



PACIFIC EARTHQUAKE ENGINEERING RESEARCH CENTER

Performance of Beam to Column Bridge Joints Subjected to a Large Velocity Pulse

Natalie Gibson

University of California, San Diego

André Filiatrault

University of California, San Diego

Scott A. Ashford

University of California, San Diego

Performance of Beam to Column Bridge Joints Subjected to a Large Velocity Pulse

Natalie Gibson

Department of Structural Engineering
University of California, San Diego

André Filiatrault

Department of Structural Engineering
University of California, San Diego

Scott A. Ashford

Department of Structural Engineering
University of California, San Diego

A final report on research supported primarily by
the Earthquake Engineering Research Centers Program
of the National Science Foundation under Award Number
EEC-9701568

PEER Report 2002/24
Pacific Earthquake Engineering Research Center
College of Engineering
University of California, Berkeley
April 2002

ABSTRACT

The destructive effects of velocity pulses were first recorded during the 1971 San Fernando, California, earthquake. However, the actual near-field behavior of a rupturing fault remained undefined until the 1994 Northridge, California, and 1995 Kobe, Japan, earthquakes. A large amount of data were gathered from structural damage and strong ground motion recording stations, allowing engineers to more fully understand the near-field seismic environment. This prompted investigations into the performance of bridges, which often have natural periods close to those of recorded velocity pulses.

For this report, four half-scale beam to column bridge joints were tested with a velocity pulse loading. Two were representative of construction before 1971, and two were typical of joints designed today. After the pulse, the joints were loaded with a typical cyclic displacement history. These joint tests were compared to joints tested previously without a pulse and to the PEER Bridge Performance Levels as outlined in Hose (1999).

This research determined that velocity pulse loading caused considerable damage to the pre-1971 joints, exhibiting Performance Levels 1–5 and loss of strength beginning during the pulse loading. The current design specimens exhibited minimal damage (Performance Levels 1–3) during the pulse and continued to perform well during the subsequent cyclic loading. Performance Level 5 and degradation began at a displacement ductility of six.

Both designs exhibited higher than predicted strengths during the velocity pulse. By modifying the material properties for the effects of high strain rate, it was shown that the higher strengths could be accounted for analytically.

ACKNOWLEDGMENTS

This work was supported in part by the Pacific Earthquake Engineering Research Center through the Earthquake Engineering Research Centers Program of the National Science Foundation under Award Number EEC-9701568. The opinions, findings, conclusions, and recommendations expressed herein are those of the authors and do not necessarily reflect the views of PEER.

CONTENTS

ABSTRACT.....	iii
ACKNOWLEDGMENTS	iv
TABLE OF CONTENTS	v
LIST OF FIGURES.....	vii
LIST OF TABLES.....	xi
LIST OF SYMBOLS	xiii
1 INTRODUCTION	1
1.1 Scope of Research.....	1
1.2 Organization of Report	2
2 LITERATURE REVIEW	3
2.1 Near-Field Ground Motions and Velocity Pulses.....	4
2.2 Effect of Velocity Pulses on Structures	5
2.3 Previous Studies on Strain-Rate Effects	6
2.3.1 Strain-Rate Effects on Steel	7
2.3.2 Strain-Rate Effects on Concrete.....	8
2.4 Previous Experiments on Effects of Velocity Pulses	10
2.5 Discussion.....	10
3 DESCRIPTION OF TEST SPECIMENS	13
3.1 Pre-1971 Test Specimens	14
3.2 Current Design Test Specimens.....	16
3.3 Construction of Test Units.....	18
4 EXPERIMENTAL SETUP AND INSTRUMENTATION.....	19
4.1 Instrumentation	20
4.1.1 Load and Displacement Measurements	21
4.1.2 Strain Gauge Measurement.....	22
4.2 Loading Protocol	25
4.3 Test Procedure	28
5 TEST RESULTS.....	31
5.1 Material Properties.....	31
5.2 General Behavior of Test Specimens	32

5.2.1	Dead Load Application	34
5.2.2	Pulse Application	37
5.2.2.1	<i>Current Design Specimens</i>	37
5.2.2.2	<i>Pre-1971 Specimens</i>	37
5.2.3	Cyclic Loading.....	40
5.2.3.1	<i>Current Design Specimens</i>	40
5.2.3.2	<i>Pre-1971 Specimens</i>	42
5.2.4	Final Stages of Test.....	44
5.2.4.1	<i>Current Design Specimens</i>	44
5.2.4.2	<i>Pre-1971 Specimens</i>	46
5.3	Global Hysteretic Behavior of Test Specimens.....	50
5.4	Energy Absorbed by Test Specimens	54
5.5	Equivalent Viscous Damping Ratio of Test Specimens	56
5.6	Stiffness Degradation of Test Specimens	59
5.7	Moment-Curvature Relationships of Test Specimens	61
5.8	Curvature Distribution in Columns	64
5.9	Measured Plastic Hinge Lengths	67
5.10	Cyclic Shear Behavior of Joints	68
5.11	Strain-Rate Distribution in Reinforcing Bars	72
6	NUMERICAL MODELING	75
6.1	Predicted Response.....	75
6.2	Moment-Curvature Response for Dynamic Tests	78
7	SUMMARY AND CONCLUSIONS.....	83
7.1	Summary.....	83
7.2	Conclusions.....	84
	REFERENCES.....	85

LIST OF FIGURES

Figure 2.1	Velocity pulse – Rinaldi Recording Station, 1994 Northridge earthquake.....	3
Figure 2.2	Directivity pulse accumulates as rupture propagates to right.....	5
Figure 3.1	Pre-1971 design reinforcement details (units 3, 4)	15
Figure 3.2	Pre-1971 beam longitudinal bar splice layout.....	16
Figure 3.3	Current design reinforcement details (units 1, 2).....	17
Figure 4.1	Experimental test setup	20
Figure 4.2	External instrumentation of test units.....	22
Figure 4.3	Pre-1971 test units: location of strain gauges on longitudinal reinforcement.....	23
Figure 4.4	Current design test units: location of strain gauges on longitudinal reinforcement	23
Figure 4.5	Pre-1971 test units: location of strain gauges on transverse reinforcement.....	24
Figure 4.6	Current design test units: location of strain gauges on transverse reinforcement	25
Figure 4.7	Displacement loading history for test units.....	27
Figure 4.8	Velocity loading history for test units.....	27
Figure 5.1	Cracking in beam joint from gravity load	34
Figure 5.2	Vertical load history: current design, quasi-static test	35
Figure 5.3	Vertical load history: pre-1971 design, quasi-static test	35
Figure 5.4	Vertical load history: current design, dynamic test.....	36
Figure 5.5	Vertical load history: pre-1971 design, dynamic test.....	36
Figure 5.6	Peak of positive pulse: current design, quasi-static test.....	38
Figure 5.7	Peak of pulse: current design, dynamic test.....	39
Figure 5.8	Peak of pulse: pre-1971 design, dynamic test.....	39
Figure 5.9	Peak of positive pulse: pre-1971 design, quasi-static test.....	39
Figure 5.10	North plastic hinge: $\mu=3$ current design, quasi-static test.....	41
Figure 5.11	South plastic hinge: $\mu=6$ current design, quasi-static test.....	41
Figure 5.12	North plastic hinge: $\mu=6$ dynamic test.....	42
Figure 5.13	Cracking in joint: $\mu=4$, pre-1971 design, quasi-static test	43
Figure 5.14	Joint around $\mu=4$: pre-1971 design, dynamic test	43
Figure 5.15	Current design after quasi-static test (north is right).....	45

Figure 5.16	Current design after quasi-static test (north is left)	45
Figure 5.17	Failure of dynamic current design (view from north)	46
Figure 5.18	Current design after dynamic test (north is left)	46
Figure 5.19	Pre-1971 joint after quasi-static test (east view of joint).....	48
Figure 5.20	Pre-1971 specimen after quasi-static test (north is right).....	48
Figure 5.21	Pre-1971 joint at failure of dynamic test (view from north)	49
Figure 5.22	Pre-1971 specimen after dynamic test (north is right)	49
Figure 5.23	Force-displacement history: non-pulse test, pre-1971 specimen (MacRae 1994)	51
Figure 5.24	Force-displacement history: non-pulse test, current design specimen (Sritharan 1996).....	52
Figure 5.25	Force-displacement history: current design specimen, quasi-static test.....	52
Figure 5.26	Force-displacement history: current design specimen, dynamic test.....	53
Figure 5.27	Force-displacement history: pre-1971 specimen, quasi-static test.....	53
Figure 5.28	Force-displacement history: pre-1971 specimen, dynamic test	54
Figure 5.29	Energy absorbed by test specimens.....	55
Figure 5.30	Equivalent viscous damping ratios: current design specimen, quasi-static test	57
Figure 5.31	Equivalent viscous damping ratios: current design specimen, dynamic test	57
Figure 5.32	Equivalent viscous damping ratios: pre-1971 specimen, quasi-static test	58
Figure 5.33	Equivalent viscous damping ratios: pre-1971 specimen, dynamic test.....	58
Figure 5.34	Secant stiffness: current design specimen, quasi-static test	59
Figure 5.35	Secant stiffness: current design specimen, dynamic test.....	60
Figure 5.36	Secant stiffness: pre-1971 specimen, quasi-static test.....	60
Figure 5.37	Secant stiffness: pre-1971 specimen, dynamic test.....	61
Figure 5.38	Moment-curvature history: current design specimen, quasi-static test	62
Figure 5.39	Moment-curvature history: current design specimen, dynamic test	63
Figure 5.40	Moment-curvature history: pre-1971 specimen, quasi-static test	63
Figure 5.41	Moment-curvature history: pre-1971 specimen, dynamic test.....	64
Figure 5.42	Curvature distribution in column: current design specimen, quasi-static test.....	65
Figure 5.43	Curvature distribution: current design specimen, dynamic test	65
Figure 5.44	Curvature distribution: pre-1971 specimen, quasi-static test.....	66
Figure 5.45	Curvature distribution: pre-1971 specimen, dynamic test	66
Figure 5.46	Evolution of plastic hinge length with displacement ductility	68

Figure 5.47	Original and deformed geometry of shear measurement in joint.....	69
Figure 5.48	Joint shear deformation history: current design specimen, quasi-static test	70
Figure 5.49	Joint shear deformation history: current design specimen, dynamic test.....	70
Figure 5.50	Joint shear deformation history: pre-1971 specimen, quasi-static test.....	71
Figure 5.51	Joint shear deformation history: pre-1971 specimen, dynamic test.....	71
Figure 5.52	Strain-rate time-history: south column longitudinal bar, pulse of current design specimen, dynamic test	72
Figure 5.53	Strain-rate time history: north column longitudinal bar, pulse of current design specimen, dynamic test	73
Figure 5.54	Strain-rate time history: south column longitudinal bar during cyclic loading of current design, dynamic test	73
Figure 5.55	Strain-rate time history: south column longitudinal bar during cyclic loading of current design, dynamic test	74
Figure 6.1	Moment-curvature history: current design specimen, quasi-static test	76
Figure 6.2	Moment-curvature history: pre-1971 specimen, quasi-static test	77
Figure 6.3	Moment-curvature history: current design specimen, dynamic test	77
Figure 6.4	Moment-curvature history: pre-1971 specimen, dynamic test.....	78
Figure 6.5	Moment-curvature history: current design specimen with revised gauge length for curvature calculation.....	79
Figure 6.6	Moment-curvature history: pre-1971 specimen with revised gauge length for curvature calculation	79
Figure 6.7	Moment-curvature history: current design dynamic test with prediction revised for dynamic material properties	81
Figure 6.8	Moment-curvature history: pre-1971 dynamic test with prediction revised for dynamic material properties	81

LIST OF TABLES

Table 5.1	Compressive strength of concrete cylinders taken from concrete pours.....	31
Table 5.2	Yield and ultimate strength of steel reinforcing bars	32
Table 5.3	PEER bridge performance levels (Hose 1999)	33
Table 6.1	Dynamic material properties	80

LIST OF SYMBOLS

A_h	area of hysteresis loop
α	factor to account for strain rate on the modulus of elasticity
B	horizontal linear potentiometer length in shear panel of joint
D	diagonal linear potentiometer length in shear panel of joint
d_b	diameter of longitudinal reinforcing bar
Δ	horizontal displacement at top of test column
Δ_i	horizontal displacement at given time step
Δ_{i+1}	horizontal displacement at next time step
Δ_m	maximum horizontal displacement
Δ_y	displacement at yield
E	modulus of elasticity
E_i	energy at given time step
E_{i+1}	energy at next time step
$\dot{\varepsilon}$	strain rate
$\dot{\varepsilon}_0$	strain rate at quasi-static loading
ε_u	ultimate compressive strain of concrete
f	stress
f_y	yield stress for steel
f_u	ultimate stress for steel
f'_c	compressive strength of concrete
h_c	horizontal distance between potentiometer pairs mounted on column
θ	angle of vertical potentiometer from horizontal
K_{eq}	equivalent secant stiffness
L	length of column
l_g	gauge length
L_p	plastic hinge length in column
L_{sp}	strain penetration length of column longitudinal reinforcing steel into base
M_I	ideal moment
M_y	yield moment

μ	ductility level
N_a	near-source factor (1997 UBC) for acceleration ranges of the response spectrum
N_v	near-source factor (1997 UBC) for velocity ranges of the response spectrum
ξ_{eq}	equivalent viscous damping ratio
π	Archimedes' number (pi) equal to 3.14159
ρ_y	yield ratio for steel
S	south vertical potentiometer length in shear panel of joint
V_i	force from horizontal actuator at given time step
V_{i+1}	force from horizontal actuator at next time step
V_m	maximum horizontal force from actuator
ϕ	column curvature
ϕ_y	yield curvature

1 Introduction

Recordings from recent earthquakes have provided evidence that ground motions in the near field of a rupturing fault can contain a large energy, or “directivity,” pulse. A directivity pulse occurs when the propagation of the fault proceeds at near the same rate as the shear wave velocity. This pulse is seen in the forward direction of the rupture, and can cause considerable damage during an earthquake, especially to structures with natural periods close to those of the pulse.

The destructive 1994 Northridge, California, and 1995 Kobe, Japan, earthquakes occurred near densely populated areas, and researchers were able to gather a great number of recordings of the strong ground shaking. The pattern of structural damage also provided good data. Although the issue of a velocity pulse loading was first addressed after the 1971 San Fernando, California, earthquake, it was the loss of life and cost of structural damage from the more recent earthquakes that prompted the need for additional research into the problem of velocity pulses. The Pacific Earthquake Engineering Research (PEER) Center funded a three-year effort to investigate the effect of a large velocity pulse applied to bridges. The focus of this report is on the effect of a velocity pulse on bridge subassemblages; the specifics of this phase of the research are outlined in Section 1.1.

1.1 SCOPE OF RESEARCH

The research for this report involved the testing of four beam-column joint specimens. Two of the units were modeled after an existing bridge joint that was built before 1971. The design of the other two joints was revised to reflect the current engineering practice of the time (1996). This model would still be typical of joint design today. The designs for the joints were taken from joints previously tested under typical cyclic loading at the University of California, San Diego (UCSD). This report investigates the behavior of the specimens when they are subjected

to a large velocity pulse. This pulse was applied dynamically to two of the specimens and quasi-statically to the other two. After the pulse, the joints were loaded with the same cyclic loading that the non-pulse test specimens received. The results from this research were then compared to the results of the non-pulse tests, and to the PEER Bridge Performance Levels as outlined in Hose (1999). The test data were also examined for the effects of high strain rates on joint behavior.

1.2 ORGANIZATION OF REPORT

The following report is divided into eight chapters. This first chapter is the introduction chapter and has presented the intentions of the research. The second chapter is a review of the relevant literature published on velocity pulses, their effects on structures, and the effects of strain rate on material properties. The third chapter describes the construction of the test specimens. Chapter 4 presents the instrumentation of each specimen, and describes how the test was performed including the loading protocol that was used. Chapter 5 presents photographs and graphical results of the four tests. Comparisons of the behaviors of the tests are also presented in Chapter 5. In Chapter 6, the data from the tests are compared to the prediction of a moment-curvature model. The model is then modified to take into account the effect of high strain rate induced by the velocity pulse on the material properties. Chapter 7 presents the conclusions of the research. The eighth chapter provides the references for information presented in this report.

2 Literature Review

The destructive potential of near-fault ground motions manifested itself during the 1994 Northridge, California, and 1995 Kobe, Japan, earthquakes. For one of the few times in recent history, these earthquakes were centered near highly populated areas. The large amount of data gathered from structural damage and strong ground motion recording stations allowed engineers to more fully understand the near-field seismic environment. Both earthquakes generated peak velocities as high as 175 cm/sec and velocity pulses with periods in the range of 1 sec to 2 sec as illustrated in Figure 2.1. This period is close to the natural period of many structures such as bridges and mid-rise buildings, several of which were severely damaged (Somerville 2000).

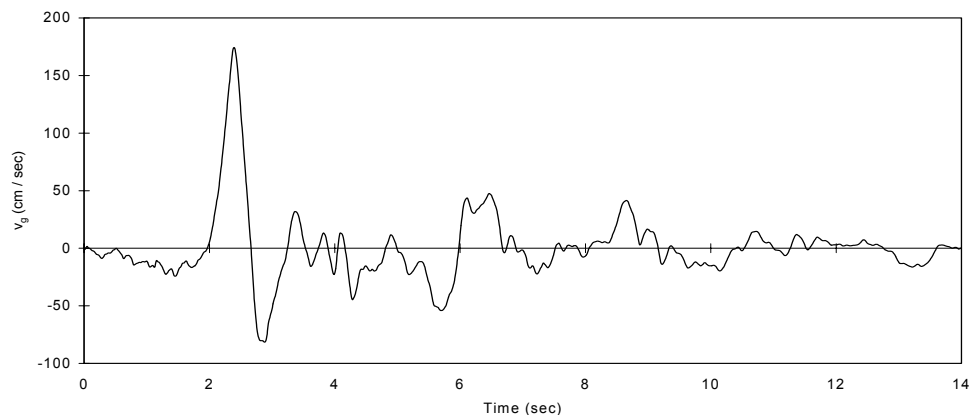


Fig. 2.1 Velocity Pulse — Rinaldi Recording Station, 1994 Northridge earthquake

The current edition of the Uniform Building Code (1997) has begun to address this problem. It defines near-field sites as any area within 15 km of a known active fault, and specifies base shear amplification factors to account for the increased loading. Since 1994, research has been undertaken to better understand the behavior of structures when subjected to near-field ground motions.

2.1 NEAR-FIELD GROUND MOTIONS AND VELOCITY PULSES

The near field of an earthquake can be defined as any area in the close vicinity of the fault rupture surface. In the near field, the ground shaking is influenced by a number of factors. Besides strong shaking, the characteristics of near-field ground motions are linked to the fault geometry and the orientation of the traveling seismic waves (Somerville 2000). Vertical strike-slip faults can produce a directivity effect, and dip-slip faults can produce directivity effects as well as hanging wall effects. Hanging wall effects are felt on the hanging wall of a fault (the earth above a vertically dipping fault), and are due to the proximity of much of the fault to hanging wall sites.

A main issue of concern for structures in the near field of an earthquake is the directivity effects of the slipping fault. Somerville (1997), Hall (1998) and others have studied and quantified the characteristics of near-fault ground motions. When a fault rupture propagates toward a site at a velocity close to that of the shear wave velocity, an accumulation of most of the energy of the seismic radiation of the fault can arrive at the site as a single long-period pulse. This is called a directivity pulse. The directivity pulse can be explained using a model first suggested by Abrahamson (1998) shown in Figure 2.2. The rupture is broken into subfaults; beginning at the epicenter, the rupture propagates along the fault in the direction of the arrow toward Site A. Because the velocity of the shear waves is close to the rupture velocity, the energy of the forward direction arrives within a short time period. Forward directivity effects only occur when the rupture propagates toward the site, and the direction of slip on the fault is aligned with the site. Not all near-fault locations will experience forward rupture directivity effects in a given event. It can be seen by the model that the Site B will experience a lengthening of the time between the arrival of the waves; thus the record at Site B will have a long duration but not a velocity pulse.

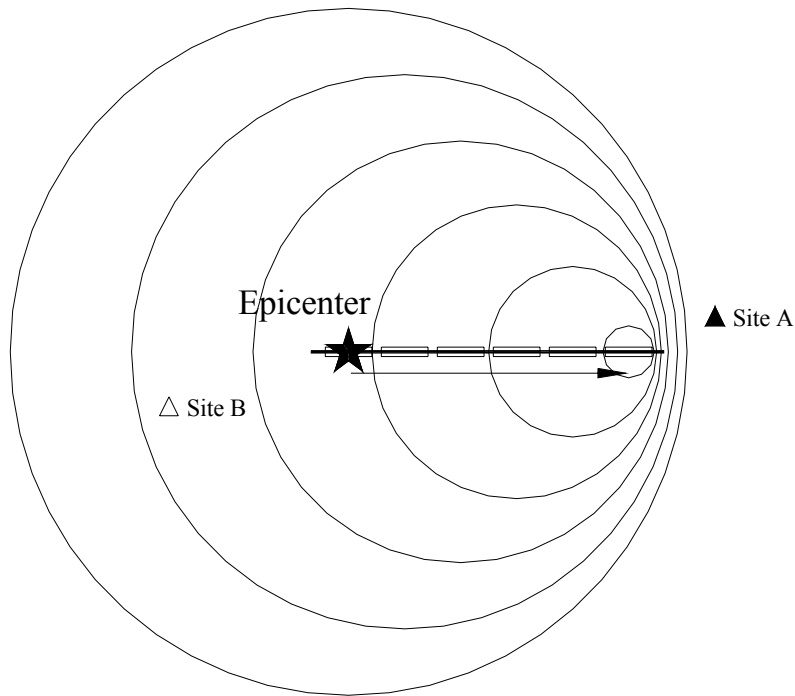


Fig. 2.2 Directivity pulse accumulates as rupture propagates to right

Forward directivity effects can be felt for both strike-slip faults and dip-slip faults. On a strike-slip fault, the directivity effects are mostly concentrated away from the hypocenter because the energy builds up as the shear waves travel away from the point of dislocation toward the site. A dip-slip fault produces forward directivity effects at the sites located around the surface exposure of the fault. Although the geometry of a fault is usually well known, the direction of rupture is unpredictable. Therefore it is recommended that all buildings that fall within the near field of an active fault be designed for a possible velocity pulse.

2.2 EFFECT OF VELOCITY PULSES ON STRUCTURES

The 1997 UBC has begun to address the problem of directivity pulses in the near field of an earthquake. Near-source factors, N_a and N_v are introduced for the respective short period (acceleration) and intermediate period (velocity) ranges of the response spectrum. These factors are intended to reflect the fact that the near-fault rupture directivity enhances the intermediate

period part of the response spectrum. There is a growing concern that even designing to this enhanced spectrum may still not adequately address the demands on structures produced by brief, impulsive ground motions (Somerville 2000). Since the location of a site relative to a causative fault is usually known, Somerville (1998) indicated a need to augment the response spectrum with motions in the form of simplified pulses that can be related to the magnitude, fault distance, and site conditions.

Krawinkler (1996) suggested a guideline for choosing loading histories to test steel structures in order to assess their seismic performance. Loading should begin with low symmetrical cycles of positive and negative load in the elastic range and then three cycles each at increasing multiples of the yield displacement of the test structure until failure. This testing protocol may be adequate when looking at a far-field earthquake, but must be revised when testing for a velocity pulse. A major difference in the loading of a velocity pulse is the rate of loading on the materials. The mechanical properties of the materials may change substantially as a result of a high strain rate. These changes in material properties may in turn affect the stiffness, strength and energy dissipation characteristics of the test structure. Therefore, the added velocity with which the forces are applied must be considered in the experimental investigation. Another aspect that must be considered when testing for a velocity pulse is that the pulse of energy usually occurs at the beginning of the earthquake record, and therefore before the structure has begun to yield.

2.3 PREVIOUS STUDIES ON STRAIN-RATE EFFECTS

The majority of structural testing for earthquake loading is performed quasi-statically, thus implying that the loads are applied at rates slow enough so that material strain-rate effects do not influence the results (Leon 1996). It is important to recognize that actual earthquake loads will impose higher loading rates than quasi-static testing represents, and that structural response during real earthquake loading will include the effects of strain rate. This is especially important in the case of near-field earthquakes. The range of strain rates induced by near-field ground motions is 10^{-1} to 10 sec^{-1} higher than the values currently considered in design (Gioncu 2000). This type of loading can cause the structure to behave very differently than predicted in laboratory tests.

Abrams (1996) performed testing on concrete and masonry structures under quasi-static and then dynamic loading. He found that the structures loaded slowly (quasi-statically) exhibited decreased strength and stiffness when compared to the same structure loaded dynamically. Damage was much more prominent at the slower loading rate because of increased crack propagation.

Many researchers have investigated the relationships between material properties and strain rate. Empirical equations have been proposed to modify material properties obtained from quasi-static testing to account for strain rates.

2.3.1 Strain-Rate Effects on Steel

In the design of steel for structures the steel is expected to be able to withstand large plastic deformations before failure. Test results have indicated, however, that high strain rates can decrease the ratio between the ultimate stress and the yield stress. This means that a ductile failure could become a brittle fracture.

The first testing on strain rates was performed by Manjain (1944). This testing documented an increase in yield stress with an increase in strain rate, especially at strain rates higher than 10^{-1} sec^{-1} , which corresponds to the range of strong earthquake shaking. The increase in strain rate had little effect on the ultimate tensile strength, thus the yield ratio, ρ_y , defined below, where f_y is the yield stress and f_u is the ultimate strength, increases with strain rate.

$$\rho_y = \frac{f_y}{f_u} \quad (2.1)$$

More recent testing has verified the results presented by Manjain and has resulted in equations proposed for relating the yield and ultimate stress at higher strain rates to those at quasi-static rates ($f_{y,dyn}$ and $f_{u,dyn}$ are the yield stress and ultimate stress considering the effects of strain rate).

- Wright and Hall (1964), $10^{-6} \text{ sec}^{-1} < \dot{\epsilon} < 10^3 \text{ sec}^{-1}$

$$\frac{f_{y,dyn}}{f_y} = 1 + 2.77 \exp[0.162(\log \dot{\epsilon} - 3.74)] \quad (2.2)$$

- Soroushian and Choi (1987), $10^{-4} \text{ sec}^{-1} < \dot{\epsilon} < 10^1 \text{ sec}^{-1}$

$$\frac{f_{y,dyn}}{f_y} = 1.46 - 4.51 \times 10^{-7} f_y + (0.0927 - 9.20 \times 10^{-7} f_y) \log \dot{\epsilon} \quad (2.3)$$

(f_y in MPa)

$$\frac{f_{u,dyn}}{f_u} = 1.15 - 7.7 \times 10^{-7} f_y + (0.0497 - 2.44 \times 10^{-7} f_y) \log \dot{\epsilon} \quad (2.4)$$

(f_y in MPa)

- Kaneko et al. (1996), $10^{-4} \text{ sec}^{-1} < \dot{\epsilon} < 10^1 \text{ sec}^{-1}$, $\dot{\epsilon}_0 = 10^{-4} \text{ sec}^{-1}$

$$\frac{f_{y,dyn}}{f_y} = 1 + \frac{21}{f_y} \log \frac{\dot{\epsilon}}{\dot{\epsilon}_0} \quad (f_y \text{ in MPa}) \quad (2.5)$$

$$\frac{f_{u,dyn}}{f_u} = 1 + \frac{7.4}{f_y} \log \frac{\dot{\epsilon}}{\dot{\epsilon}_0} \quad (f_y \text{ in MPa}) \quad (2.6)$$

- Ammann (1995), $\dot{\epsilon} \leq 10 \text{ sec}^{-1}$, $\dot{\epsilon}_0 = 5 \times 10^{-5} \text{ sec}^{-1}$

$$\frac{f_{y,dyn}}{f_y} = 1 + \frac{6}{f_y} \ln \left(\frac{\dot{\epsilon}}{\dot{\epsilon}_0} \right) \quad (f_y \text{ in MPa}) \quad (2.7)$$

$$\frac{f_{u,dyn}}{f_u} = 1 + \frac{1.5}{f_u} \ln \left(\frac{\dot{\epsilon}}{\dot{\epsilon}_0} \right) \quad (f_u \text{ in MPa}) \quad (2.8)$$

- Wakabayashi (1984), $5 \times 10^{-5} \text{ sec}^{-1} < \dot{\epsilon} < 5 \times 10^{-2} \text{ sec}^{-1}$, $\dot{\epsilon}_0 = 5 \times 10^{-5} \text{ sec}^{-1}$

$$\frac{f_{y,dyn}}{f_y} = 1 + 4.73 \times 10^{-2} \log_{10} \left| \frac{\dot{\epsilon}}{\dot{\epsilon}_0} \right| \quad (2.9)$$

The modulus of elasticity of steel remains relatively unchanged with strain rate.

2.3.2 Strain-Rate Effects on Concrete

Less testing has been performed on the strain-rate effects of concrete than those for steel. Most of the research has been centered on dynamic impact loads, which consider strain rates much higher than quasi-static and typical earthquake loads but are about 10 times higher than the loads seen for velocity pulses. The equations proposed by Wakabayshi (1984) were determined for the strain rates of dynamic earthquake loading on structures. Equations have been proposed to account for the differences in compressive stress, modulus of elasticity, and ultimate strain.

The modulus of elasticity of concrete in compression increases with strain rate. The modulus including the effects of strain rate, E_{dyn} , can be to the static modulus through:

- Ammann (1995), $\dot{\epsilon}_0 = 30 \times 10^{-6} \text{ sec}^{-1}$

$$\frac{E_{dyn}}{E} = \left(\frac{\dot{\epsilon}}{\dot{\epsilon}_0} \right)^{0.026} \quad (2.10)$$

This relationship is valid for all grades of concrete.

The compressive strength of concrete was found to increase with the strain rate. The relationship between the dynamic compressive strength, f_{dyn} , and the static compressive strength, f , takes into account the effect of strain rate on the modulus.

- Ammann (1995), $\dot{\epsilon} \leq 30 \text{ sec}^{-1}$, $\dot{\epsilon}_0 = 30 \times 10^{-6} \text{ sec}^{-1}$

$$\frac{f_{dyn}}{f} = \left(\frac{\dot{\epsilon}}{\dot{\epsilon}_0} \right)^{1.026\alpha} \quad \text{where } \alpha = \frac{1}{5 + 3 \frac{f'_c}{4}} \quad (2.11)$$

- Wakabayashi (1984), $\dot{\epsilon}_0 = 5 \times 10^{-5} \text{ sec}^{-1}$

$$\frac{f_{dyn}}{f} = 1 + 6.58 \times 10^{-2} \log_{10} \left| \frac{\dot{\epsilon}}{\dot{\epsilon}_0} \right| \quad (2.12)$$

The strain at maximum stress (ϵ_u), or the ultimate compressive strain of concrete, increases with the strain rate. This relationship between the ultimate compressive strain under dynamic loading, $\epsilon_{u,dyn}$, and the ultimate compressive strain under quasi-static loading, $\epsilon_{u,stat}$, can be calculated by the following equation:

- Ammann (1995), $\dot{\epsilon}_0 = 30 \times 10^{-6} \text{ sec}^{-1}$

$$\frac{\epsilon_{u,dyn}}{\epsilon_{u,stat}} = \left(\frac{\dot{\epsilon}}{\dot{\epsilon}_0} \right)^{0.02} \quad (2.13)$$

Wakabayashi (1984) also performed testing on reinforced concrete beams under dynamic loading. The equations above were applied to a theoretical model and were found to predict well the dynamic test results. It was found that the moment-bearing capacity during the first cycle was much larger than during the following cycles. This confirmed that the increase in the moment capacity in the first cycle is significantly due to concrete stress. After the first cycle, the bending resistance was governed only by the behavior of the reinforcing bars due to cracking in the concrete.

2.4 PREVIOUS EXPERIMENTS ON EFFECTS OF VELOCITY PULSES

The project described in this section of the report is one phase of a three-year study of the Pacific Earthquake Engineering Research Center (PEER) on the effects of velocity pulses on bridge components, subassemblages, and systems. The investigation at UCSD began by testing long and short bridge columns.

The first study at UCSD (Orozco 2001) investigated three flexural columns subjected to a large pulse and subsequent cyclic loading at increasing multiples of yield ductility. These columns were compared to columns tested at UC Irvine (Hamilton 2000) under a non-pulse cyclic loading. It was found that the flexural columns performed well. During the pulse they exhibited increased strength and smaller plastic hinge lengths when compared to the non-pulse loading, but the ultimate strengths and ductilities were similar.

A subsequent study at UCSD (Makley 2001) investigated three different designs of shear columns subjected to a velocity pulse and then cyclic loading at increasing multiples of yield ductility until failure. These columns again were compared to similar columns tested at UC Irvine without a pulse.

Research on the effects of bridge columns and assemblies to velocity pulses is just beginning to be published. Mayes and Shaw (1997) investigated analytically the effects of near-source ground motions on bridge columns designed to current specifications for the California Department of Transportation. Mahin and Hachem (1998) investigated the response of simple bridge structures to near-fault ground motions to determine trends in the relation of bridge periods to duration of near-fault pulses. Other recent research has been conducted on the effects of near-field ground motions on building response (Hall 1995, Attalla 1995, Iwan 1996).

2.5 DISCUSSION

Since the location of active faults near structures is usually well known, it is important to take into account forward directivity effects in design, especially for long-period structures like bridges that would be greatly damaged by a response spectrum that is rich in periods higher than 0.5 sec. Consideration for the retrofit of existing structures near known faults would also be important.

Owing to the limited amount of experimental research that has been done on structures for near-field ground motions, it is important to study the behavior of bridge structures for pulse-

type motions that will combine large velocities and high strain rates, as well as large displacements. To date, testing of bridge components for near-field effects has been limited to simplified models and columns. There is a lack of information on the behavior of beam-column connections when subjected to a large velocity pulse. It is also important to investigate these structures for not only the traditional quasi-static types of loading, but also dynamic loading so that a comparison can be made and the effects of strain rate on joints can be determined. This report will contribute to shedding some light on these issues.

3 Description of Test Specimens

The main objective of this research is to examine the behavior of beam-column joints subjected to a velocity pulse. Two different types of designs were chosen to investigate, an older connection as well as a current one. Research has already been done at UCSD on the behavior of T-joints during quasi-static cyclic loading. In order to facilitate testing and reduce the number of connections that needed to be built for this project, it was decided to design the joints based on the previous tests.

MacRae et al. (1994) investigated the performance of as-built T-joints from pre-1960 design. A 3/4-scale model of the interior joint from Bent 793+57 of the Santa Monica Viaduct in Los Angeles, California, was chosen to test. This joint is typical of the joints that were designed and constructed before the destructive 1971 San Fernando earthquake that caused a large amount of damage to many bridges. It was found from this experimental study that the lightly reinforced joints are not dependable, and that joint shear failure is likely to occur prior to developing flexural capacity in the columns. This type of joint shear failure was observed in bridges following the 1971 San Fernando and 1989 Loma Prieta earthquakes.

Sritharan et al. (1996) redesigned the joint from MacRae's study to the current standards in order to assess the effectiveness of new joint details. The redesign of the joint followed the design methods proposed by Priestley et al. (1993). The particular method was chosen, from those available, to reduce the steel congestion within the joint. In the detailing of the new joint (labeled IC1), it was ensured that the column longitudinal reinforcement was anchored adequately into the joint so that the plastic flexural capacity of the column could be developed. These tests were undertaken after the 1989 Loma Prieta earthquake in northern California, which caused significant damage to many beam-column connections. The 1996 report was part of a project to examine the competency of as-built joints and to establish efficient details for new bridge joints. For comparison, this project used the information from MacRae (1994).

The previous testing provided a good baseline for the performance of both current and older bridge joints subjected to cyclic loading. This project will compare the results of the velocity pulse testing to the previous tests.

3.1 PRE-1971 TEST SPECIMENS

The two pre-1971 test specimens considered in this investigation are 1/2 scale models designed to match the previously tested joints. Although the original joint (labeled SM3) tested by MacRae (1994) was 3/4 scale, Sritharan (1996) scaled the results to compare with the results of 1/2 scale tests. The pre-1971 and the current design specimens selected for this project were all built at the same 1/2 scale to allow direct comparisons between the results of the four tests.

The specimen was constructed in an inverted position for ease of testing. Reinforcing details of the pre-1971 test specimens (units 3 and 4) are shown in Figure 3.1. The reinforcement used was Grade 60 steel. The column was 609.6 mm (24 in.) in diameter. The height of the column was 1829 mm (6 ft) from the soffit to the loading axis. This column height corresponds to the distance between the joint interface and the assumed point of contraflexure halfway up the column in the prototype structure. The column was reinforced with 14 #7 longitudinal bars ($d_b=22.2$ mm). The longitudinal bars were anchored into the joint using the same requirements of the prototype structure (16 bar diameters). The transverse column reinforcement was a #3 spiral spaced at 97 mm (3.8 in.) over the full height of the column.

The original specimen SM3 was tested with portions of the surrounding deck and soffit slabs connecting to the beam. For this investigation, the slab was considered irrelevant as long as the beam was sufficiently detailed to resist the same bending moment as that resisted by the SM3 assembly. Neglecting the deck and soffit slabs was expected to ease complexity associated in identifying force transfer mechanisms of the joints.

The beam was 610 mm (24 in.) deep and 686 mm (27 in.) wide. The length of the beam was 1219 mm (48 in.) from the center of the column to each point of support. In order to match the reinforcing ratios of the prototype, the deck was reinforced with 4 #7 ($d_b=22.2$ mm), 2 #3 ($d_b=9.5$ mm), and 3 #2 ($d_b=6.4$ mm) bars. The deck bars ran continuously for the length of the beam. The soffit was reinforced with 4 #7 ($d_b=22.2$ mm) and 3 #2 ($d_b=6.4$ mm) bars. To match the prototype and the customary detailing of the time, all of the #2 bars and one of the #7 bars were spliced within the joint region, as shown in Figure 3.2. Transverse #2 ($d_b=6.4$ mm) open

stirrups were provided at a spacing of 114 mm (4-½ in.). Similar to the prototype, no joint reinforcement was provided. The column spiral ended at the soffit face, and the transverse stirrups in the beam ended at the column face.

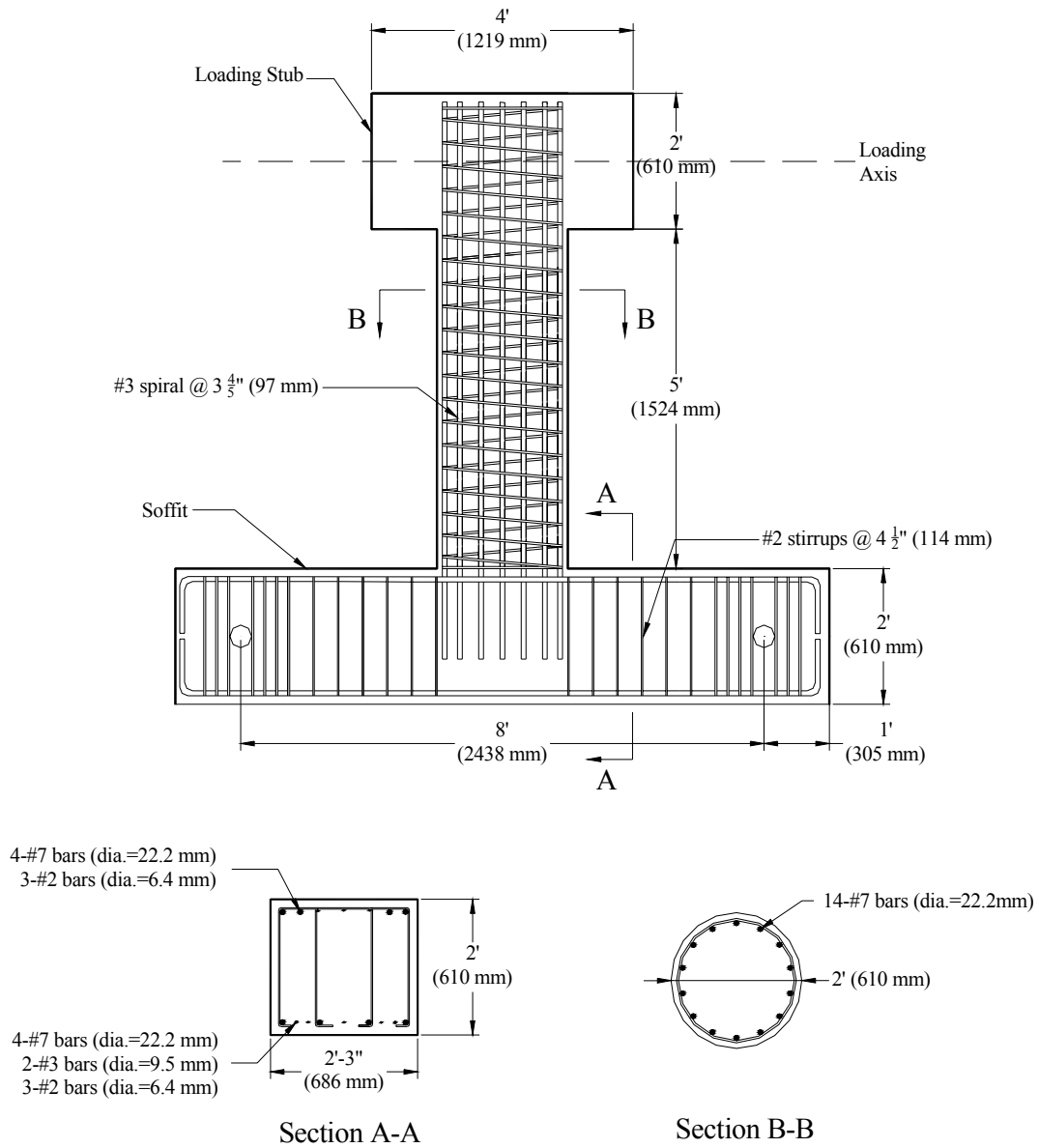


Fig. 3.1 Pre-1971 design reinforcement details (units 3, 4)

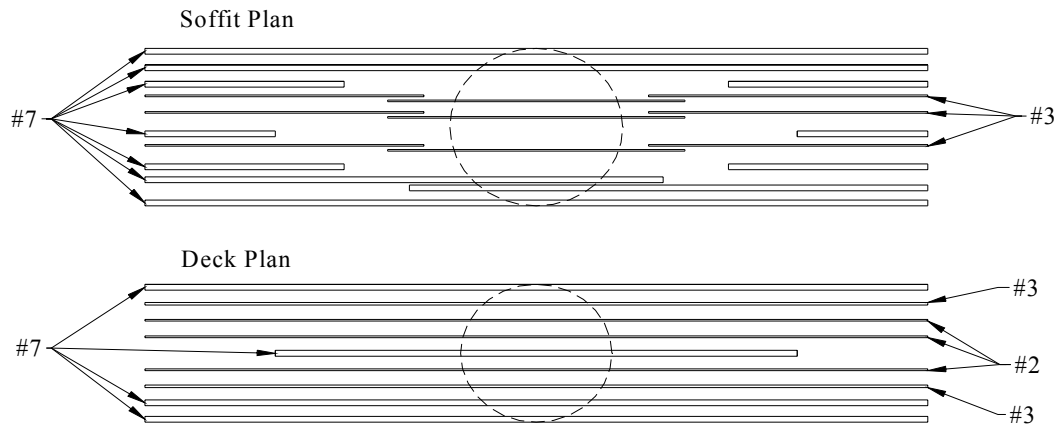


Fig. 3.2 Pre-1971 beam longitudinal bar splice layout

3.2 CURRENT DESIGN TEST SPECIMENS

The two current design test specimens considered in this investigation were similar to the IC1 design (Sritharan 1996) to allow a direct comparison to be made between the test results obtained in this project and the ones obtained in the Sritharan test.

The test units were built in an inverted position, similar to those of the pre-1971 design. The outside dimensions of the four test units are identical. The reinforcement details of the current design test specimens (units 1 and 2) are shown in Figure 3.3. The reinforcing is Grade 60 steel. The column is reinforced with 14 #7 bars ($d_b=22.2$ mm) that extend fully into the joint (533 mm, 21 in.) to meet the cap beam deck steel. A #3 spiral spaced at 97 mm (3.8 in.) was placed over the entire height of the column. The column longitudinal bars within the joint are restrained transversely by a #3 ($d_b=9.5$ mm) spiral spaced at 57 mm (2- $\frac{1}{4}$ in.).

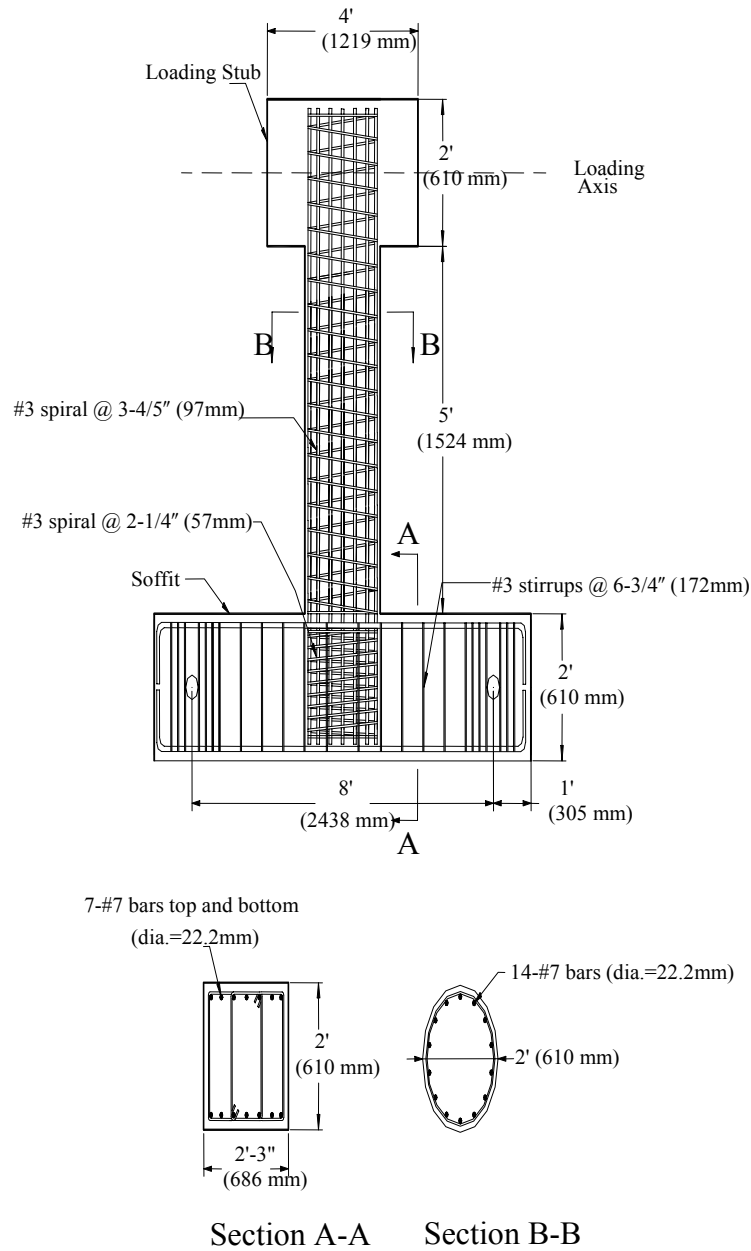


Fig. 3.3 Current design reinforcement details (units 1, 2)

The beam steel was designed by Sritharan (1996) to resist the maximum moment that could be delivered to the joint by the column plus an overstrength capacity of 30%. Again, to ease the complexity in analyzing the force transfers in the joint, the deck and soffit slabs of the prototype were left out. The beam steel was designed to resist the entire overstrength moment. The beam was reinforced with 7 #7 bars ($d_b=22$ mm) top and bottom. The bars ran continuously

over the length of the beam. Transverse reinforcement was provided by #3 (9.5 mm) closed double stirrups at a spacing of 172 mm (6-¾ in.). Within the joint, transverse reinforcing was provided by two sets of double #3 hairpins.

3.3 CONSTRUCTION OF TEST UNITS

The first units (1 and 2) were built simultaneously. Each unit was cast in two concrete pours. The beams and joint regions were cast first, and then the columns and loading stubs. This procedure introduced a construction joint at the beam-column interface. After the first two units cured, the same procedure was applied to units 3 and 4 using the same forms. Standard concrete mix was used in all four test units. The target 28-day compressive strength was 34.5 MPa (5 ksi). The concrete and steel material strengths were determined before testing was performed on the specimens. The results will be presented in Chapter 5.

4 Experimental Setup and Instrumentation

This research project investigates the behavior of two beam-column joints designed as described in Chapter 3. In order to allow the joint to behave during the test as it would in an actual structure, the joint region must be allowed to rotate as it transfers bending moment between the column where the load is applied and the beam. The simulated seismic loading is applied horizontally at the end of the column, which corresponds to the point of contra-flexure of the prototype structure. For ease of loading and restraint, the four units were tested in an inverted position, as seen in Figure 4.1. Each end of the beam was connected to the strong floor. At the north end of the beam, the movements were restrained in the horizontal and vertical directions. However, the beam was allowed to rotate around a steel pin that was fitted through a cast-in pipe in the beam end. The south end of the beam was restrained in only the vertical direction. This was achieved through the use of a steel pin through the cast-in pipe at that end as well as from links that connected the pin to the base but allowed horizontal movement.

A simulated gravity load was applied to the column and joint through a steel load beam that was attached to the top of the column. Two actuators were connected to the load beam and then to the strong floor to apply the vertical gravity load. The vertical actuators had a 734 kN (165 kip) capacity and a +/- 152 mm (6 in.) stroke. A constant load of 200 kN (45 kips) was applied by each actuator and maintained for the entire test. The horizontal cyclic load was applied by an actuator mounted to the strong wall and attached at the load stub at the top of the column. The horizontal actuator had a 980 kN (220 kip) capacity and a +/- 228 mm (9 in.) stroke, with a servo capacity of 15.8 liters per second (250 gallons per minute [GPM]). The horizontal actuator was controlled in displacement.

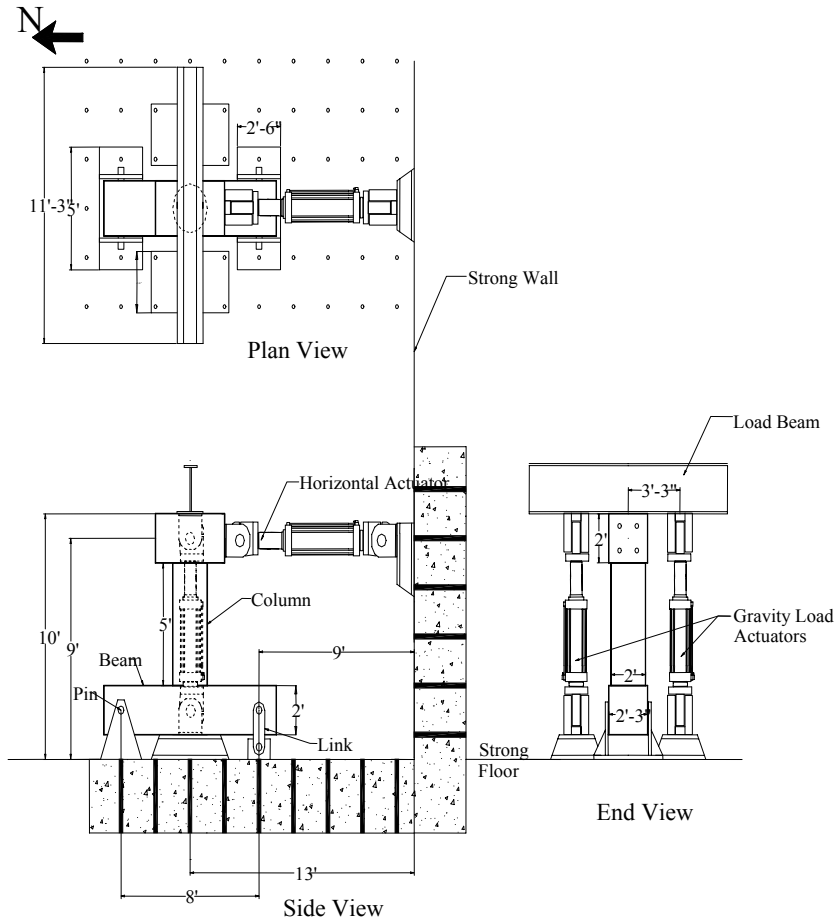


Fig. 4.1 Experimental test setup

4.1 INSTRUMENTATION

The test units were instrumented heavily with strain gauges, linear potentiometers, a rotation device, and an accelerometer for the dynamic tests. The instruments of the four units were identical. The strain gauges differed only for the pre-1971 units for which there were no joint spirals to instrument and for which the column longitudinal bars were not as long as for the current design specimens. The layout of the gauges and devices was similar to that done by Sritharan (1996) to allow comparison between the results from the pulse tests and the non-pulse testing.

4.1.1 Load and Displacement Measurements

The horizontal and vertical loads for the tests were measured from load cells mounted at the end of each actuator. The horizontal input displacement for the tests was controlled through a linear potentiometer, with a +/- 228mm (9 in.) stroke, that was connected between a reference column placed just north of the north end of the beam, and the center of the north side of the load stub, as illustrated in Figure 4.2. The north and south faces of the column were each instrumented with 5 +/- 38 mm (1-½ in.) linear potentiometers placed vertically. They were connected to brackets mounted in the concrete of the column at 178, 330, 482, 634, and 939 mm (7, 13, 19, 25, and 37 in.) from the soffit of the beam. These potentiometers were installed to measure the curvature of the column during the test.

Two linear potentiometers were placed under the beam directly below the edges of the column to measure the movement of the beam as the joint rotated during the test. The east face of the joint was instrumented with +/- 38 mm (1-½ in.) linear potentiometers as shown in Figure 4.2 to measure the deformation of the panel. A potentiometer was placed at the south end of the beam to measure any horizontal movement of the structure. Each specimen was also equipped with a rotation measurement device (inclinometer) mounted to the load stub on the west side at the intersection of the line of load application and the centerline of the column. For the two dynamic tests, an accelerometer was mounted just below the point where the overall displacement was measured on the north side of the load stub.

gauged the same way except for the fact that the gauges extend only 508 mm (20 in.) in each direction from the centerline of the column.

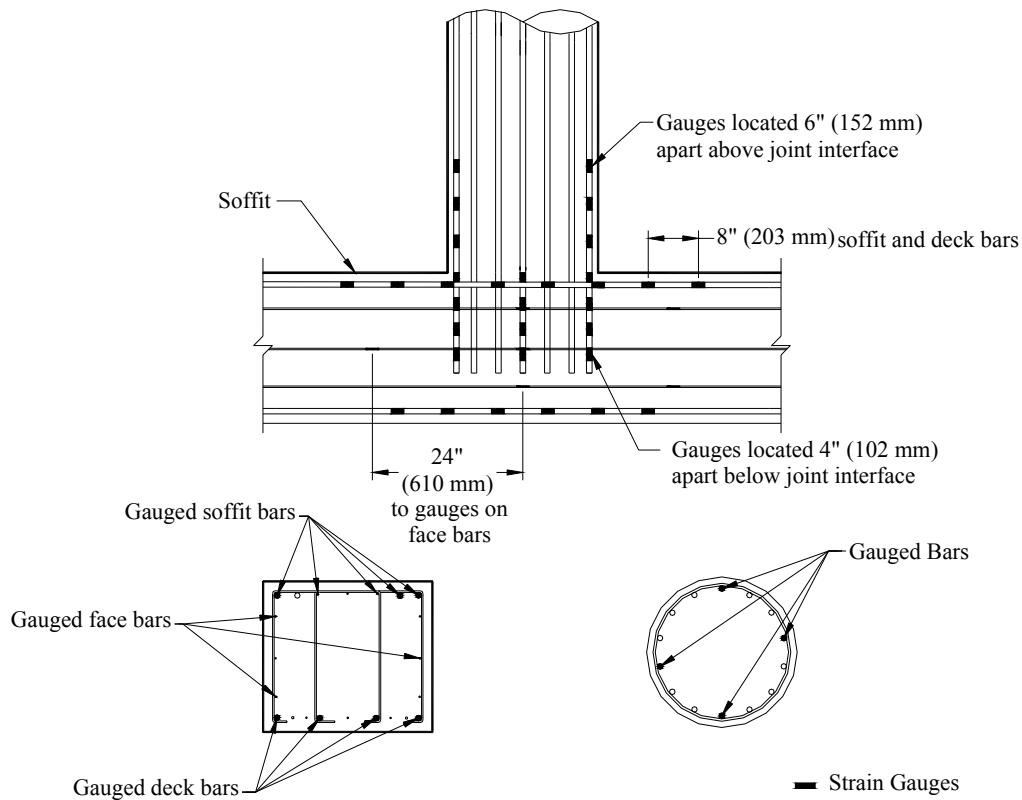


Fig. 4.3 Pre-1971 test units: location of strain gauges on longitudinal reinforcement

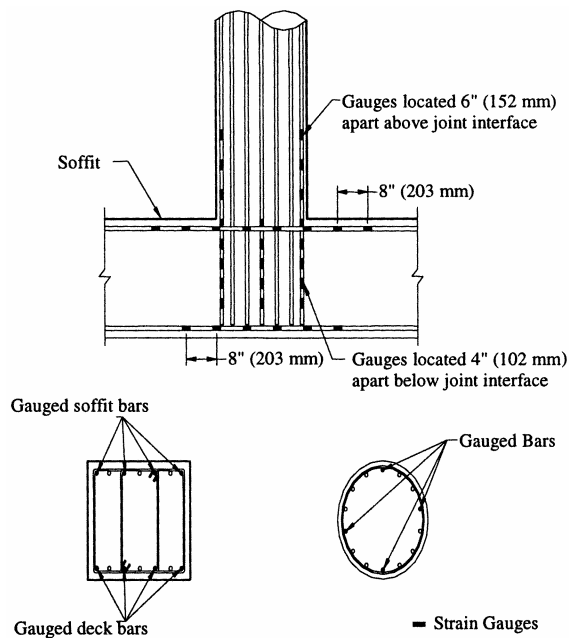


Fig. 4.4 Current design test units: location of strain gauges on longitudinal reinforcement

Four column longitudinal bars were gauged. The gauged bars were placed in the north, south, east, and west directions of the column. The north and south column bars have gauges spaced at 102 mm (4 in.) within the joint and at 152 mm (6 in.) in the column. The east and west bars are gauged only within the joint, with the gauges spaced at 102 mm (4 in.). The column longitudinal bars in the current design specimens extended further into the joint than the pre-1971 specimens, thus they had four gauges in the joint and the pre-1971 units have three gauges in the joint.

The layout of the strain gauges on the transverse reinforcement can be seen in Figure 4.5 for the pre-1971 test units, and in Figure 4.6 for the current design test units. The first five beam stirrups in each direction from the joint were gauged at the 1/6 point, halfway, and 5/6 way down the side of the stirrup. Only one of the double stirrups was gauged, so there were gauges in the interior and exterior of the beam.

The hairpin-reinforcing bar in the joint of the current design was also gauged in the same way. The pre-1971 units were also provided with three #2 bars evenly spaced up the east and west faces of the beam. These bars were gauged at the centerline and at 24 in. north and south of the joint centerline in order to help quantify the behavior of the joint in shear. The gauges used were 5 mm high-yield gauges with a gauge factor of 2.12.

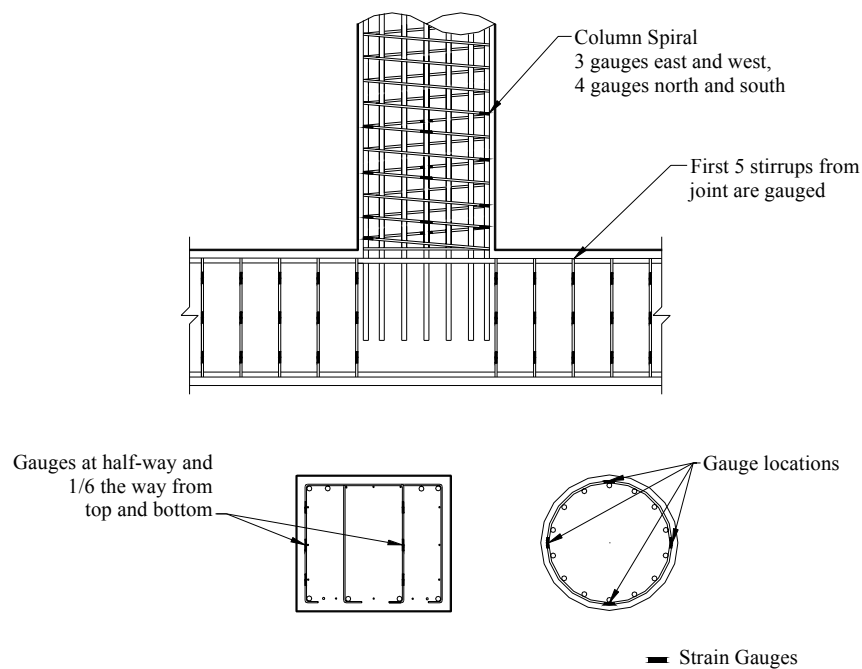


Fig. 4.5 Pre-1971 test units: location of strain gauges on transverse reinforcement

The column spiral was gauged on the north and south sides at four points, approximately 2, 6, 14, and 22 in. from the beam-column interface. Three gauges on the east and west sides were placed at approximately 6, 14, and 22 in. from the soffit. The spiral within the joint on the current design units was gauged five times on the north, south, east, and west sides with the gauges spaced evenly.

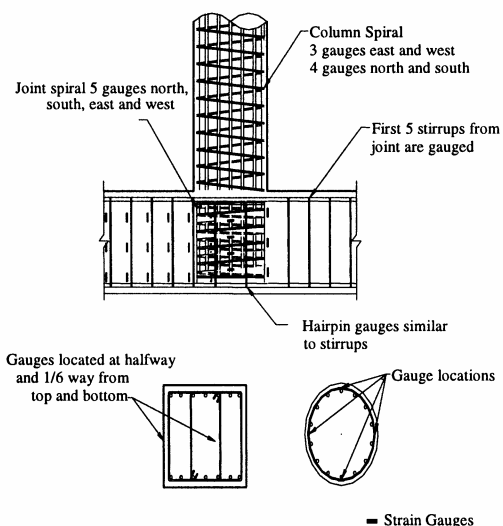


Fig. 4.6 Current design test units: location of strain gauges on transverse reinforcement

4.2 LOADING PROTOCOL

In order to optimize the test results, each design was tested both quasi-statically and dynamically. The quasi-static testing allowed observations to be made throughout the test and comparison made to the quasi-static tests performed by Sritharan (1996). The dynamic test incorporated the information of strain-rate effects caused by higher velocities encountered in a real earthquake. The loading applied to the specimens corresponded to the equivalent displacement at mid-height of the column in the prototype structure. The displacement input sequence was identical for all four specimens. The velocity pulse was applied at the beginning of the test and then followed with cyclic loading that matched the loading of Sritharan (1996). During the quasi-static testing of the pre-1971 units, it was found that the specimens failed earlier in the test than in the current design units. Therefore, the loading protocol was interrupted before it reached the levels seen in the current design tests.

The required axial load representative of the gravity in the column was determined to be 569 kN (128 kips), but Sritharan (1996) decided to use 400 kN (90 kips) for the axial load in the test to obtain the required cap beam moments at the joint interface. This lower value was chosen so the moment ratios in the beam between the model and prototype structures were satisfied at the ultimate strength of the structure.

The generalized pulse loading for this experiment was determined in association with the first year of this project (Cox 2001). Thirty-four near-field time histories containing a velocity pulse were analyzed to determine a mean peak velocity to use for the testing. All of the records were from stations located within 18 km of the fault rupture. The station closest to a fault rupture surface was the Kobe University site with a distance of 0.2 km. The smallest magnitude earthquake represented was the 1966 Parkfield, California, earthquake with a moment magnitude of 6.1. The largest was the 1978 Tabas, Iran, earthquake with a magnitude of 7.4. The maximum peak velocity value was 174 cm/sec from the Kobe earthquake, while the minimum peak velocity was 23 cm/sec from the Parkfield earthquake. The average peak velocity was 94 cm/sec. The maximum pulse duration was 9.3 sec from the Lucerne record, and the minimum was 0.5 sec from the Parkfield earthquake. The average duration was 2.2 sec. The investigation found that on average, the highest peak velocity values occurred during the first half cycle of the pulse, and that the average number of cycles of pulse was one. The typical velocity directivity pulse used to determine the loading protocol was a single cycle occurring at the beginning of the record, with a peak velocity of 100 cm/sec and a duration of approximately 2 sec.

After constructing the average pulse, the response of a nonlinear, simplified bridge column was analyzed using the “Ruaumoko” computer program (Carr 1998). The beam was neglected in the analysis and the column was modeled in a fixed-free condition. The curvature response of the column at the interface of the base of the column was determined from Ruaumoko and then scaled to match the half-scale bridge column to be tested. The equivalent displacement at the top of the column was then determined from the curvature values.

The typical cyclic loading sequence following the pulse was taken from the displacements used in the test performed by Sritharan (1996). As seen in Figure 4.7 the positive peak of the pulse is at a displacement of 6.9 cm (2.71 in.) and the negative peak of the pulse is 1.4 cm (0.55 in.).

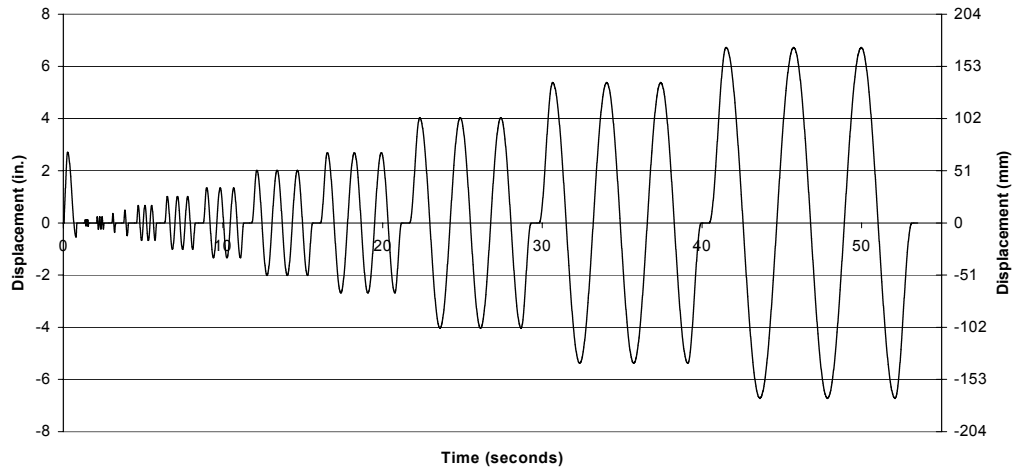


Fig. 4.7 Displacement loading history for test units

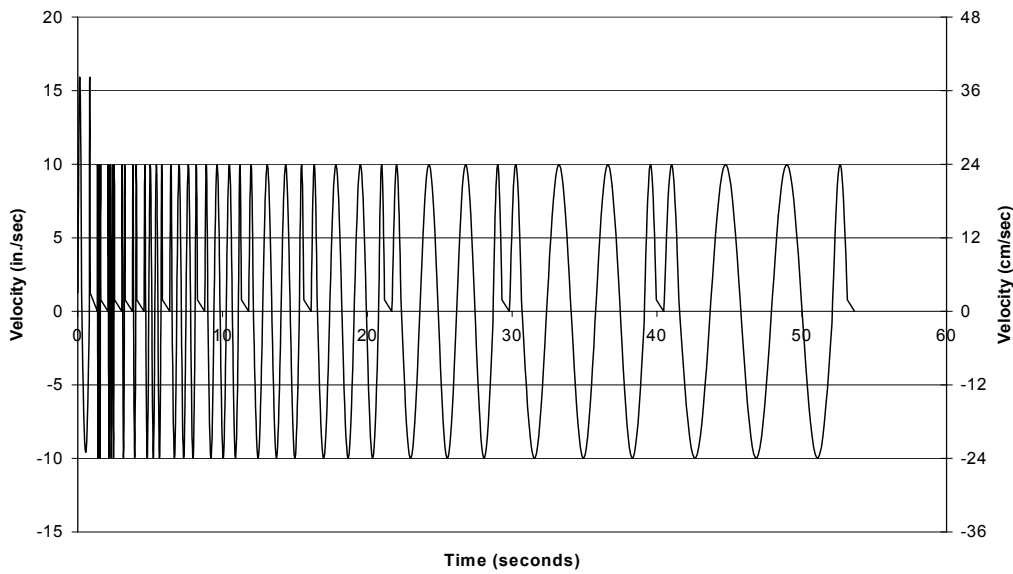


Fig. 4.8 Velocity loading history for test units

The dynamic tests were run with two velocities of loading. The prototype pulse velocity was determined from the Ruaumoko analysis. The velocity was then scaled to the half-scale test unit. The maximum velocity of the test pulse was limited by the capacity of the actuator, which was 40.5 cm/sec (16 in./sec). The peak velocities of the cycles after were all 25.4 cm/sec (10 in./sec). The velocity time history that was used in the test is shown in Figure 4.8.

4.3 TEST PROCEDURE

Each test began with the application of the gravity load. The total gravity load of 400 kN (90 kips) was applied in three increments of 133 kN (30 kips). Each of the two vertical actuators carried half of the total load. The gravity load actuators were then maintained during the test in load control. The gravity load was applied in the same manner for all of the tests. At each increment of load, the specimen was inspected and cracks were marked.

For the quasi-static tests, the pulse was applied to the structure very slowly and the test was paused at the five PEER Bridge Performance Levels, as outlined in Hose (1999), to mark cracks and take photos at each level. These performance levels will be presented again with the results in Chapter 5. The first performance level is the onset of cracking; the second level is yielding of the longitudinal steel. The third level is initiation of the local mechanism. For the current design unit, where failure eventually occurred in the plastic hinge region, the local mechanism refers to the spalling in the plastic hinge region. For the more brittle pre-1971 design, where failure occurred through shear in the joint, the local mechanism was considered to be the diagonal shear cracks in the joint. According to the PEER guidelines, crack widths of 1–2 mm (0.04–0.08 in.), or a length of the spalled region in the plastic hinge greater than 1/10 of the section depth, constitute an initiation of the local mechanism. The first three levels were seen to be reached during the pulse part of the test for both types of specimens. The fourth performance level is the full development of the local mechanism where the crack widths are greater than 2 mm (0.08 in.) or the plastic hinge spalling is greater than 1/2 of the section depth. The fifth level is the point where strength degradation is visible in the test specimen.

When testing the pre-1971 joint, all five levels were seen to occur during the push portion of the positive pulse.

After the pulse, the structure was then cycled at the displacement levels used in the non-pulse test (Sritharan 1996). The first three levels were at 25%, 50%, 75%, and 100% of the displacement at yield. Then the structure was loaded to ductilities equal to 1, 1.5, 2, 3, 4, 6, 8, and 10. At each step, three cycles were applied to observe the stability of the hysteresis loop.

The current design units were loaded until the third cycle at 10 times the yield displacement, before it was decided that there was significant reduction in the force-resisting ability of the system and the test was stopped. The pre-1971 units began to lose strength during

the pulse loading, and after three cycles at 6 times the yield displacement, the test was halted because the strength of the unit was less than 1/4 the original strength.

For the dynamic tests, the two units were tested with the same displacement histories that were used in the quasi-static tests. After the application of the gravity load, the entire displacement record was applied to the test units at the velocities discussed previously. Still cameras and videos were set up to record the test, but the test was not halted at any point.

In the next chapter, the results from the tests will be presented and compared between the four specimens tested for this project and the two specimens tested previously (Sritharan 1996, MacRae 1994).

5 Test Results

The four specimens considered in this report were tested during August and September 2000 in The Charles Lee Powell Structural Testing Laboratories at the University of California, San Diego. This chapter presents photographs taken during the tests, and the reduced experimental data in graphical form.

5.1 MATERIAL PROPERTIES

Prior to the full specimen tests, the material properties of the concrete and reinforcing steel were determined. Concrete cylinders measuring 152.4 mm in diameter x 304.8 mm in height (6 in. x 12 in.) were cast from each concrete pour. The cylinders were tested at 7 days, 28 days, and the day of the specimen test. The results are listed in Table 5.1. Each value in this table represents an average of three unconfined compression tests.

Table 5.1 Compressive strength of concrete cylinders taken from concrete pours

Test #	Description	Member	7 days		28 days		day of test	
			MPa	ksi	MPa	ksi	MPa	ksi
1	Quasi-Static	column	23.7	3.4	31.9	4.6	41.4	6.0
	Current	beam/joint	23.2	3.4	32.8	4.8	41.9	6.1
2	Quasi-Static	column	24.6	3.6	33.4	4.9	40.8	5.9
	Pre-1971	beam/joint	24.5	3.6	34.5	5.0	38.1	5.5
3	Dynamic	column	23.7	3.4	31.9	4.6	43.9	6.4
	Current	beam/joint	23.2	3.4	32.8	4.8	41.2	6.0
4	Dynamic	column	24.6	3.6	33.4	4.9	43.0	6.2
	Pre-1971	beam/joint	24.5	3.6	34.5	5.0	39.7	5.8

The steel reinforcing bars were tested for strength in tension. Uniaxial tension tests were performed on three coupons taken from the reinforcing bars of the column and beam. The

samples obtained from the column and joint spirals were deformed in the process of shaping the spiral; thus they did not have clearly defined yield points. The yield value was taken when the gauge read approximately 2200 $\mu\epsilon$. The results are presented in Table 5.2. Each value is an average of three coupon tests.

Table 5.2 Yield and ultimate strength of steel reinforcing bars

Description	Bar Size (diameter mm)	Yield Strength		Ultimate Strength	
		MPa	ksi	MPa	ksi
Longitudinal Column and Beam Bars	#7 (22.2)	437	63.4	709	102.9
Column Spiral	#3 (9.5)	434	62.9	679	98.4
Joint Spiral	#3 (9.5)	362	52.5	672	97.4
Beam Stirrups- Pre-1971	#2 (6.4)	489	70.9	590	85.6

5.2 GENERAL BEHAVIOR OF TEST SPECIMENS

The test units were simply supported, as discussed in Chapter 4, and subjected to the loading history, as presented in Section 4.2. The experimental observations are documented in this section with photographs taken during the tests. The five bridge performance levels determined for the Pacific Earthquake Engineering Research (PEER) Center by Hose (1999) were described in Section 4.3 and are highlighted below in the table. The PEER performance levels were recorded easily for each quasi-static test because the test could be paused when each new level was observed. The performance levels for the dynamic tests had to be determined after the test from the videos and recorded data. The photographs for the dynamic tests were taken on a timer and the correlation between the pictures and the load level is defined as closely as possible.

Table 5.3 PEER bridge performance levels (Hose 1999)

Level	Performance Level	Qualitative Performance Description	Quantitative Performance Description
I	CRACKING	Onset of hairline cracks	Cracks barely visible.
II	YIELDING	Theoretical first yield of longitudinal reinforcement	Crack widths < 1mm.
III	INITIATION OF LOCAL MECHANISM	Initiation of inelastic deformation. Onset of concrete spalling. Development of diagonal cracks.	Crack widths 1-2 mm. Length of spalled region > 1/10 cross-section depth.
IV	FULL DEVELOPMENT OF LOCAL MECHANISM	Wide crack widths/spalling over full local mechanism region.	Crack widths > 2mm. Diagonal cracks extend over 2/3 cross-section depth. Length of spalled region > 1/2 of cross-section depth.
V	STRENGTH DEGRADATION	Buckling of main reinforcement. Rupture of transverse reinforcement. Crushing of core concrete.	Crack widths > 2mm in concrete core. Measurable dilation > 5% of original member dimension.

Each type of specimen was tested quasi-statically first. The quasi-static tests were stopped intermittently for observations, and the cracks that had formed since the last stop were marked. The ends of the cracks were marked with a hatch mark perpendicular to the crack and labeled with the load level so that the rate of crack propagation could be tracked. Also the rubble was also cleared away from the specimen at each pause to allow an unobstructed view of the joint behavior. The dynamic tests were not paused at all during the loading cycles. After completion of the test, the cracks were all marked so that they could be seen in the photographs.

The description of the tests below is divided into three sections: the application of the dead load, the pulse portion of the load, and the cycling at increasing ductility levels leading up to failure of the specimen. Each section describes and compares the four different tests.

5.2.1 Dead Load Application

The dead load was applied to each test unit by increments of 133 kN (30 kips) until a target dead load of 400 kN (90 kips) was reached. This dead load was maintained for the rest of the test. For all specimens, the first cracks formed vertically in the beam starting at the deck and moving up the east and west sides of the joint when the gravity load reached 267 kN (60 kips). The cracks extended about halfway up the joint as seen in Figure 5.1. The beams first cracked at the same load level for all of the tests and the crack pattern was similar. Figures 5.2–5.5 present the history of the gravity load verses the horizontal displacement of the column for each specimen. It can be observed that for the quasi-static tests, as shown in Figures 5.2 and 5.3, there was very little change in the vertical load. The variation was a maximum of 9 kN (2 kips). The vertical actuators were able to respond to the movement of the horizontal actuator and maintain the vertical load. This was not the case for the dynamic tests, as shown in Figures 5.4 and 5.5. The vertical actuators were not able to keep up with the speed of the horizontal actuator and the load varied greatly from approximately 225 kN (50 kips) to 580 kN (130 kips). The change in vertical load for the higher ductility levels was much lower. By the time that a ductility of four was reached ($\mu=4$), the variation was only 110 kN (25 kips), and by $\mu=8$, the variation was less than 45 kN (10 kips).



Fig. 5.1 Cracking in beam joint from gravity load

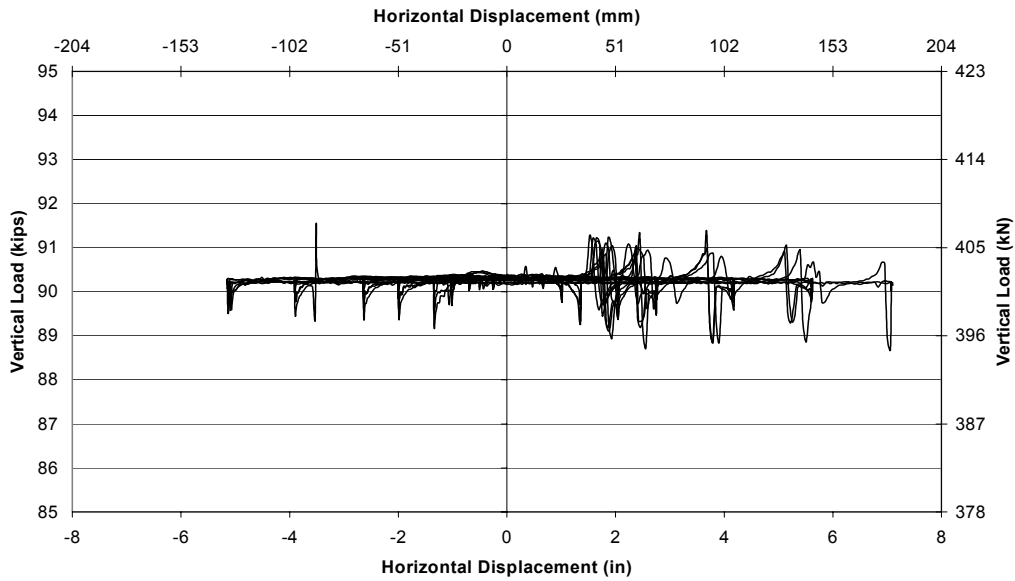


Fig. 5.2 Vertical load history: current design, quasi-static test

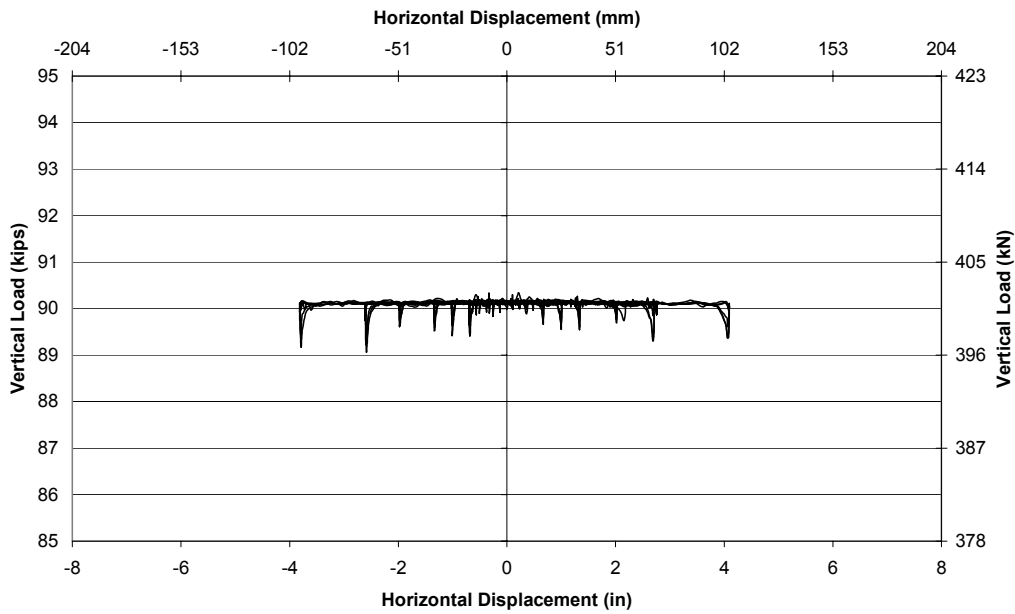


Fig. 5.3 Vertical load history: pre-1971 design, quasi-static test

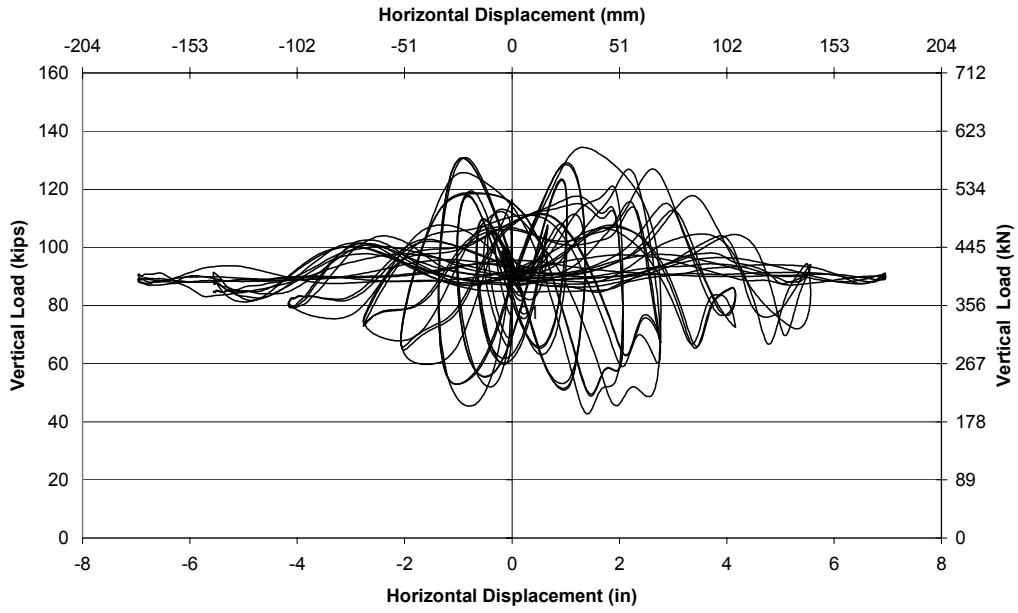


Fig. 5.4 Vertical load history: current design, dynamic test

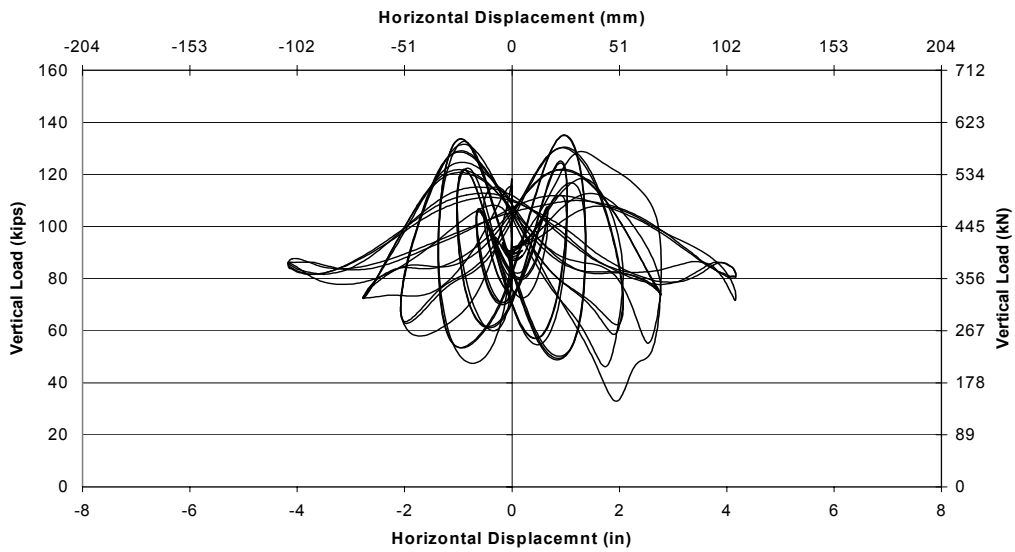


Fig. 5.5 Vertical load history: pre-1971 design, dynamic test

5.2.2 Pulse Application

5.2.2.1 Current Design Specimens

The current design specimens exhibited spalling in the north plastic hinge region and yielding of the column longitudinal bars during application of the pulse. PEER Performance Level I was observed at a displacement around 10 mm (0.4 in.), with horizontal flexural cracks observed up the height of the south side of the column. Level II, the first yield level, occurred in the south column longitudinal bar at a displacement of around 14 mm (0.55 in.). The third performance level is the initiation of the local mechanism, which in the case of the flexural columns corresponds to the formation of a plastic hinge in the column. At a positive displacement of 47 mm (1.85 in.), Level III was observed in the column.

At the positive peak of the pulse for the quasi-static test specimen, the north plastic hinge region showed spalling of the cover concrete 102 mm (4 in.) up the column from the beam, as shown in Figure 5.6. The negative pulse (in the pull direction) was much smaller than the positive pulse, and as expected there was less damage. Horizontal flexural cracks were seen up the full height of the column on both sides, but only spalling at the north base of the column occurred. There was minor cracking in the joint with more cracks caused by the positive pulse than the negative pulse.

During the dynamic test, the pulse caused spalling of the column cover concrete in the north plastic hinge over a distance of 152 mm (6 in.), as shown in Figure 5.7.

There was no visible damage in the south plastic hinge region. There was also no visible cracking seen in the joint during the dynamic test.

5.2.2.2 Pre-1971 Specimens

The pre-1971 specimens exhibited major shear cracking in the joint region and a reduction in load-carrying capacity by the peak of the positive pulse. The columns showed flexural cracking, but the cracks never reached the width of the cracks seen in the current design specimens. The first performance level, corresponding to diagonal shear cracking in the joint, was observed at a displacement of 8 mm (0.33 in.). Levels II, and III were recorded at the same displacement of 29 mm (1.15 in.). The shear cracks in the joint had reached a width of 1.6 mm (0.06 in.) and the longitudinal rebar in the beam deck had reached yield strain. At the peak of the positive pulse, Performance Level V was observed, as shown in Figure 5.9. The cracks in the joint had reached

a width of 4 mm (0.16 in.) and the strength of the specimen had begun to reduce. The joint showed some movement along a shear plane that had formed during the beginning of the pulse loading.

The negative pulse caused less damage than the positive pulse. At the peak of the negative pulse, the cracks in the joint were 1.2 mm (0.05 in.) wide and there was minor spalling of the concrete in the joint. Performance Levels I, II, and III were recorded in the negative direction. Cracking occurred in the negative direction, and the deck bars on the south side of the beam yielded during the unloading of the positive pulse. At a displacement of -8 mm (-0.3 in.) the cracks in the joint exceeded 1 mm (0.04 in.) (Level III). A greater number of cracks formed due to the positive loading than to the negative loading. The column showed minor damage, with some flaking and spalling of the cover concrete in the north plastic hinge region extending about 2 in. from the beam. The northern-most column longitudinal bar also yielded during the positive pulse.

During the dynamic test, the positive pulse caused many large full-length shear cracks, but the negative pulse caused only one full-length diagonal crack, as shown in Figure 5.8. The shear damage in the negative direction was later concentrated along this crack. Small amounts of flaking and spalling of the concrete occurred along the shear cracks in the joint. The specimen also began to lose strength before the peak of the positive pulse. There was minor flaking of the north plastic hinge region of the column, but the south plastic hinge showed no damage at the end of the negative pulse. Overall, the behavior of the specimen during the pulse loading was similar for the dynamic and quasi-static tests.



Fig. 5.6 Peak of positive pulse: current design, quasi-static test



Fig. 5.7 Peak of pulse: current design, dynamic test



Fig. 5.8 Peak of pulse: pre-1971 design, dynamic test

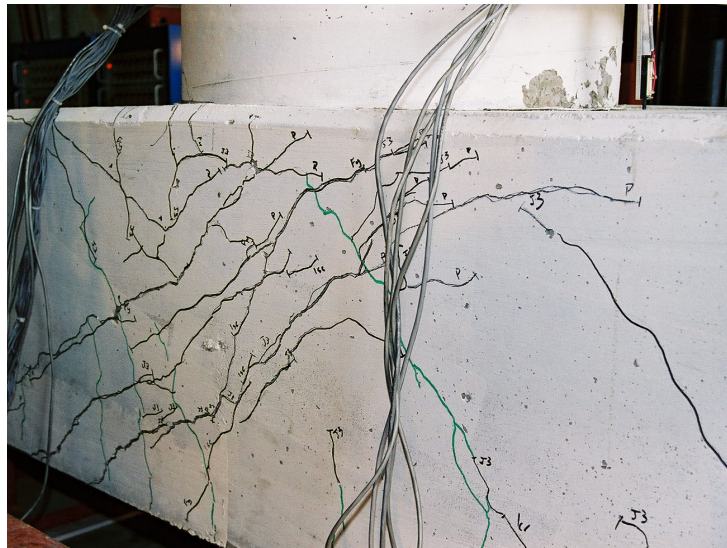


Fig. 5.9 Peak of positive pulse: pre-1971 design, quasi-static test

5.2.3 Cyclic Loading

All four specimens were loaded with the same displacement history as described in Section 4.2. The current design specimens showed large amounts of flexural hinging in the column with less damage in the joint region. The pre-1971 specimens degraded quickly in the joint, and other than minor flexure cracks in the column, showed little column damage.

5.2.3.1 Current Design Specimens

During the quasi-static test, the flexural cracks increased in number and length around the column. By the third cycle of $\mu=3$ the specimen had reached Performance Level IV, with the spalling in the north plastic hinge region extending 305 mm (12 in.) up from the beam, as shown in Figure 5.10. At this point, there was also a small amount of spalling in the south plastic hinge region. It was observed at this load level that the horizontal force was causing the beam to lift off its base about 1 mm (0.05 in.) at the south support. Owing to construction tolerances, some room for movement existed between the steel pin and the supporting link. When the horizontal force from the actuator exceeded the overturning weight of the specimen, the south end of the beam shifted. A few cracks developed at the support regions, but the movement did not seem to affect the results of the rest of the test.

By $\mu=6$ the south plastic hinge was spalling over a height of 127 mm (5 in.), as shown in Figure 5.11. Shear cracks in the joint region had reached 0.8 mm (0.03 in.). The beginning of Performance Level V behavior was observed in the column at the third cycle of $\mu=6$ when flexure cracks had reached 2 mm (0.08 in.) in width. Later cycling produced reduced strength in the column, confirming that Level V had been reached. The plastic hinge regions continued to enlarge, and there was cracking and spalling of the concrete in the beam soffit on the south side of the column base. At $\mu=6$, the bars in the deck side of the beam (the lower side of the beam in the test setup) also yielded.

The dynamic test showed increasing damage to the plastic hinge region and the width of the cracks in the column, but very little damage to the joint. Small shear cracks were seen to open and close in the joint, but at the end of the tests the residual crack width was a maximum of 0.3 mm (0.01 in.). There was no spalling of the concrete in the joint. The size of the spalled region in the plastic hinge was approximately the same as in the quasi-static test until $\mu=3$. At

$\mu=4$, the spalling in the north plastic hinge region, extended 178 mm (7 in.) from the beam. Flaking of the concrete, and large flexural cracks in the column were seen over a height about 483 mm (19 in.) from the beam, as shown in Figure 5.12.



Fig. 5.10 North plastic hinge: $\mu=3$ current design, quasi-static test



Fig. 5.11 South plastic hinge: $\mu=6$ current design, quasi-static test



Fig. 5.12 North plastic hinge: $\mu=6$ dynamic test

5.2.3.2 Pre-1971 Specimens

Most of the main shear cracks in the joint formed during the pulse, and the subsequent damage during the cyclic loading was concentrated along the existing cracks. The joint was seen to shift along these shear planes, and small chunks of concrete fell out of the cracks. Since all five performance levels had been reached by the end of the pulse loading, the strength degradation of the specimens continued during the cyclic loading.

During the quasi-static test, the shear cracks in the joint reached a width of 4 mm (0.16 in.) by $\mu=2$. The region bounded by the shear cracks in the joint began to jut out 4 mm (0.16 in.) from the plane of the beam. By $\mu=3$ the cracks in the joint were wider than 5 mm (0.2 in.), and there was flaking at the south base of the column. At $\mu=4$, the main crack in the joint had reached a width of 38 mm (1.5 in.) and there was more movement along that plane, as shown in Figure 5.13.

The dynamic test progressed similarly to the quasi-static test. After the pulse very few new shear cracks formed. The cracks that formed during the pulse widened with each ductility level, and spalling began around $\mu=2$ with small concrete pieces falling out of the cracks. At $\mu=4$, the face concrete in the joint began to break up into chunks, and the shear plane extended through the joint and the top of the beam (Fig. 5.14).

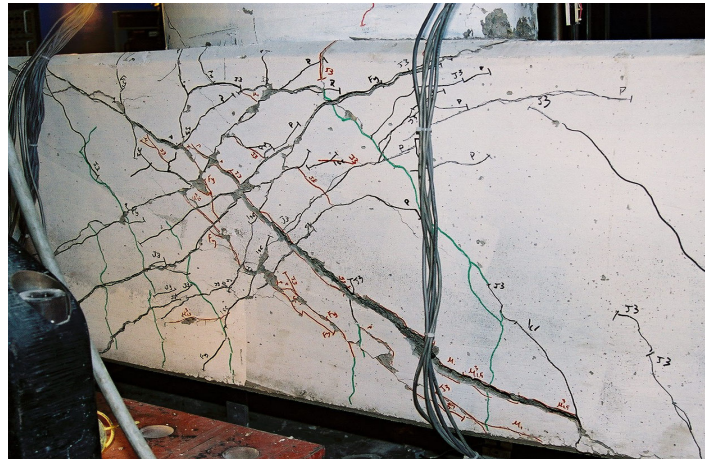


Fig. 5.13 Cracking in joint: $\mu=4$, pre-1971 design, quasi-static test



Fig. 5.14 Joint around $\mu=4$: pre-1971 design, dynamic test

5.2.4 Final Stages of Test

5.2.4.1 Current Design Specimens

The failure mechanism for both the quasi-static and dynamic current design test specimens was the same. During the quasi-static test, the longitudinal column bars in the north plastic hinge region began to buckle out during the cycles of $\mu=8$. The northern-most longitudinal bar in the column broke during the 3rd cycle of $\mu=8$. The longitudinal bar fractured in the space between the column spiral bars. Although the spiral stretched noticeably, it did not break by the end of the test, as shown in Figure 5.15. After the longitudinal bar fracture, the test was continued for two more cycles to view the degrading behavior. The south longitudinal bars buckled severely, and the two northern bars, adjacent to the first fractured bar, also fractured in the last two cycles of the loading. During the quasi-static test, the joint was damaged and spalling occurred, but the greater amount of the damage was focused in the plastic hinge regions of the column, as shown in Figure 5.16. The spalled region of the north plastic hinge was shorter and extended deeper into the column core than in the south plastic hinge. The south hinge seemed to form as would be expected under typical cyclic loading.

The failure in the dynamic test was much more dramatic. During the second positive push at $\mu=8$, the spiral bar fractured in the north plastic hinge region. After the fracture of the spiral, the concrete in the core began to degrade quickly. The north and south column longitudinal bars could easily be seen to buckle out and back during the following cycles. By the end of the test, the three most northern and southern column longitudinal bars had fractured. From viewing the tests, however, it was difficult to tell exactly when. The difference between the quasi-static and the dynamic tests of the current design was most visible in the eventual failures. The spiral fractured in the dynamic test, and after that, the degrading concrete seemed to pour out of the plastic hinge region, as shown in Figure 5.17. During the cycles of $\mu=8$, the spalling in the south hinge increased from a height of 76 mm (3 in.) to 483 mm (19 in.). Column shear cracks were seen to form in the bottom third of the column on the east and west side.

The column shifted along the shear cracks during the cycles of $\mu=8$. The joint showed minimal damage after completion of the test, as shown in Figure 5.18.

The interesting difference between the dynamic and quasi-static tests was the behavior in the joint region. The quasi-static test had much more damage in the joint than during the dynamic test. Two deck bars in the beam began to yield at $\mu=6$ during the quasi-static test, but

the strains in the deck during the dynamic test were not as high, and no longitudinal beam bars yielded.



Fig. 5.15 Current design after quasi-static test (north is right)



Fig. 5.16 Current design after quasi-static test (north is left)



Fig. 5.17 Failure of dynamic current design (view from north)



Fig. 5.18 Current design after dynamic test (north is left)

5.2.4.2 Pre-1971 Specimens

The two pre-1971 specimens exhibited joint failure at the end of the tests. No bars fractured during either the quasi-static or dynamic test. The end of the test was determined by spalling of

large chunks of concrete, a more than 50% reduction in horizontal capacity of the column, and the visible degradation of the interior concrete in the joint region.

During the quasi-static test, there were three main cracks running from the beam soffit on the north side of the column to the deck on the south side of the column. These cracks formed during the pulse and were the focus of the degradation from the push loading. In the pull direction only one main crack formed from the south soffit to the north deck during the negative pulse, and the degradation in that direction occurred on that plane. At $\mu=6$, large chunks of concrete began to spall off the face and soffit of the beam, and the joint shifted enough along the main crack so that it couldn't close again on the return cycle, as shown in Figure 5.19.

The beam reinforcing was visible in the joint at this point. The beam longitudinal bars in the joint region of the soffit buckled out of plane, spalling the concrete off the edges of the beam.

The test was stopped at the end of the third cycle of $\mu=6$ (Fig. 5.20) because the horizontal strength had degraded by more than 50%.

The dynamic test exhibited much more concrete spalling in the joint than in the quasi-static test. At $\mu=4$ the concrete in the joint began to visibly break up, and at $\mu=6$ the core concrete began to pour out of the joint, as shown in Figure 5.21. The joint shifted along the main shear plane and then jutted out at the deck side of the beam. The soffit concrete flaked and broke apart at the base of the column. The test was stopped at the third cycle of $\mu=6$ to match the loading of the quasi-static test, as shown in Figure 5.22.



Fig. 5.19 Pre-1971 joint after quasi-static test (east view of joint)



Fig. 5.20 Pre-1971 specimen after quasi-static test (north is right)



Fig. 5.21 Pre-1971 joint at failure of dynamic test (view from north)



Fig. 5.22 Pre-1971 specimen after dynamic test (north is right)

5.3 GLOBAL HYSTERETIC BEHAVIOR OF TEST SPECIMENS

The global horizontal force-displacement curves for the tests are presented and discussed in this section. The force was measured from the horizontal actuator, and the displacement for the two quasi-static tests was measured from the linear potentiometer at the north side of the load stub as described in Section 4.1. For the dynamic tests, the applied displacement was measured at the horizontal actuator due to the required speed of loading. The yield displacement of 12.4 mm (0.489 in.) that was taken from Sritharan (1996) was shown to be adequate for this investigation. The average displacement from the four tests measured at the first yield of the longitudinal steel in the column was 12.7 mm (0.5 in.), which is very close to that used in that loading protocol. The ductility levels were found as described in Section 4.3, which was taken from the tests performed by Sritharan (1996).

The first two graphs show the non-pulse tests that were performed prior to this investigation. The specimen that is being called “pre-1971” was investigated by MacRae (1994) and was described in Chapter 3. The force-displacement relationship (Fig. 5.23) shows a degrading stiffness after $\mu=2$ until the test was stopped at $\mu=8$, when the lateral strength of the column was one third of the original. The non-pulse test of the current design specimen was performed by Sritharan (1996). The force-displacement time history is shown in Figure 5.24. The initial stiffnesses of the two tests are similar. At $\mu=1$, the load and displacement levels are similar, but the current design specimen exhibits increased strength at higher levels of displacement until an ultimate load of 409 kN (92 kips) at $\mu=6$. The pre-1971 specimen begins to lose strength after a maximum load of 302 kN (68 kips) at $\mu=2$. The loops of the current design specimen are much fatter; therefore the specimen is dissipating more energy than the more pinched loops of the pre-1971 design.

The strength of the current design specimen during the pulse was similar to the maximum capacity of the non-pulse test. The non-pulse test did not reach its maximum capacity until $\mu=6$, whereas the maximum load for the pulse tests was observed during the initial push at around 50 mm (2 in.), as shown in Figures 5.25 and 5.26. The two pulse tests for the current design specimens were very similar in their hysteretic behavior. Both had reduced strength after the pulse, but by the third cycle of $\mu=8$ all of the current design specimens were exhibiting similar strengths as in the non-pulse test.

The pre-1971 units were much more affected by the pulse than the current design specimens. During the pulse, the specimens reached higher loads than in the non-pulse test, but after the pulse the capacity was around half of the initial strength as shown in Figures 5.27 and 5.28. The loads reached during the pulse were similar for the current design and the pre-1971 specimens, but before the maximum displacement of the pulse, the pre-1971 units began to lose strength. The cyclic loops in the positive direction are pinched after the pulse and begin to flatten out by $\mu=3$. In the negative direction the hysteresis loops are more regular, but they never reach the strength that was seen in the negative direction of the non-pulse test.

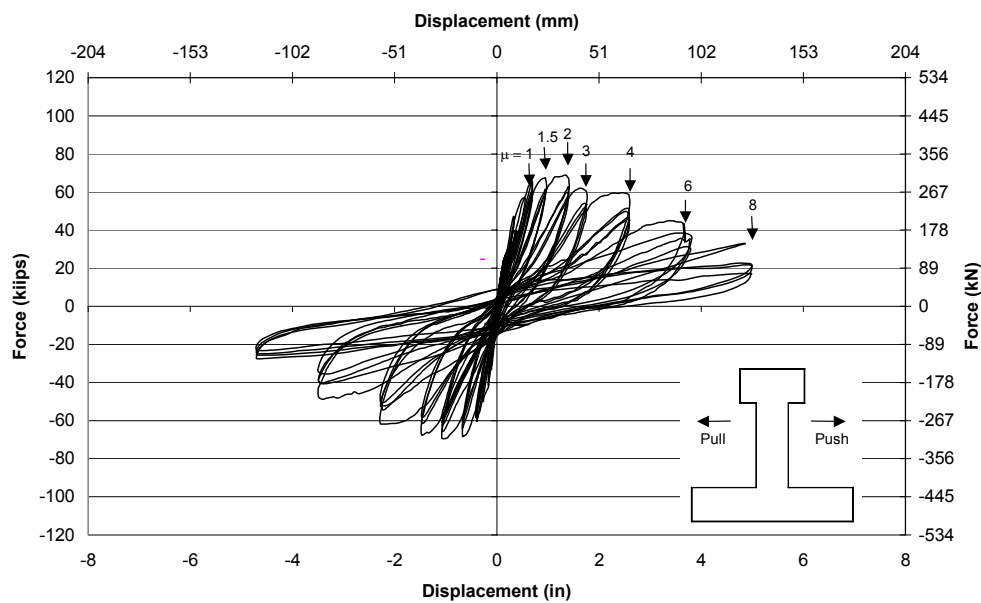


Fig. 5.23 Force-displacement history: non-pulse test, pre-1971 specimen (MacRae 1994)

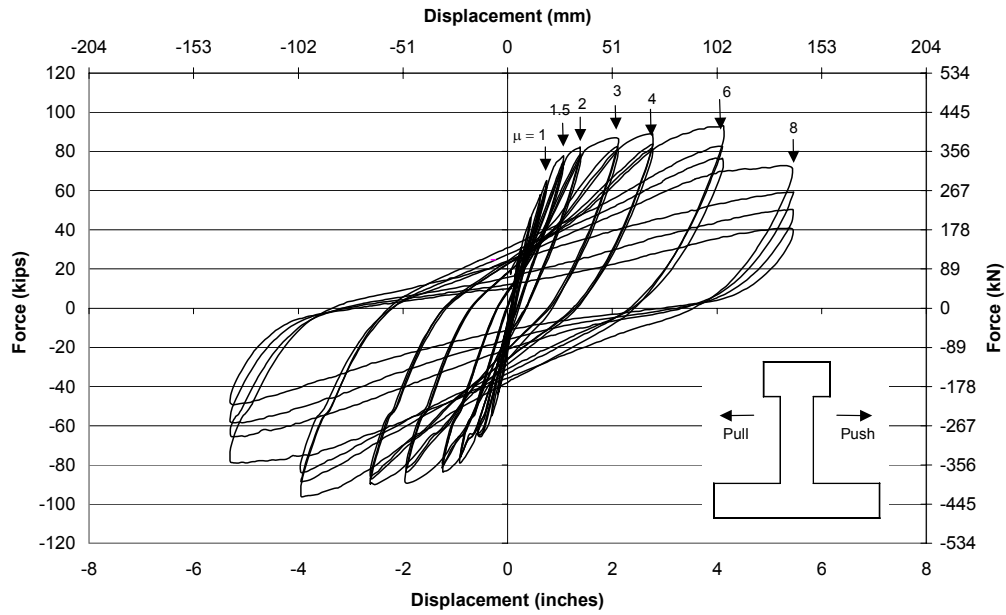


Fig. 5.24 Force-displacement history: non-pulse test, current design specimen (Sritharan 1996)

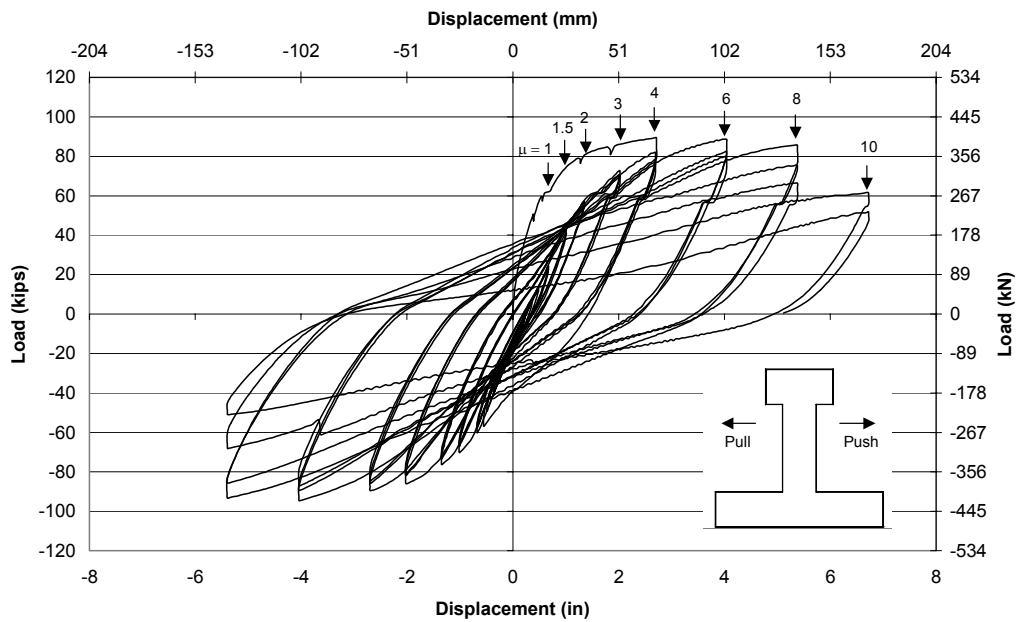


Fig. 5.25 Force-displacement history: current design specimen, quasi-static test

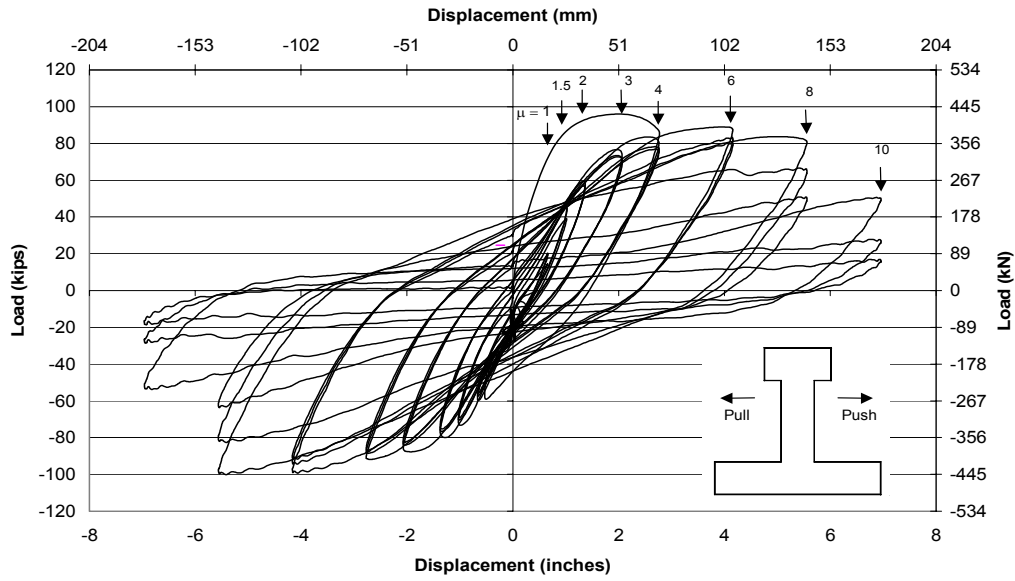


Fig. 5.26 Force-displacement history: current design specimen, dynamic test

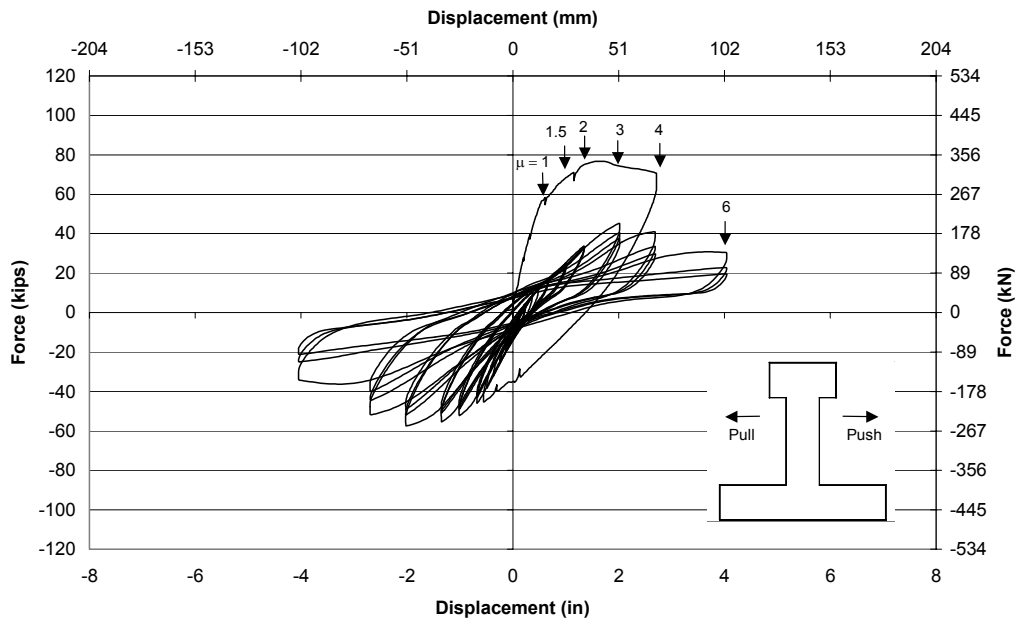


Fig. 5.27 Force-displacement history: pre-1971 specimen, quasi-static test

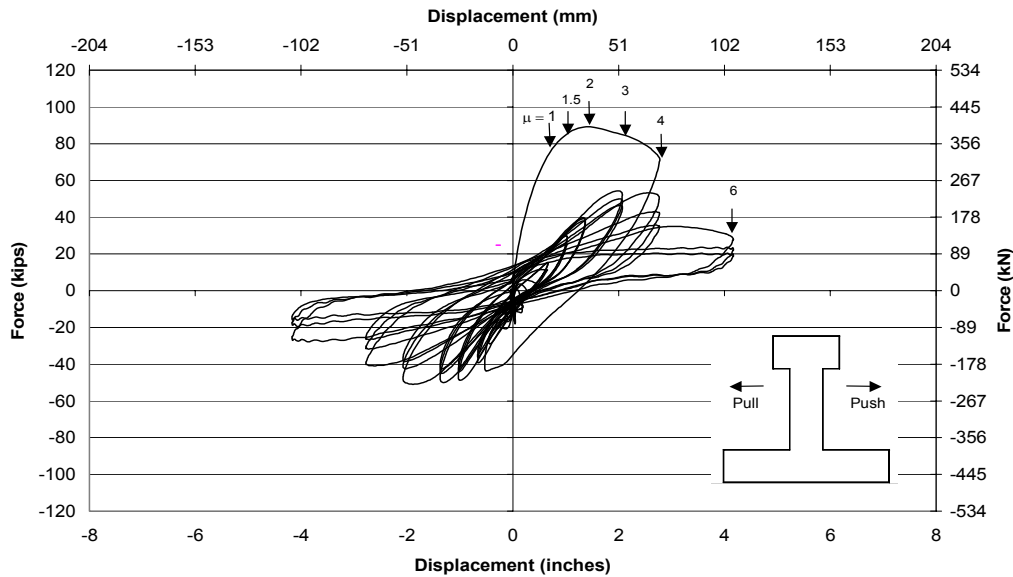


Fig. 5.28 Force-displacement history: pre-1971 specimen, dynamic test

5.4 ENERGY ABSORBED BY TEST SPECIMENS

The energy absorbed by the test specimens is determined from the force-displacement time history. The hysteresis loops are integrated to find the area inside each loop. The trapezoidal integration rule is used as shown below in Equation 5.1, where E_i is the energy at the given time step and E_{i+1} is the cumulative energy at the next time step, V_i is the force from the horizontal actuator at the given time step, and V_{i+1} is the horizontal force from the actuator at the next time step. Δ_i is the horizontal displacement of the column at the given time step, and Δ_{i+1} is the horizontal displacement at the next time step. After the absorbed energy was determined for each test, all six tests were graphed in Figure 5.29. Since the data taken for the quasi-static tests were not at the same time step as for the dynamic tests, the energy absorbed by the quasi-static tests had to be plotted versus a pseudo-time. This pseudo-time was determined so that the peaks of the cycles occurred at the same time as the peaks in the two dynamic tests. The energy is additive, so the peaks represent the energy absorbed into the structure during the loading portion of the cycle, and the valleys represent the elastic energy restored to the system on the unloading part of the cycle. Since the structure is yielding, the total energy is not restored and the graph slopes upward.

$$E_{i+1} = \left(\frac{V_i + V_{i+1}}{2} \right) (\Delta_{i+1} - \Delta_i) + E_i \quad (5.1)$$

The current design specimens absorbed much more energy than the pre-1971 specimens. This was expected after viewing the difference in the shape of the force-displacement hysteresis loops. Both designs absorbed more energy during the dynamic tests than in the quasi-static tests. The current design non-pulse test was similar to the pulse test until $\mu=8$ when the non-pulse test began to absorb less energy. During the non-pulse cycling at $\mu=8$, recordings indicated that large joint shear deformation occurred that was consistent with an observed drop in horizontal force resistance. Much more concrete degradation and spalling was seen in the joint region during the non-pulse test than during the pulse tests of the current design specimen. Since more energy was absorbed overall during the pulse tests than during the non-pulse tests, it can be inferred that the pulse loading was not overly detrimental to the final behavior of the specimen.

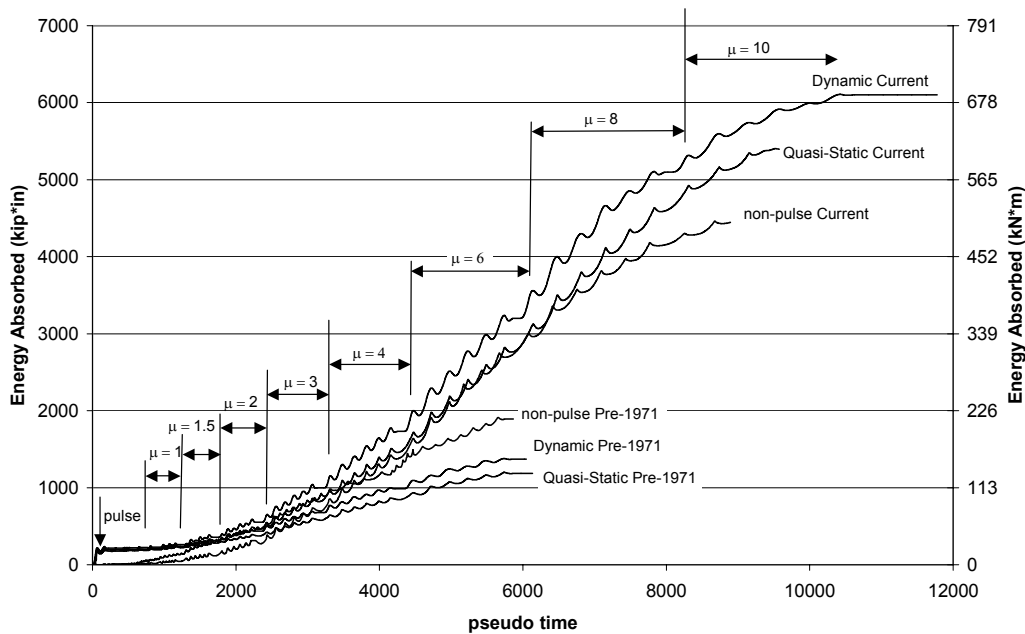


Fig. 5.29 Energy absorbed by test specimens

The pulse loading caused a spike in the energy plot that was equal for all of the pulse tests. The pre-1971 specimens absorbed less energy than did the current design specimens but the non-pulse pre-1971 unit behaved practically equally to that of the current design until the second cycle of $\mu=4$, when it began to diverge. The pulse-tested pre-1971 specimens absorbed

more energy than did the non-pulse specimens in the beginning during the pulse loading, but very little after the pulse and therefore ended up absorbing less energy over all.

5.5 EQUIVALENT VISCOUS DAMPING RATIO OF TEST SPECIMENS

The displacement-based design method (Priestley 1996) represents bridge structures as single-degree-of-freedom structures with an equivalent stiffness and an equivalent viscous damping ratio. The damping ratio used is an approximated value taken from testing data. The equivalent viscous damping ratio of the specimen, ξ_{eq} , is computed from the force-displacement time history using:

$$\xi_{eq} = \frac{A_h}{2\pi V_m \Delta_m} \quad (5.2)$$

A_h is the area of the hysteresis loop (the same as the energy computed in 5.4), V_m is the maximum horizontal force from the actuator for each cycle, and Δ_m is the maximum horizontal displacement at that cycle.

The results of these equivalent viscous damping computations are presented in Figures 5.30–5.33. During all the tests, the damping that was computed for the pulse loading was similar (about 25% of critical). By $\mu=8$ and $\mu=10$ the damping in the cycles was close to that of the pulse for the current design specimens. The pre-1971 specimens exhibited an increase in damping from $\mu=1$ to $\mu=6$, but never reached the damping levels seen during the pulse. There is very little difference between the damping seen in the quasi-static and the dynamic tests, although for the dynamic tests, the damping is a little higher overall.

At a displacement of $\mu=4$, the same displacement as the pulse, the damping in the system for the current design was on average 70% of the damping during the pulse cycle. In the pre-1971 specimens the damping at $\mu=4$ averages 55% of the damping during the pulse.

The first cycle of the lower ductility levels had a higher damping than did the later cycles. The later ductility levels showed some increase in damping in the second and third cycles. This is due to the reduction in strength of the specimen during the later cycles.

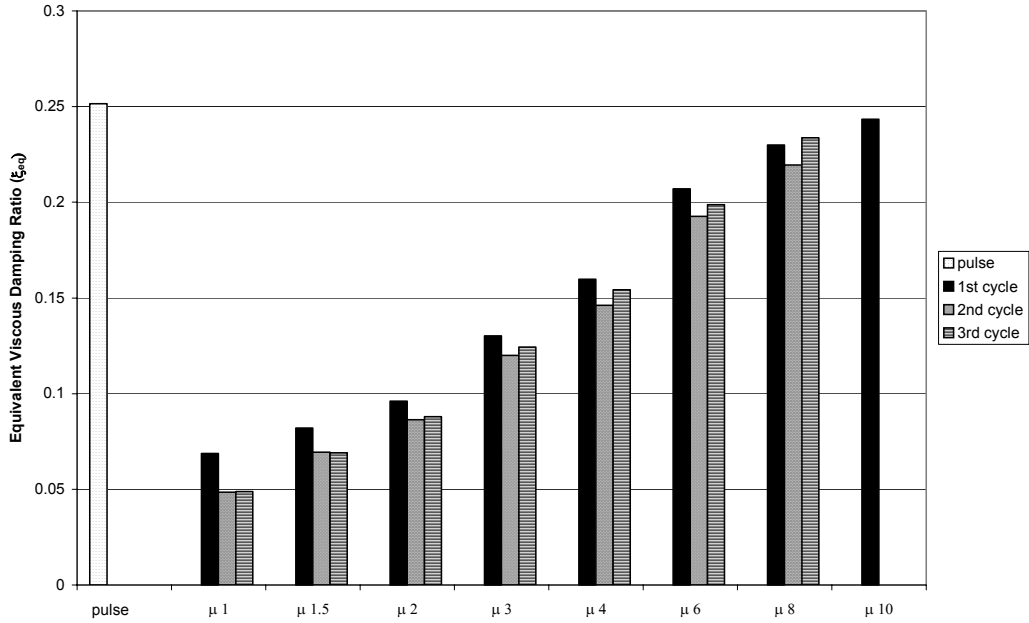


Fig. 5.30 Equivalent viscous damping ratios: current design specimen, quasi-static test

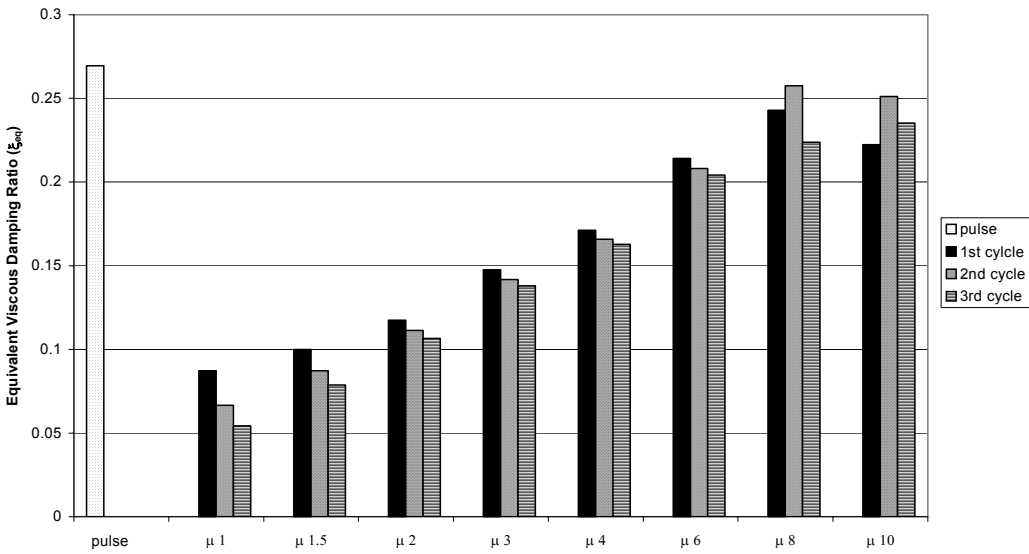


Fig. 5.31 Equivalent viscous damping ratios: current design specimen, dynamic test

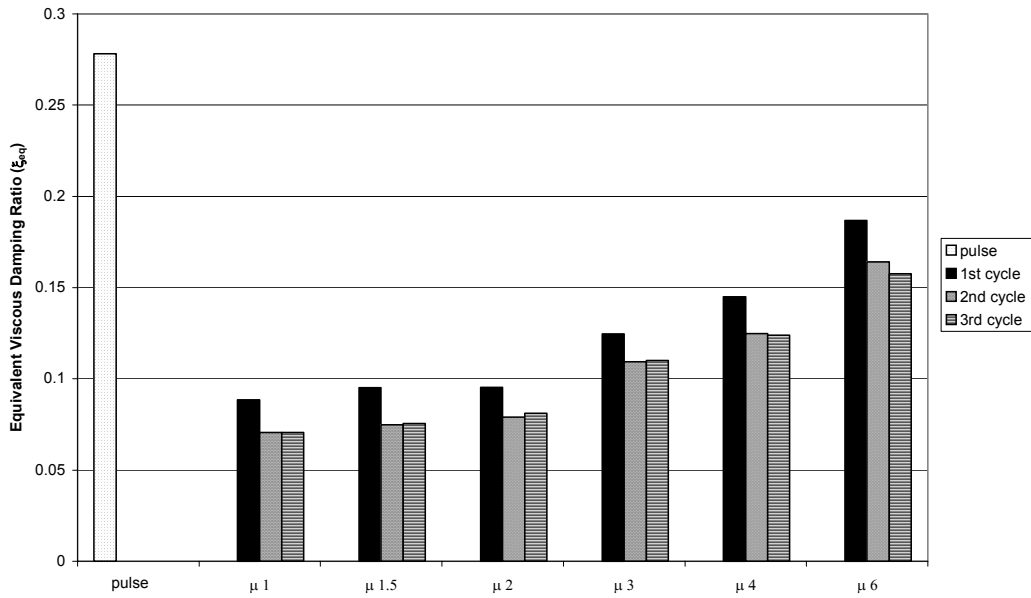


Fig. 5.32 Equivalent viscous damping ratios: pre-1971 specimen, quasi-static test

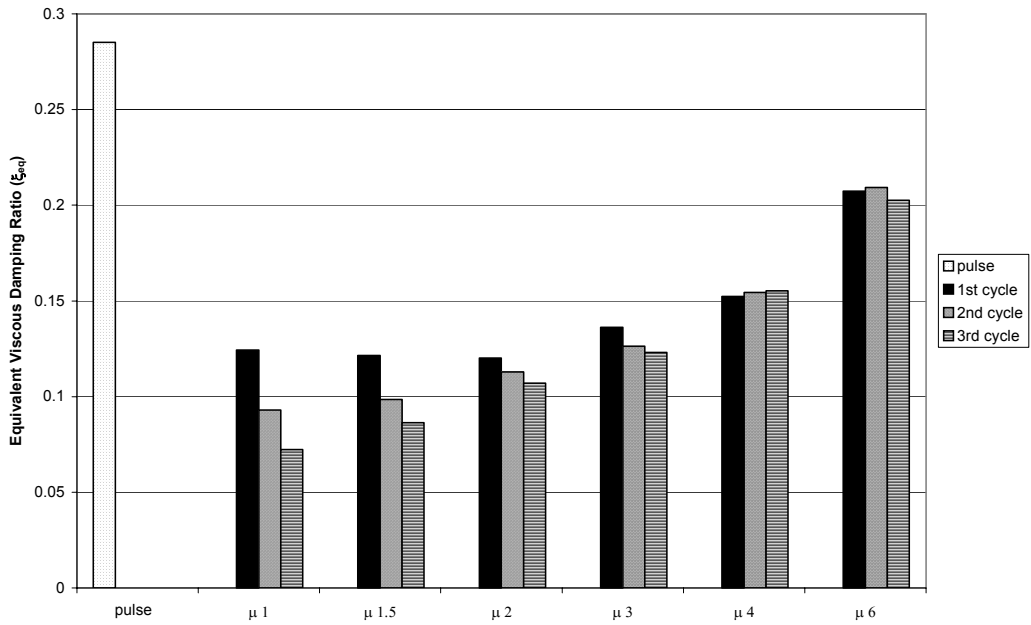


Fig. 5.33 Equivalent viscous damping ratios: pre-1971 specimen, dynamic test

5.6 STIFFNESS DEGRADATION OF TEST SPECIMENS

When creating a model for the analysis and design of bridges, an equivalent stiffness is used in the single-degree-of-freedom representation. This stiffness is a value estimated for the structure from experimental data. The secant stiffness of each hysteretic cycle of each test, K_{eq} , was computed from:

$$K_{eq} = \frac{(|V_{max}| + |V_{min}|)}{(|\Delta_{max}| + |\Delta_{min}|)} \quad (5.3)$$

V_{max} is the maximum horizontal load for that cycle and V_{min} is the minimum horizontal load for that cycle. Similarly Δ_{max} is the maximum horizontal displacement of the column during the given cycle, and Δ_{min} is the minimum horizontal displacement for that cycle.

The stiffness for each cycle was graphed against the ductility level for each test, as shown in Figures 5.34–5.37. The stiffness visibly degraded throughout the tests. The dynamic tests were less stiff overall than the quasi-static tests; this could be due to the greater damage seen earlier on in the dynamic tests. The stiffness during the pulse was the same for the quasi-static and dynamic tests, but the current design units were stiffer than for the pre-1971 units. This is a result of the increased deformations in the joints of the pre-1971 specimens.

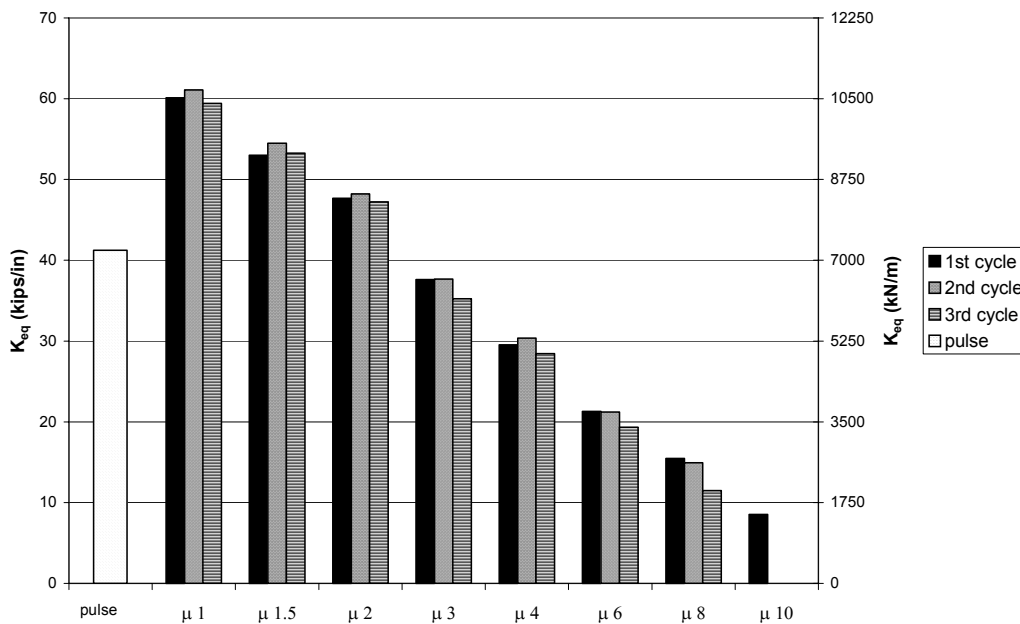


Fig. 5.34 Secant stiffness: current design specimen, quasi-static test

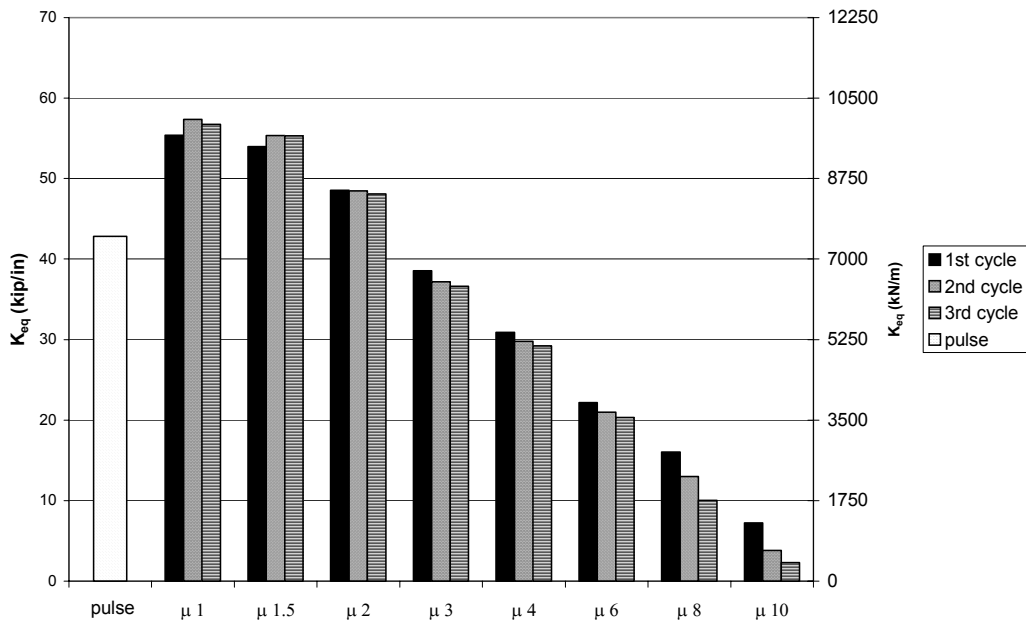


Fig. 5.35 Secant stiffness: current design specimen, dynamic test

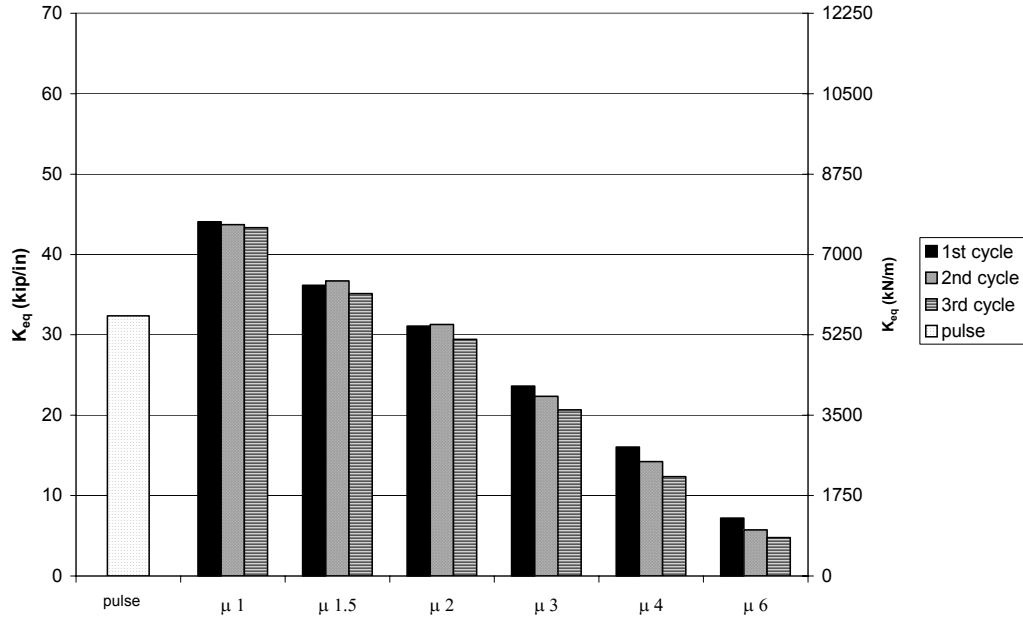


Fig. 5.36 Secant stiffness: pre-1971 specimen, quasi-static test

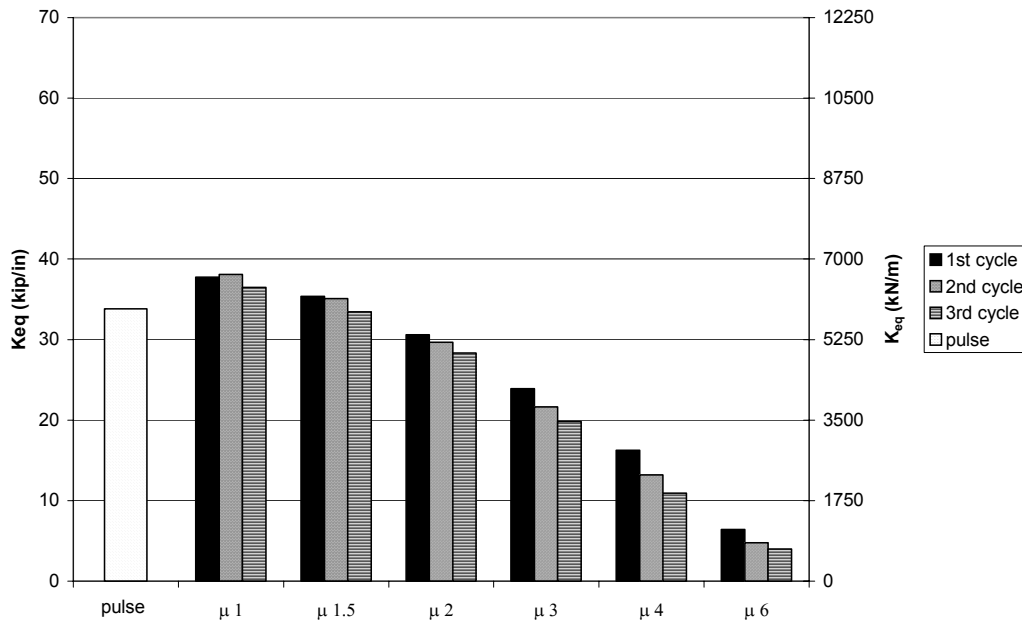


Fig. 5.37 Secant stiffness: pre-1971 specimen, dynamic test

5.7 MOMENT-CURVATURE RELATIONSHIPS OF TEST SPECIMENS

Each column was instrumented with matched pairs of linear potentiometers as described in Section 4.1.1. The maximum curvature of the column occurred at the intersection of the column and the beam; thus the pair of potentiometers at the base of the column was used to find the curvature for this section. The displacement measured by the north potentiometer (Δ_N) and the south potentiometer (Δ_S) can be transformed to an average curvature ϕ , by:

$$\phi = \frac{\Delta_N - \Delta_S}{h_c l_g} \quad (5.4)$$

h_c is the horizontal distance between the potentiometers and l_g is the gauge length.

The curvature was plotted against the maximum moment in the column. The maximum moment at the base of the column was calculated from the horizontal force in the actuator times the distance from the actuator loading point to the soffit of the beam. For these specimens, that distance was 1829 mm (72 in.).

The size and shape of the moment-curvature hysteresis loops illustrate the energy dissipated in flexure by the test units. These resulting moment-curvature relationships are

presented in Figures 5.38–5.41. The current design specimens dissipated much more energy in flexure than the pre-1971 specimens. The curvature values are greater and the loops of the moment-curvature graphs are larger. The pre-1971 units conversely have very thin hysteresis loops. The maximum curvature for the pre-1971 units was about 65% of the curvature seen in the current design units. The dynamic test for the pre-1971 unit exhibited very little curvature in the column. The pulse portion of the load caused similar responses for all specimens. After the pulse, the pre-1971 units show little flexural behavior, whereas the current design specimens showed greater flexural behavior.

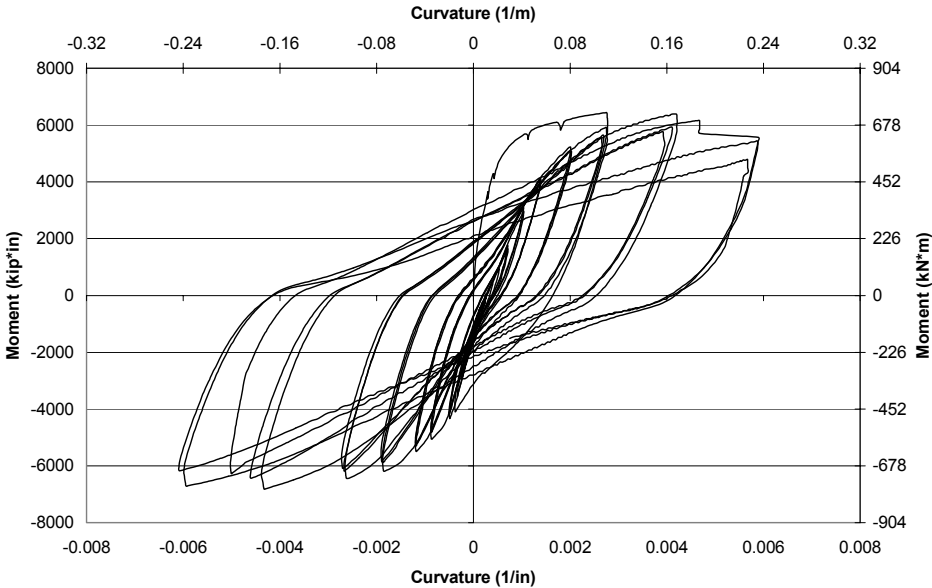


Fig. 5.38 Moment-curvature history: current design specimen, quasi-static test

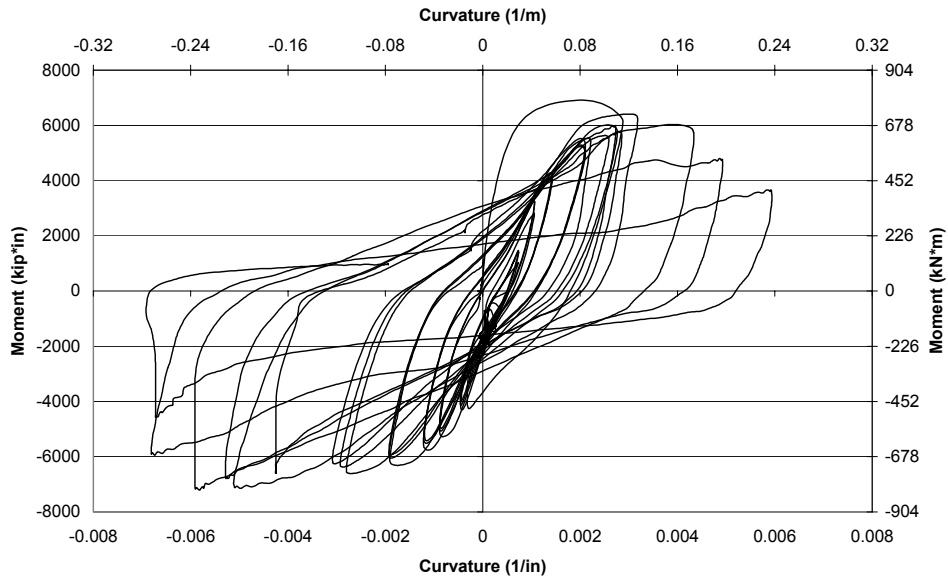


Fig. 5.39 Moment-curvature history: current design specimen, dynamic test

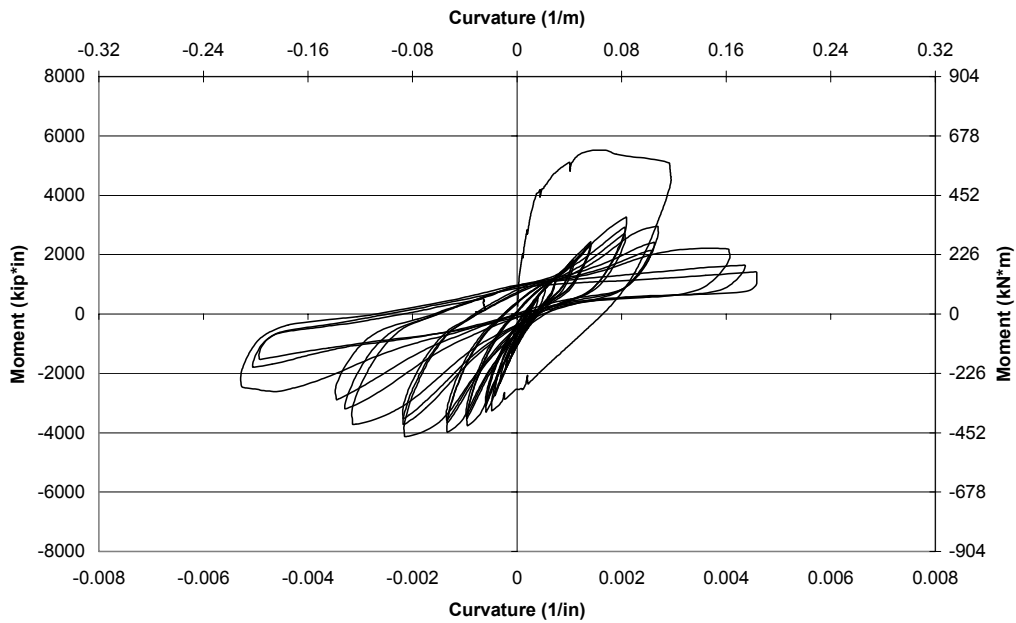


Fig. 5.40 Moment-curvature history: pre-1971 specimen quasi-static test

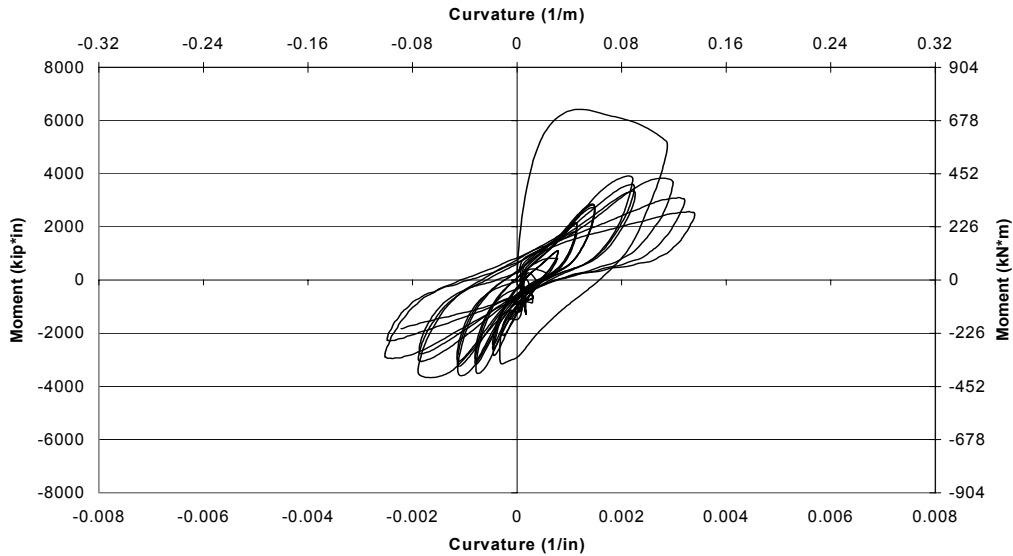


Fig. 5.41 Moment-curvature history: pre-1971 specimen, dynamic test

5.8 CURVATURE DISTRIBUTION IN COLUMNS

The columns were instrumented with linear potentiometers over a height of 939 mm (37 in.). This was illustrated in Figure 4.2. As described in Section 5.7 (Equation 5.4), the maximum average curvature was determined at each potentiometer location and plotted against the height up the column from the beam. This calculation was performed at the first cycle of each ductility level. The curvature is plotted on these graphs only until $\mu=4$. During the current design tests, the spalling of the concrete and the degradation of the concrete in the core of the column might have rendered the data taken from the later cycles inaccurate. The resulting curvature distributions in the columns are presented in Figures 5.42–5.45.

The maximum curvature in the column, for all of the tests, occurred at the intersection with the beam. The current design specimens, which had much more spalling and degradation over the height of the column, showed greater curvature in the column base. The pre-1971 specimens measured substantial curvature at the column-beam intersection, but the curvature in the rest of the column was very small compared to the current design specimen. The positive pulse that measures approximately the same horizontal displacement as the cycle of $\mu=4$ had practically the same curvature as that seen during the cycles of $\mu=4$ for all four tests.

In comparing the dynamic and static tests, the pre-1971 units showed a little more curvature in the column during the quasi-static test than in the dynamic test. The current design specimens recorded higher curvature at higher gauge heights during the dynamic test, but the maximum curvature at the base was the same for the two tests.

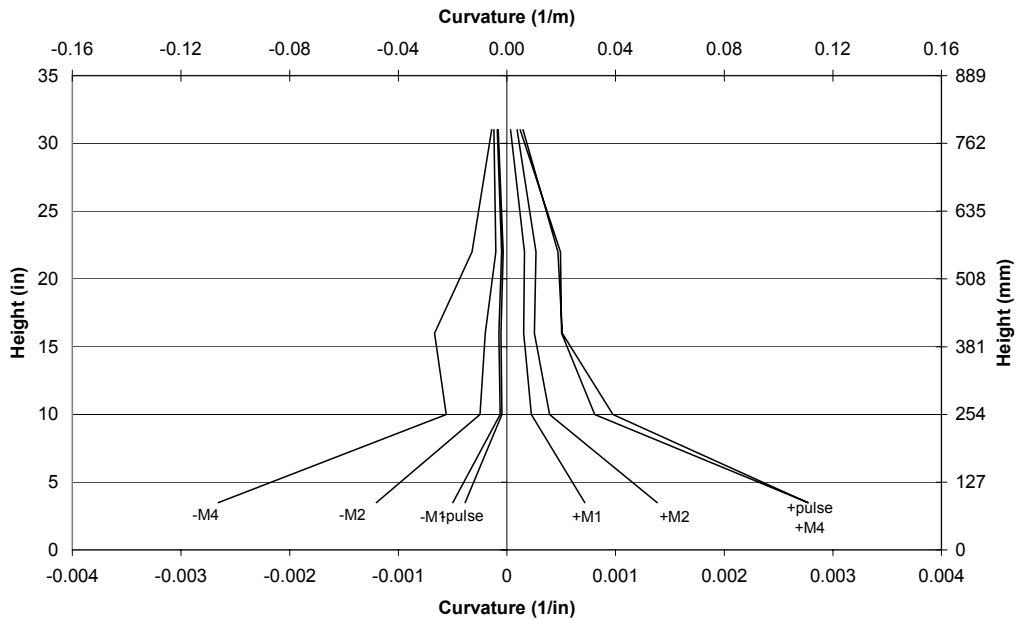


Fig. 5.42 Curvature distribution in column: current design specimen, quasi-static test

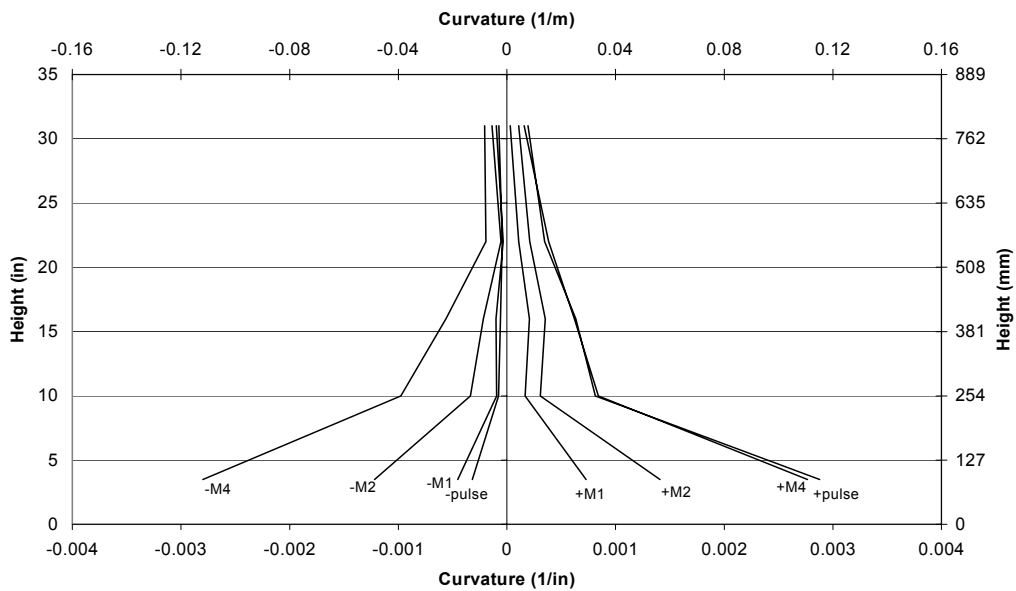


Fig. 5.43 Curvature distribution: current design specimen, dynamic test

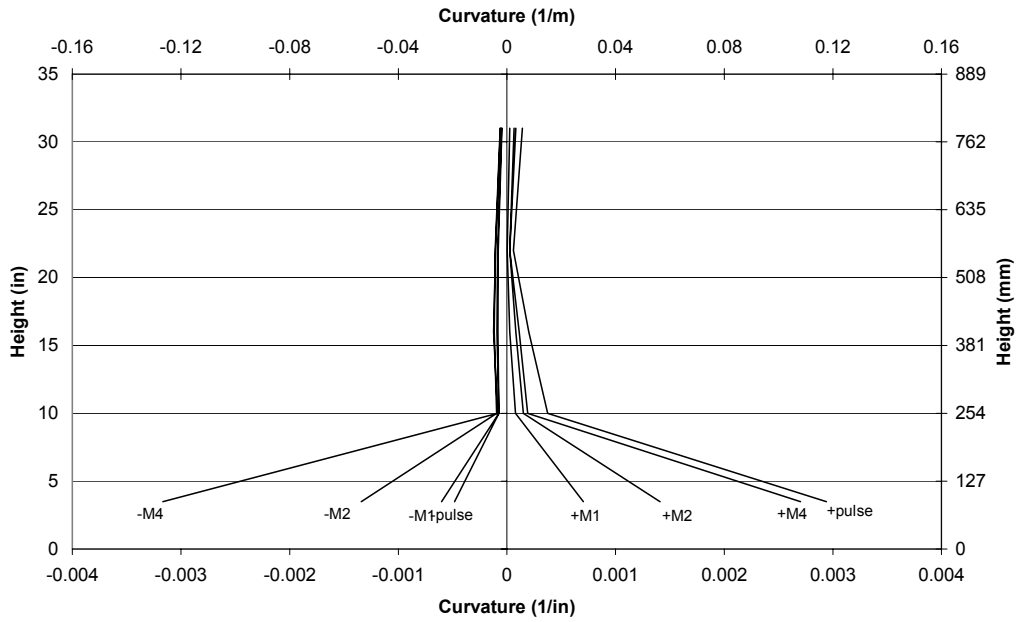


Fig. 5.44 Curvature distribution: pre-1971 specimen, quasi-static test

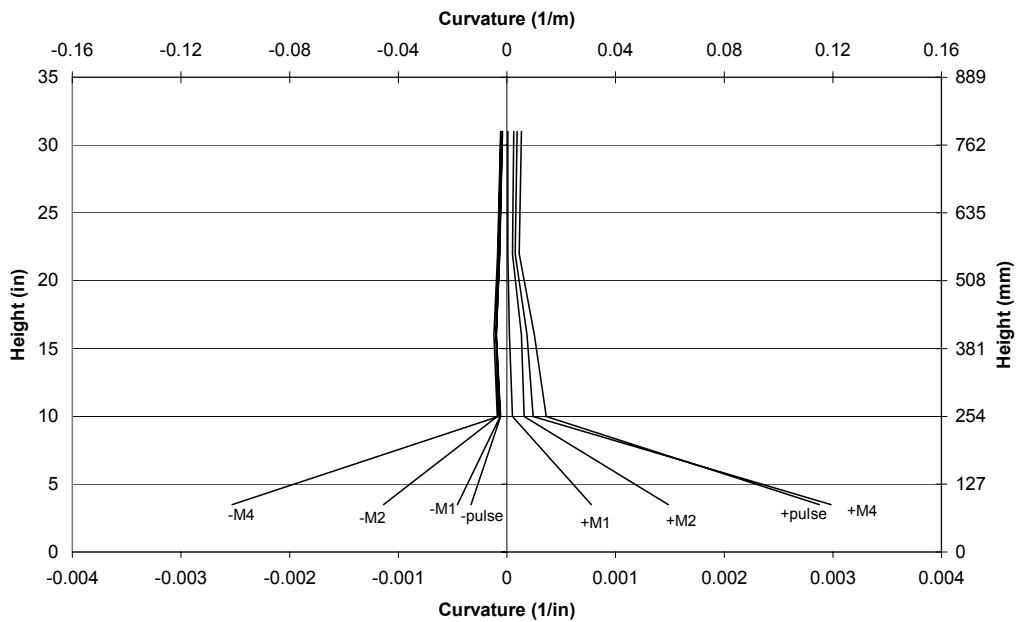


Fig. 5.45 Curvature distribution: pre-1971 specimen, dynamic test

5.9 MEASURED PLASTIC HINGE LENGTHS

As was seen in the previous section, the inelastic flexural behavior of each column was concentrated at the end of the column adjacent to the beam. The experimental plastic hinge length can be calculated from the curvature at the column base and the plastic displacement recorded at the top of the column. The calculation for the total displacement at the top of the column, Δ , is shown in Equation 5.8. This is a function of the plastic displacement taken from the plastic curvature, $\phi_p = (\phi - \phi_y)$, acting over the plastic hinge length (L_p) added to the elastic displacement (Δ_y). The elastic displacement was recorded during the tests, as described in Section 5.4, and then used to calculate the yield curvature, ϕ_y , with Equation 5.7. The total displacement equation was then rewritten to express the plastic hinge length, L_p , in terms of ductility level (μ), yield displacement (Δ_y) and curvature (ϕ).

$$L_p = 0.08L + 0.022 f_y d_{bl} \geq 0.044 f_y d_{bl} \quad (f_y \text{ in MPa}) \quad (5.5)$$

$$\Delta = \frac{\phi L^2}{3} \quad \text{for } \phi \leq \phi_y \quad (5.6)$$

$$\phi_y = \frac{3\Delta_y}{L^2} \quad (5.7)$$

$$\Delta = (\phi - \phi_y) L_p \left(L - \frac{L_p}{2} \right) + \Delta_y \quad (5.8)$$

$$L_p = L - \sqrt{L^2 - 2(\mu - 1) \frac{\Delta_y}{(\phi - \phi_y)}} \quad (5.9)$$

Before testing, the plastic hinge length was predicted by Equation 5.5 (Priestley 1996). The predicted value of 363 mm (14.3 in.) is close to the actual values that were calculated from the test data. The first values that were computed were for $\mu=2$ because it was assumed that before that level, a plastic hinge has not fully formed. The values for the higher ductilities of 8 and 10 are not likely to be accurate, as the concrete in the plastic hinge regions began to spall and could have displaced the linear plots mounted on the edges of the column. The plastic hinge length is fairly constant for all of the tests, as can be seen in Figure 5.46.

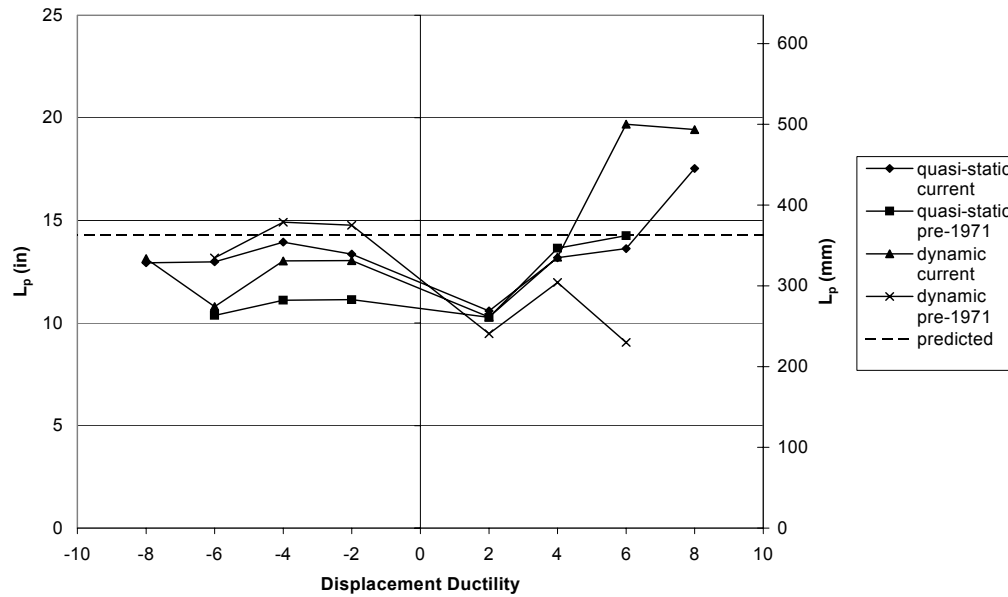


Fig. 5.46 Evolution of plastic hinge length with displacement ductility

5.10 CYCLIC SHEAR BEHAVIOR OF JOINTS

Linear potentiometers were placed on the face of the beam in the joint area to measure the deformation of the joint as described in Section 4.1.1. The joint horizontal movement was determined from a procedure developed by Sritharan (1996), illustrated below in Figure 5.47. The change in length of the vertical gauge (S), the horizontal gauge (B), and the diagonal gauge (D) determined the rotation of the shear panel, and thus the global horizontal shear deformation of the joint (Δ_1) can be obtained by Equations 5.10–5.15.

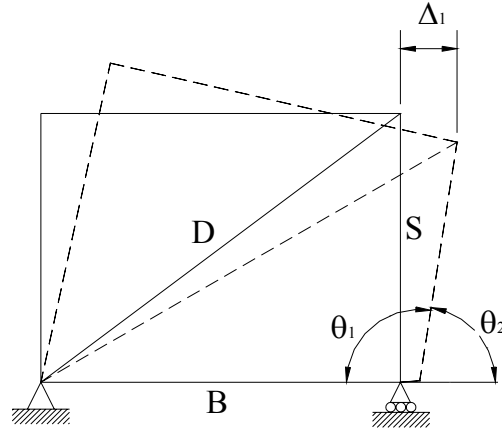


Fig. 5.47 Original and deformed geometry of shear measurement in joint

$$S = S_0 + \Delta S \quad (5.10)$$

$$D = D_0 + \Delta D \quad (5.11)$$

$$B = B_0 + \Delta B \quad (5.12)$$

$$\theta_1 = \cos^{-1} \left(\frac{B^2 + S^2 - D^2}{2BS} \right) \quad (5.13)$$

$$\theta_2 = \pi - \theta_1 \quad (5.14)$$

$$\Delta_1 = S \cos \theta_2 \quad (5.15)$$

Figures 5.48–5.51 present the global shear deformation in the joint against the shear load applied to the joint by the horizontal actuator. The joints of the current design deformed much less than the pre-1971 joints. The joint of the current design dynamic test had almost no damage at all, and as expected the joint deformation was almost undetectable, as shown in Figure 5.49. Although the current design quasi-static test (Fig. 5.48) exhibited some movement in the joint, the shear stiffness was high until $\mu=8$ when the concrete cracks in joint began to widen. After $\mu=8$, the degradation of the joint began to dissipate a small amount of energy in shear shown in the pinched loops of the last four cycles. The pre-1971 joints exhibited much more movement than the current design. Figures 5.50 and 5.51 clearly show the deformation of the joint during the pulse and then the continued movement during the remainder of the cyclic loading. A shear deformation of 10 mm (0.4 in.) was seen in both specimens by $\mu=6$. The pulse portion of the test caused a large amount of damage in the positive direction with the later cycling at much lower

load level. The quasi-static pre-1971 test degraded slowly, with large amounts of energy dissipation in shear as seen by the large loops of Figure 5.50. The dynamic test of the pre-1971 dissipated more shear energy during the pulse than in the quasi-static test, but then during the cyclic loading the loops were very pinched and flattened out quickly, as shown in Figure 5.51.

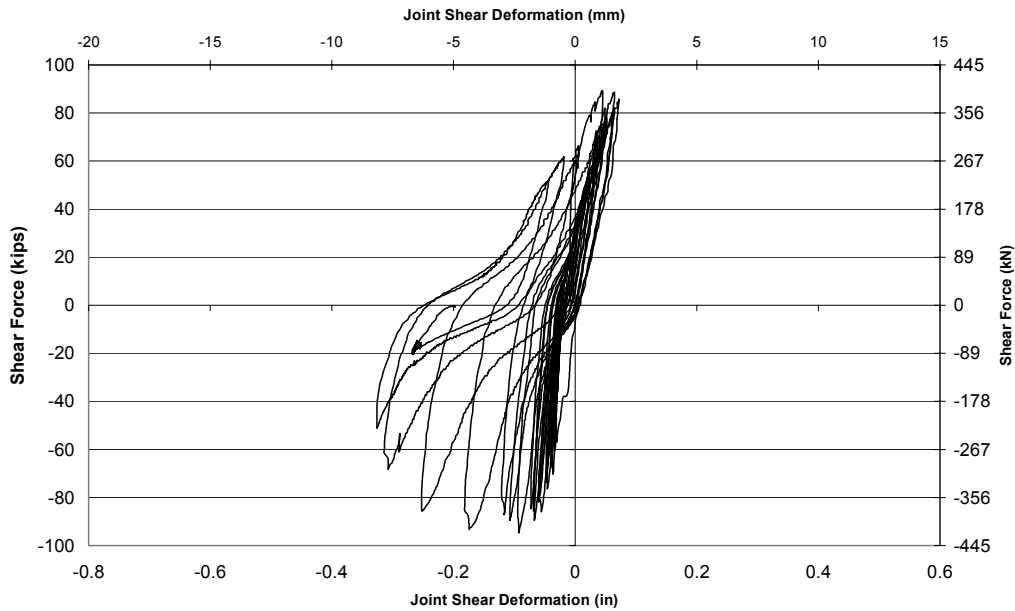


Fig. 5.48 Joint shear deformation history: current design specimen, quasi-static test

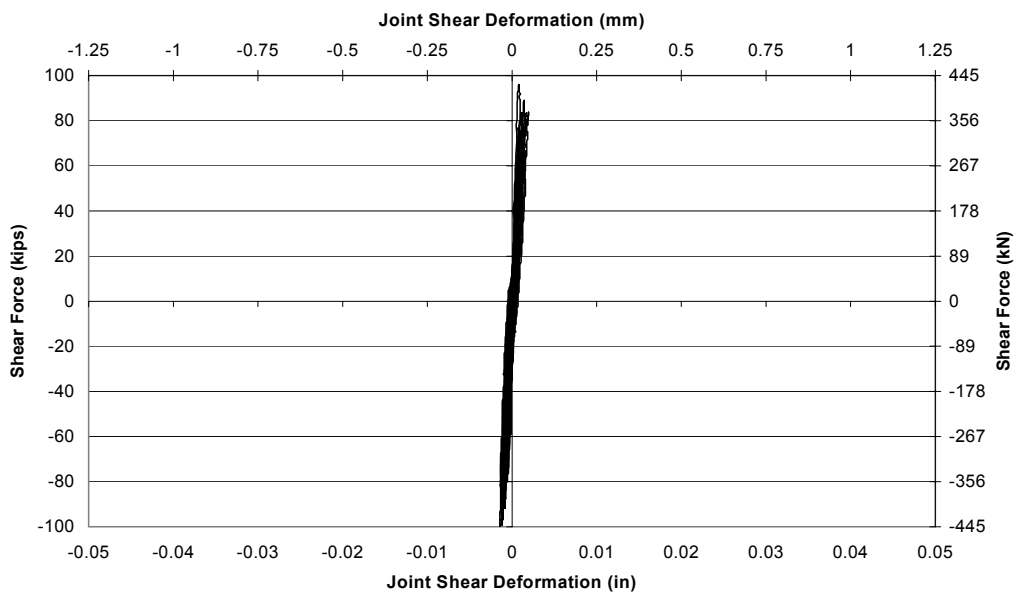


Fig. 5.49 Joint shear deformation history: current design specimen, dynamic test

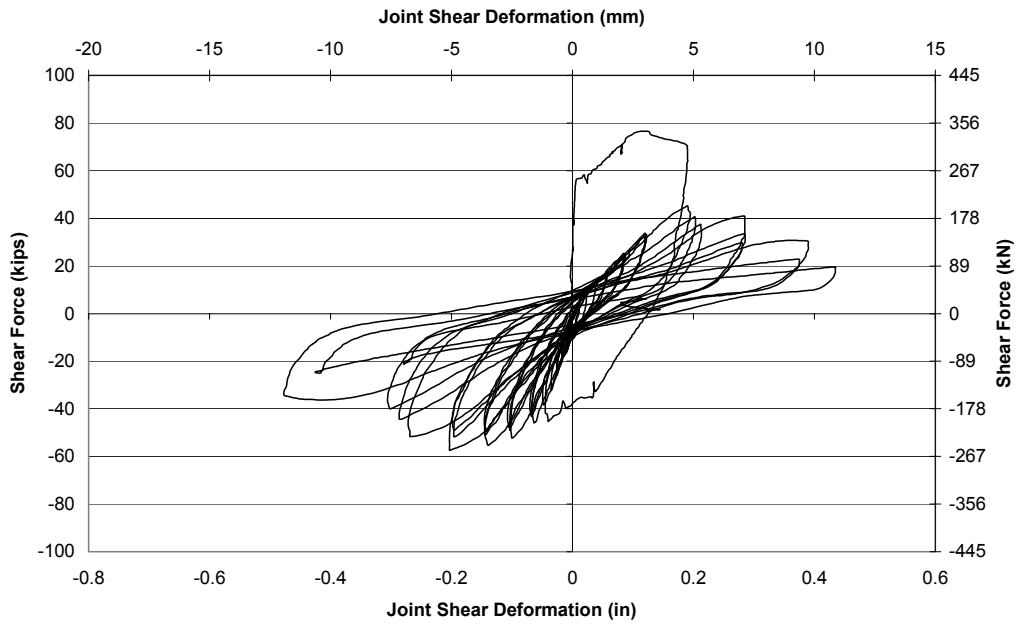


Fig. 5.50 Joint shear deformation history: pre-1971 specimen, quasi-static test

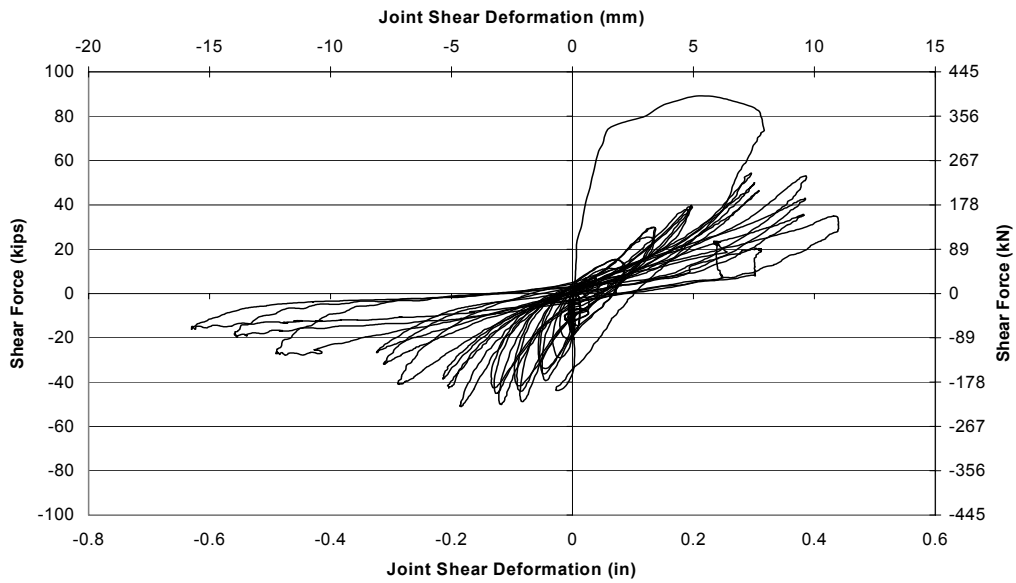


Fig. 5.51 Joint shear deformation history: pre-1971 specimen, dynamic test

5.11 STRAIN-RATE DISTRIBUTION IN REINFORCING BARS

The column longitudinal bars were instrumented with strain gauges as described in Section 4.1.2. The strain rate in the bars was computed as the change in strain over each time step. Plotted below are the graphs of the strain-rate history of the south column longitudinal bar (Fig. 5.52) and the north column longitudinal bar (Fig. 5.53) during the pulse loading. The south bar is in tension during the positive portion of the pulse and shows strain rates 40% higher than that of the north bar that in the south bar is associated with the strain gauge located 152 mm (6 in.) up from the compression during the positive pulse. The graph is shown for the beam interface. The strain gauge located directly at the beam-column interface did not function properly. The strain rate for the cyclic portion of the test is shown in Figures 5.54-5.55. By $\mu=4$, the strain rate had reached about half of the value seen during the pulse.

The rate of the strain in the specimens can affect their behavior. This concept was discussed in Section 2.3, and equations were presented to include the effects of strain rate in the determination of material properties for use in analysis. The data presented in this section will be used in the next chapter to try to determine more accurate values for the concrete and steel properties during dynamic testing. The revised properties should improve the predicted moment-curvature response for comparison with the recorded test values.

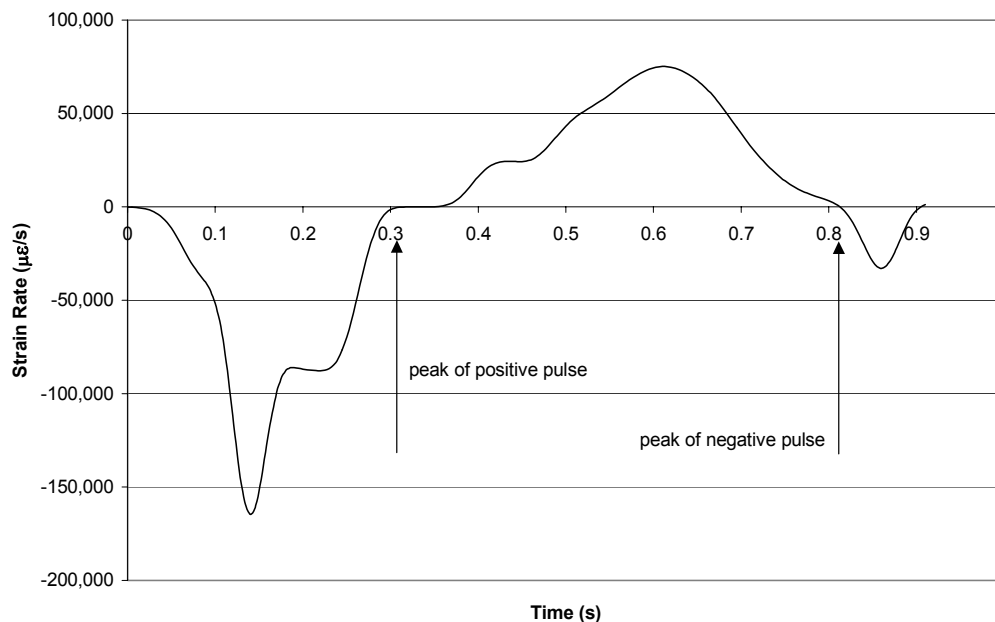


Fig. 5.52 Strain-rate time-history: south column longitudinal bar, pulse of current design specimen, dynamic test

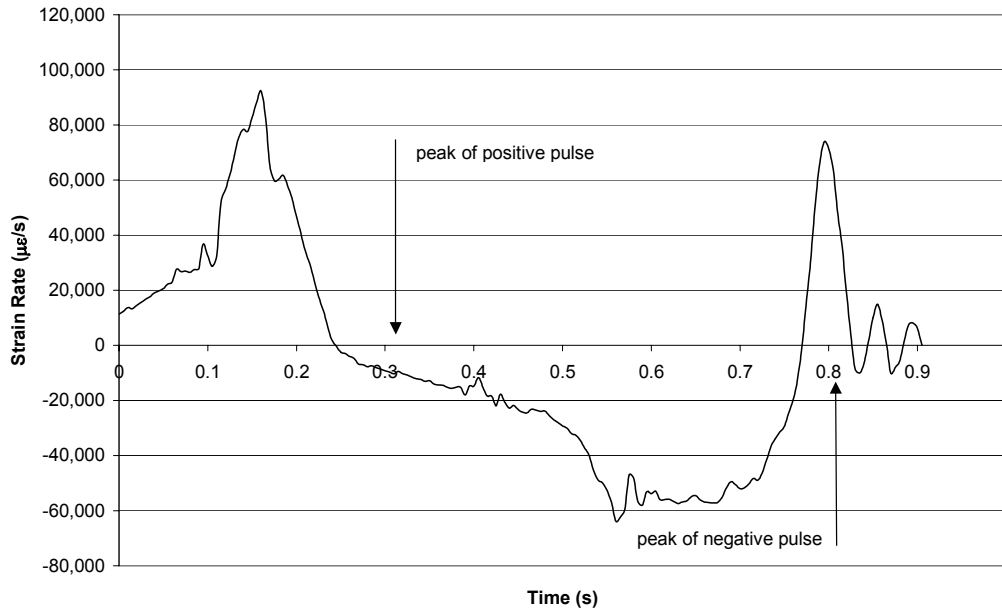


Fig. 5.53 Strain-rate time history: north column longitudinal bar, pulse of current design specimen, dynamic test

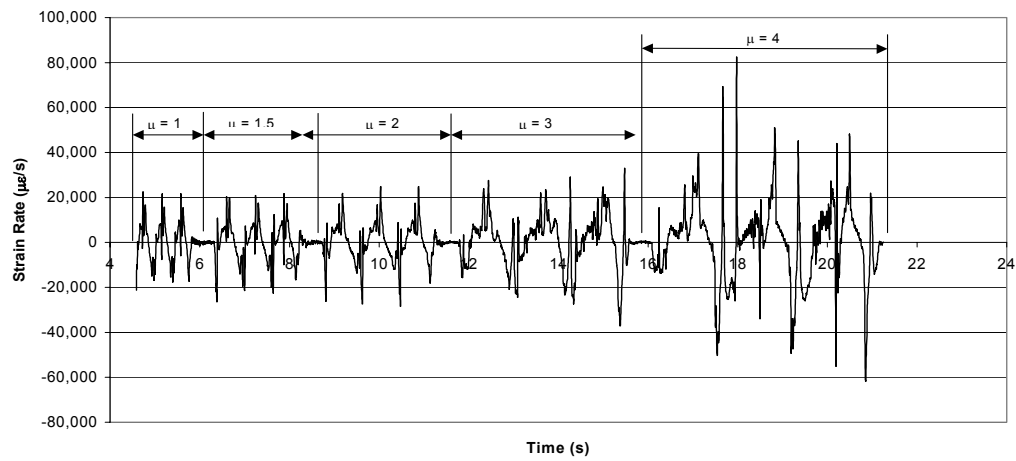


Fig. 5.54 Strain-rate time history: south column longitudinal bar during cyclic loading of current design dynamic test

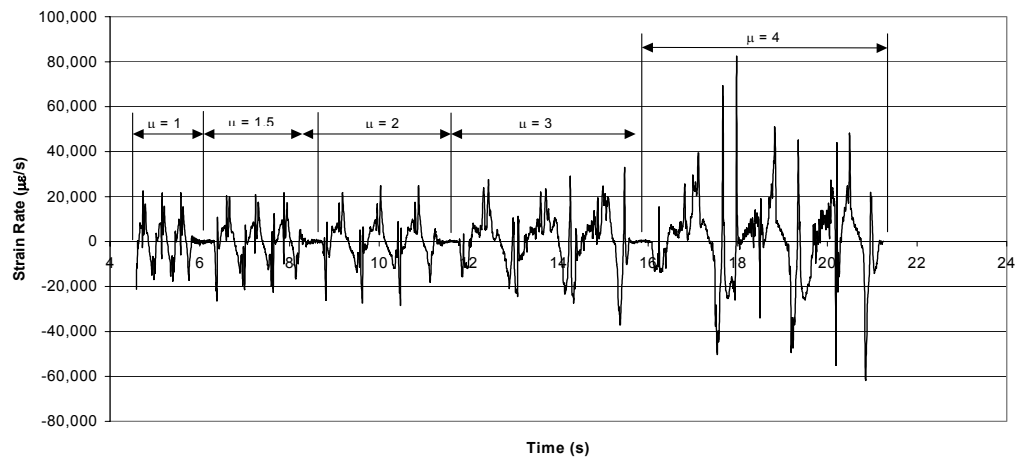


Fig. 5.55 Strain-rate time history: south column longitudinal bar during cyclic loading of current design dynamic test

6 Numerical Modeling

The theoretical strength and deformation response of the specimens was assessed before testing using a simple moment-curvature analysis program as described in this section. The prediction was compared to the actual test results and then the test results were revised to take into account new methods for calculation of the average column curvature from test data. The prediction was then revised to account for the change in material properties due to strain-rate effects. The revised moment-curvature prediction was then compared to the dynamic test results for both the pre-1971 and the current design test specimens.

6.1 PREDICTED RESPONSE

A moment-curvature analysis was performed by computer using the SEQAD Moment Curvature Analysis Program (SEQMC) produced by SC Solutions. The column cross section described in Chapter 3 was modeled as a cantilevered column. Since the columns of the two designs were identical, only one analysis was performed. The SEQMC program determines moment and curvature characteristics for planar reinforced concrete sections. The analysis is based on Mander's (1988) confined concrete model. This concrete model considers the strength enhancement of reinforced concrete due to confinement, and strain hardening of longitudinal reinforcement. The moment-curvature relation is produced by the computer program for a user-defined axial load level, and is calculated until concrete or steel strain limits are reached.

The steel model that was chosen for the prediction was the high strength steel model that had a user-defined yield stress. The high-strength model has no defined yield plateau and the ultimate stress of the steel is defined as 150% of the yield stress. This model was chosen because the grade 60 steel that was used in construction of the specimens does not typically show a defined yield plateau. This is the standard option chosen when analyzing sections using grade 60 or higher steel. The properties that were used in the model for the steel yield stress, and the

concrete compression stress were determined from the material testing performed as described in Section 5.1.

The response of the quasi-static tests was generally less than for the predicted model. In the negative direction of the current design specimen test, as shown in Figure 6.1, the prediction traced an envelope for the behavior of the specimen, but in the positive direction, the behavior during the pulse displacement never reached the levels predicted. The pre-1971 specimen never reached the expected strength of the column in either direction, as shown in Figure 6.2. When looking at both of the dynamic tests, as shown in Figures 6.3 and 6.4, the stiffness seen in the test results during the pulse loading is less than the prediction, and the strength of the specimens is higher than predicted by the model. The difference in stiffness could be due to the method used for calculating the curvature at the base of the column from the potentiometer readings. The difference in strength could be due to the strain-rate effects of the dynamic material response. A modification of the curvature calculation and the material properties to account for strain rate is presented in the next section.

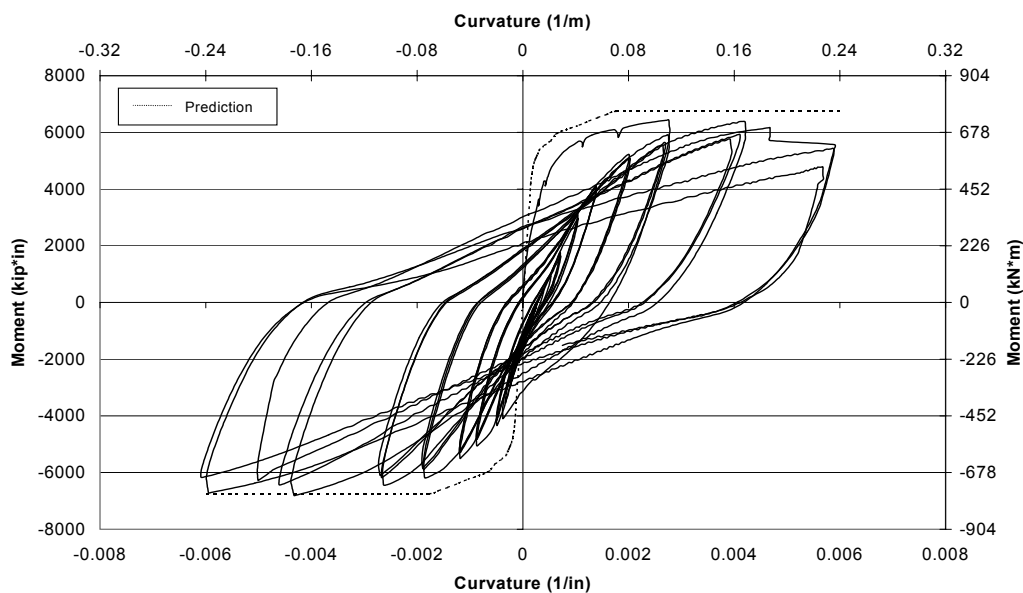


Fig. 6.1 Moment-curvature history: current design specimen quasi-static test

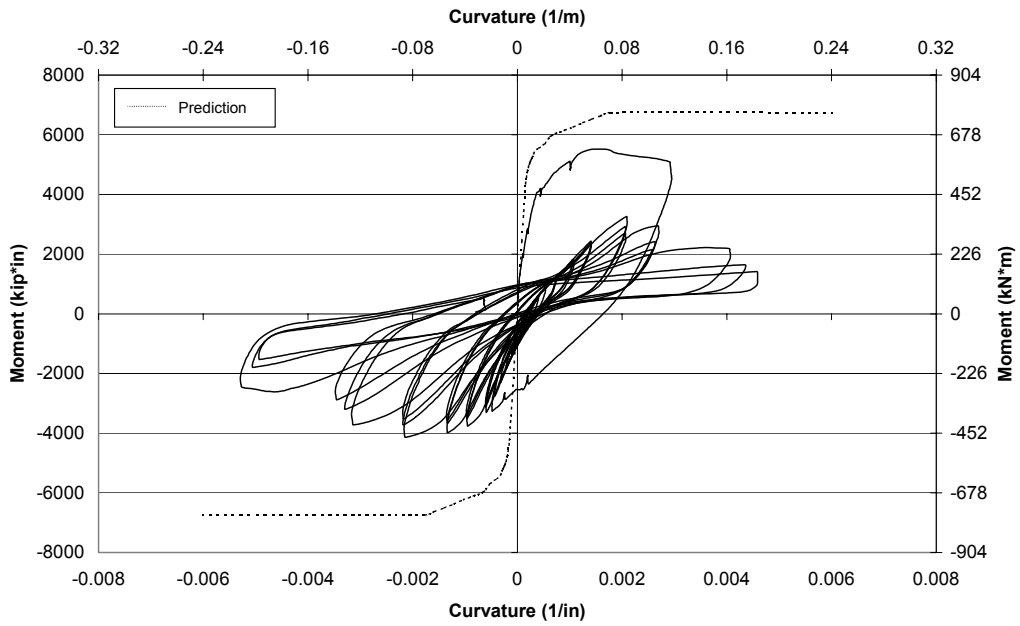


Fig. 6.2 Moment-curvature history: pre-1971 specimen quasi-static test

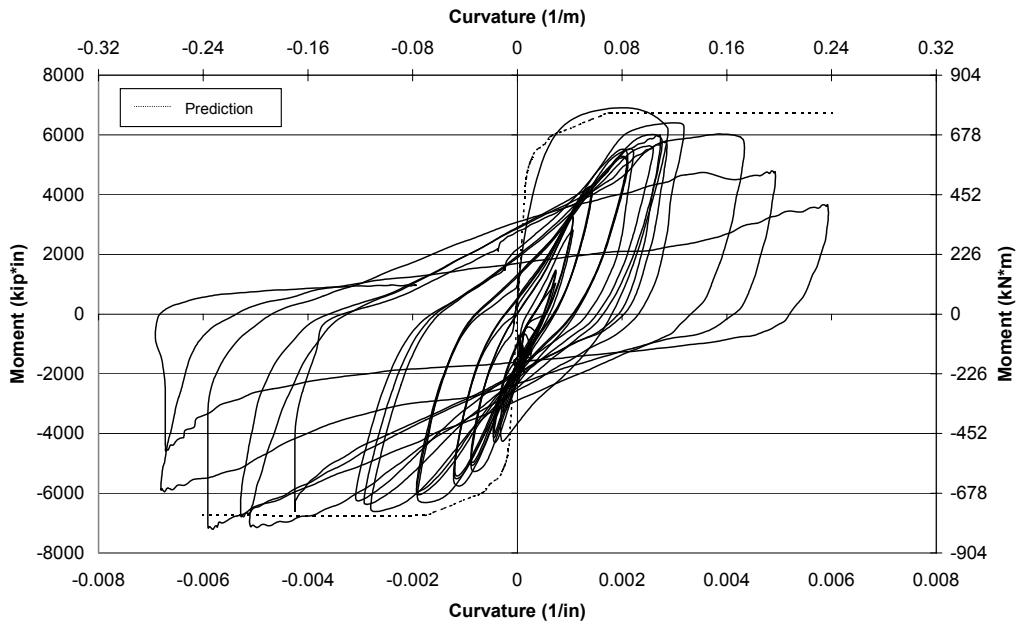


Fig. 6.3 Moment-curvature history: current design specimen dynamic test

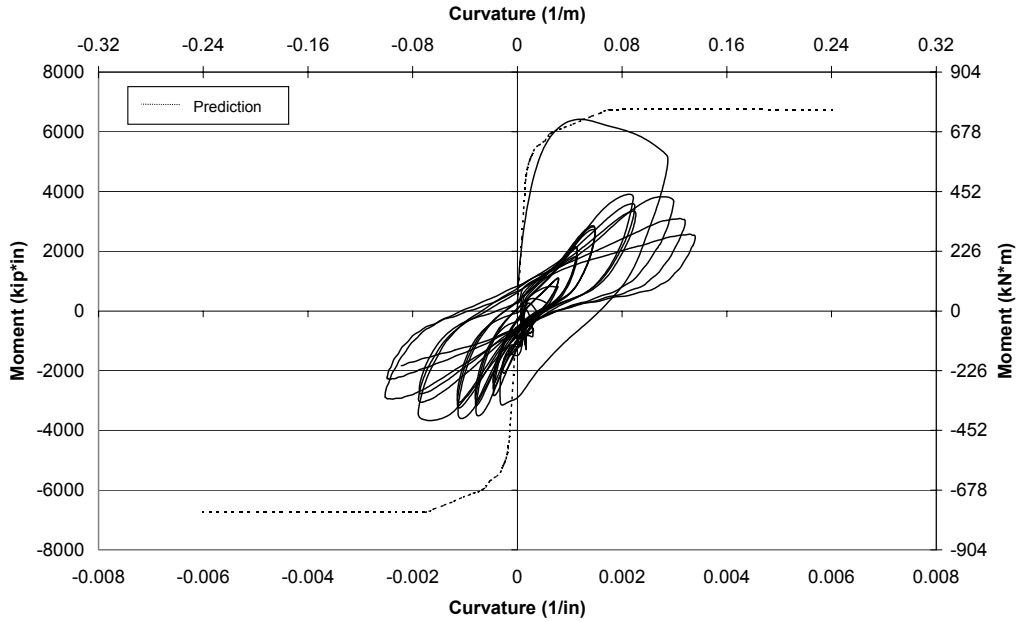


Fig. 6.4 Moment-curvature history: pre-1971 specimen dynamic test

6.2 MOMENT-CURVATURE RESPONSE FOR DYNAMIC TESTS

The initial stiffness of the specimens differs between the predicted and the observed behavior. This discrepancy was addressed by Priestley (1994) and Sritharan (1996). They proposed using a modified gauge length in the calculation of average curvature at the base of the column to account for additional rotation due to strain penetration into the joint. This equation for the modified gauge length is presented below:

$$l_g' = l_{sp} + l_g \left(1 - 1.67 \frac{l_g}{l_c} \right) \quad (6.1)$$

$$l_{sp} = 0.022 f_y d_{bl} \quad (6.2)$$

Where l_g' is the modified gauge length, l_g is the actual gauge length, l_{sp} is the strain penetration length for the column longitudinal reinforcing bars, and l_c is the length of the column from the loading point to the base.

The modified gauge length was then used to re-compute the curvature, Equation 5.4. The revised moment-curvature hysteresis graphs are compared with the SEQMC prediction as shown in Figures 6.5 and 6.6. The revised hysteresis graphs are stiffer in the pulse loading and match

much closer the predicted stiffness, but the specimens now show much higher strength during the pulse than the prediction. This could be due to the high strain rates that were present during the pulse loading.

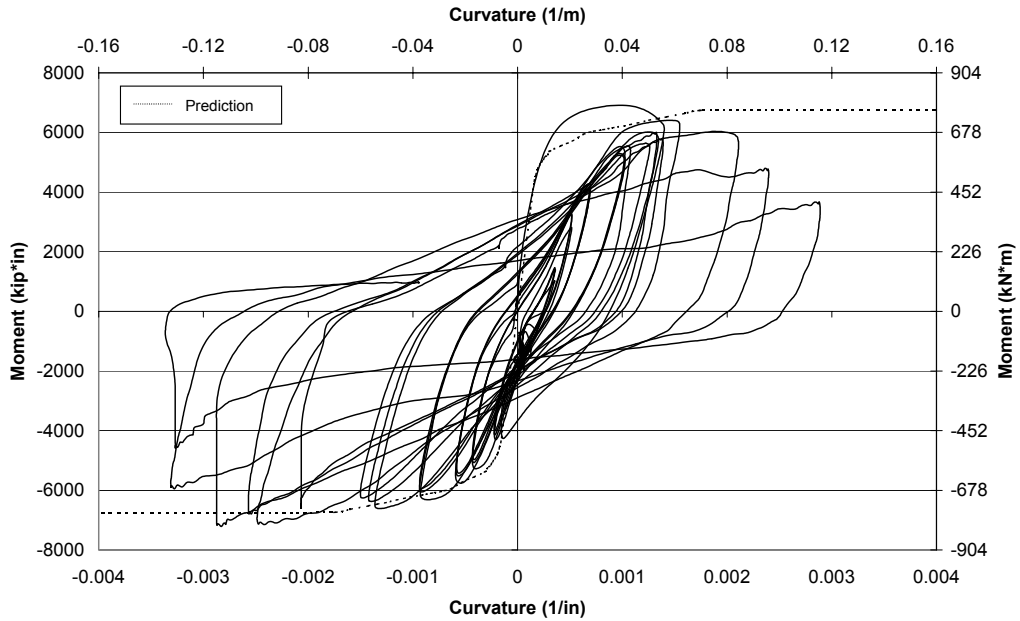


Fig. 6.5 Moment-curvature history: current design specimen with revised gauge length for curvature calculation

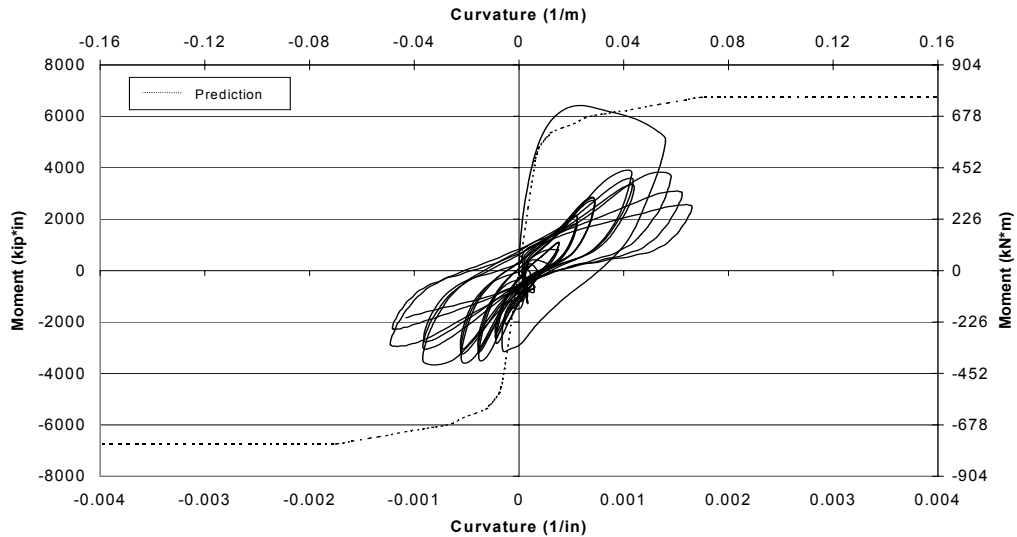


Fig. 6.6 Moment-curvature history: pre-1971 specimen with revised gauge length for curvature calculation

The strain-rate equations presented in Section 2.3 were applied to the material properties presented in Tables 5.1 and 5.2 to determine the dynamic material properties appropriate for the high strain rates seen during the pulse loading. The strain rate for this calculation was chosen as an average value of the strain rates of the north and south column longitudinal bars during the positive pulse. This average value was 0.13 $\mu\epsilon/\text{sec}$. The results of the equations are presented below in Table 6.1. The mean values of these properties were then used in the SEQMC program to produce a revised moment-curvature prediction that better fits the response of the specimens to the velocity pulse. The Mander (1988) steel model option was used in the post analysis because the model can incorporate the change in steel properties seen during higher strain rates. The yield stress and the ultimate stress levels must be defined by the user so that the decrease in the ratio between the two stress levels and can be accounted for as discussed in Section 2.3.1.

Table 6.1 Dynamic material properties

Property	Static Values		Dynamic Values			Mean Dynamic Value	
	MPa	ksi	Equation #	MPa	ksi	MPa	ksi
F_y	437	63.4	Wright & Hall (2-2)	640.5	92.9	534.9	77.6
			Soroushian & Choi (2-3)	602.0	87.3		
			Kaneko et al. (2-5)	502.3	72.9		
			Ammann (2-7)	484.1	70.2		
			Wakabayshi (2-9)	445.5	64.6		
F_u	709	102.9	Soroushian & Choi (2-4)	783.7	113.7	750.3	108.9
			Kaneko et al. (2-6)	746.3	108.3		
			Ammann (2-8)	720.8	104.6		
E_c	30690	4452	Ammann (2-10)	38145.3	5534.1	38145	5534
f'_c	42.0	6.1	Ammann (2-11)	53.1	7.7	52.3	7.6
			Wakabayshi (2-12)	51.4	7.5		

The new moment-curvature prediction is much closer to the specimen response as shown in Figures 6.7 and 6.8. The maximum moments seen during the pulse are now accounted for by the revised dynamic material properties. This revised analysis shows that the behavior of the specimens during the velocity pulse can be predicted using material properties that are adjusted for high strain rates. The behavior of the specimens after the pulse cannot be adequately predicted by simple computer analysis because of the damage caused during the pulse loading. The prediction does provide, however, a good limiting envelope for the behavior of the current design specimens. The pre-1971 specimens followed the prediction closely during the early

loading of the positive pulse but due to the concentration of damage in the joint, the maximum predicted moment was never reached.

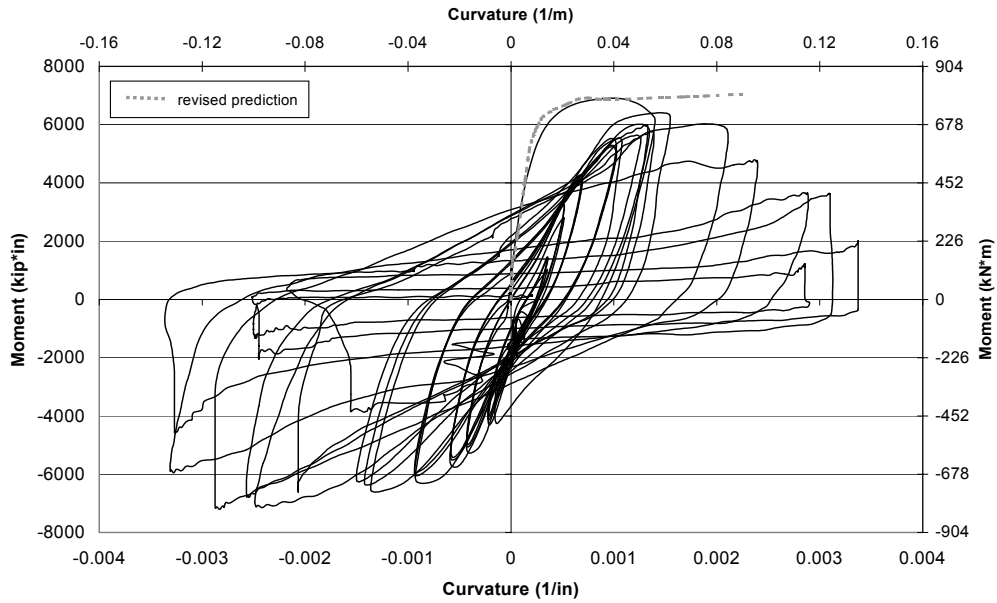


Fig. 6.7 Moment-curvature history: current design dynamic test with prediction revised for dynamic material properties

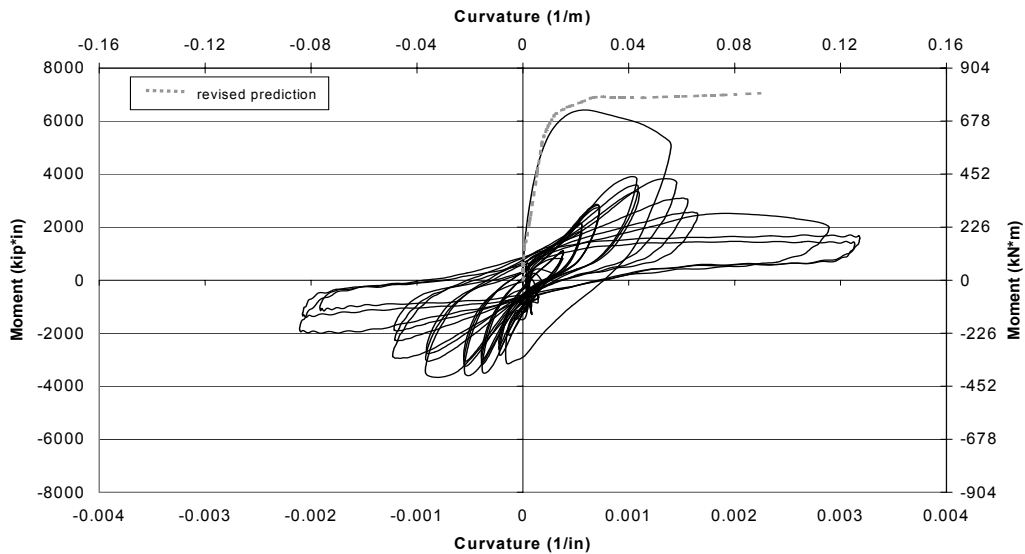


Fig. 6.8 Moment-curvature history: pre-1971 dynamic test with prediction revised for dynamic material properties

7 Summary and Conclusions

Four beam-column joint specimens were tested for this report to investigate the performance of bridge joints subjected to a large velocity pulse. Two of the specimens were older designs typical of the construction before the damaging 1971 San Fernando, California, earthquake, which prompted much code reform. The design of the other two specimens was revised from the pre-1971 model to conform to current design practices in California.

All four specimens were subjected to the same loading history. This protocol included a high velocity, large displacement pulse at the beginning of a typical cyclic loading test. One of the specimens of each design was tested quasi-statically and one was tested dynamically. Although some increases in strength were seen due to the velocity of the dynamic pulse and cyclic loading, generally the dynamic and quasi-static test results were similar. The current design units dissipated most of the energy in the plastic hinge region where the column longitudinal steel eventually fractured. Levels I–III of the PEER Bridge Performance Levels were seen during the pulse for the current design specimens, but the specimens were able to withstand loading up to the first cycle at eight times yield displacement ($\mu=8$) before strength degradation (Level V) and behaved more uniformly after the pulse than the pre-1971 units. The pre-1971 specimens began to fail in the joint, exhibiting all five of the PEER Bridge Performance Levels, during the push portion of the large positive pulse. Strength levels dropped off and subsequent cycling showed strengths of about half of the original level. The pre-1971 joints degraded quickly and the tests had to be stopped at six times the yield displacement ($\mu=6$), earlier than with the current design specimens.

The following conclusions were drawn from the testing performed for this report:

- The pulse caused significant damage to the pre-1971 specimens, as compared to the same design tested without a pulse.
- The overall behavior of the current design specimens was not greatly affected by the pulse loading.

- The pulse loading increased the damage to specimens but did not change the expected failure mechanism of the joints.
- The current design specimens dissipated as much or more energy when tested with a velocity pulse as when tested without a pulse.
- The pre-1971 units dissipated less energy due to the damage in the joint caused by the pulse than did the non-pulse tests of the same design.
- The dynamic pulse loading produced strengths in the specimens higher than predicted by the original moment-curvature analysis.
- By revising the material properties for high strain rates, the additional strength seen during the pulse loading can be accounted for in a moment-curvature prediction.

REFERENCES

Abrams, D. (1996) "Effects of Scale and Loading Rate with Tests of Concrete and Masonry Structures", *Earthquake Spectra*, Earthquake Engineering Research Institute, Vol. 12, No.1, P13-28.

Ammann, W. and Nussbaumer, H. (1995) "Behavior of Concrete and Steel under Dynamic Actions", *Vibration Problems in Structures*, Birkhauser, Basel, Switzerland, P177-183.

Cox, K. (2001) "Characterization of a Large Velocity Directivity Pulse for Laboratory Testing", report submitted for Master's Degree in Structural Engineering, UCSD.

Gioncu, V. (2000) "Influence of Strain-Rate on the Behavior of Steel Members", *Behaviour of Steel Structures in Seismic Areas*, Proceedings of the Third International Conference STESSA 2000, Montreal, Canada, August 21-24, A.A.Balkema, Netherlands, P19-26.

Hamilton, C. H., Pardoen, G. C. and Kazanjy, R. P. (2000) "Experimental Testing of Bridge Columns Subjected to Reversed-cyclic and Pulse-type Loading Histories." Report 2000-12-01, *Civil Engineering Technical Report Series*, University of California, Irvine, December.

Hamilton, C. H., Pardoen, G. C., Kazanjy, R. P. and Hose, Y. D. (2001) "Experimental and Analytical Assessment of Simple Bridge Structures Subjected to Near-fault Ground Motions". *Proceedings of the International Conference on Engineering Mechanics and Computation 2001*, Cape Town, South Africa, April.

International Conference of Building Officials, *1997 Uniform Building Code*, Volume 2, Structural Engineering Design Provisions, Whittier, California

Krawinkler, H. (1996) "Cyclic Loading Histories for Seismic Experimentation of Structural Components" *Earthquake Spectra*, Earthquake Engineering Research Institute, Vol. 12, No. 1, February, P1-12.

Leon, T. and Deierlein, G. (1996) “Considerations for the Use of Quasi-Static Testing”, *Earthquake Spectra*, Earthquake Engineering Research Institute, Vol. 12, No. 1, February, P87-109.

MacRae, G. A., Priestley, M. J. N. and Seible, F. (1994) “Santa Monica Viaduct Retrofit – Large-scale Column-cap Beam Joint Transverse Test – Preliminary Report,” *Structural Systems Research Project*, Report No. TR-94/02, University of California at San Diego, California.

Makley, B. (2001) “Seismic Behavior of Bridge Shear Columns Subjected to Near Field Pulse Loading”, report submitted for Master’s Degree in Structural Engineering, UCSD.

Mander, J. B., Priestley, M. J. N. and Park, R. (1998) “Theoretical Stress-Strain Model for Confined Concrete”, *Journal of Structural Engineering, ASCE*, Vol. 114, P1804-1826.

Mayes, R. and Shaw, A. (1997) “The Effect of Near Fault Ground Motions on Bridge Columns”, *Proceedings of the FHWA/NCEER Workshop on the National Representation of Seismic Ground Motion for New and Existing Highway Facilities*, Burlingame, California, May 29-30.

Orozco, G. (2001) “The Effect of Large Velocity Pulses on Bridge Piers”, Report submitted for Master’s Degree in Structural Engineering, UCSD.

Priestley, M. J. N., Seible, F. and Calvi, G. M. (1996) *Seismic Design and Retrofit of Bridges*, Wiley-Interscience Publications, New York.

SEQAD Inc., SEQad Moment Curvature Analysis Program (SEQMC), distributed by SC Solutions, available online at <http://www.best.com/~solvers/seqmc/html>.

Somerville, P. (2000) “Characterization of Near Field Ground Motions”, *U.S.-Japan Workshop: Effects of Near-Field Earthquake Shaking*, San Francisco, March 20&21.

Somerville, P. (1997) “The Characteristics and Quantification of Near Fault Ground Motion”, *Proceedings of the FHWA/NCEER Workshop on the National Representation of Seismic Ground Motion for New and Existing Highway Facilities*, Burlingame, California, May 29-30.

Sritharan, S., Priestley, M.J.N. and Seible, F. (1996) *Seismic Response of Column/Cap Beam Tee Connections with Cap Beam Prestressing*, Structural Systems Research Report, Report No. SSRP-96/09, University of California at San Diego, California.

Wakabayshi, M., Nakamura, T., Iwai, S. and Hayashi, Y., “Effects of Strain Rate on the Behavior of Structural Members Subjected to Earthquake Force”, *Eighth World Conference on Earthquake Engineering*, San Francisco 1984, Volume IV.

PEER REPORTS

PEER reports are available from the National Information Service for Earthquake Engineering (NISEE). To order PEER reports, please contact the Pacific Earthquake Engineering Research Center, 1301 South 46th Street, Richmond, California 94804-4698. Tel.: (510) 231-9468; Fax: (510) 231-9461.

- PEER 2002/24** *Performance of Beam to Column Bridge Joints Subjected to a Large Velocity Pulse.* Natalie Gibson, André Filiatrault, and Scott A. Ashford. April 2002.
- PEER 2002/23** *Effects of Large Velocity Pulses on Reinforced Concrete Bridge Columns.* Greg L. Orozco and Scott A. Ashford. April 2002.
- PEER 2002/22** *Characterization of Large Velocity Pulses for Laboratory Testing.* Kenneth E. Cox and Scott A. Ashford. April 2002.
- PEER 2002/21** *Fourth U.S.-Japan Workshop on Performance-Based Earthquake Engineering Methodology for Reinforced Concrete Building Structures.* December 2002.
- PEER 2002/20** *Barriers to Adoption and Implementation of PBEE Innovations.* Peter J. May. August 2002.
- PEER 2002/19** *Economic-Engineered Integrated Models for Earthquakes: Socioeconomic Impacts.* Peter Gordon, James E. Moore II, and Harry W. Richardson. July 2002.
- PEER 2002/18** *Assessment of Reinforced Concrete Building Exterior Joints with Substandard Details.* Chris P. Pantelides, Jon Hansen, Justin Nadauld, and Lawrence D. Reaveley. May 2002.
- PEER 2002/17** *Structural Characterization and Seismic Response Analysis of a Highway Overcrossing Equipped with Elastomeric Bearings and Fluid Dampers: A Case Study.* Nicos Makris and Jian Zhang. November 2002.
- PEER 2002/16** *Estimation of Uncertainty in Geotechnical Properties for Performance-Based Earthquake Engineering.* Allen L. Jones, Steven L. Kramer, and Pedro Arduino. December 2002.
- PEER 2002/15** *Seismic Behavior of Bridge Columns Subjected to Various Loading Patterns.* Asadollah Esmaeily-Gh. and Yan Xiao. December 2002.
- PEER 2002/14** *Inelastic Seismic Response of Extended Pile Shaft Supported Bridge Structures.* T.C. Hutchinson, R.W. Boulanger, Y.H. Chai, and I.M. Idriss. December 2002.
- PEER 2002/13** *Probabilistic Models and Fragility Estimates for Bridge Components and Systems.* Paolo Gardoni, Armen Der Kiureghian, and Khalid M. Mosalam. June 2002.
- PEER 2002/12** *Effects of Fault Dip and Slip Rake on Near-Source Ground Motions: Why Chi-Chi Was a Relatively Mild M7.6 Earthquake.* Brad T. Aagaard, John F. Hall, and Thomas H. Heaton. December 2002.
- PEER 2002/11** *Analytical and Experimental Study of Fiber-Reinforced Strip Isolators.* James M. Kelly and Shakhzod M. Takhirov. September 2002.

- PEER 2002/10** *Centrifuge Modeling of Settlement and Lateral Spreading with Comparisons to Numerical Analyses.* Sivapalan Gajan and Bruce L. Kutter. January 2003.
- PEER 2002/09** *Documentation and Analysis of Field Case Histories of Seismic Compression during the 1994 Northridge, California, Earthquake.* Jonathan P. Stewart, Patrick M. Smith, Daniel H. Whang, and Jonathan D. Bray. October 2002.
- PEER 2002/08** *Component Testing, Stability Analysis and Characterization of Buckling-Restrained Unbonded BracesTM.* Cameron Black, Nicos Makris, and Ian Aiken. September 2002.
- PEER 2002/07** *Seismic Performance of Pile-Wharf Connections.* Charles W. Roeder, Robert Graff, Jennifer Soderstrom, and Jun Han Yoo. December 2001.
- PEER 2002/06** *The Use of Benefit-Cost Analysis for Evaluation of Performance-Based Earthquake Engineering Decisions.* Richard O. Zerbe and Anthony Falit-Baiamonte. September 2001.
- PEER 2002/05** *Guidelines, Specifications, and Seismic Performance Characterization of Nonstructural Building Components and Equipment.* André Filiatrault, Constantin Christopoulos, and Christopher Stearns. September 2001.
- PEER 2002/04** *Consortium of Organizations for Strong-Motion Observation Systems and the Pacific Earthquake Engineering Research Center Lifelines Program: Invited Workshop on Archiving and Web Dissemination of Geotechnical Data, 4–5 October 2001.* September 2002.
- PEER 2002/03** *Investigation of Sensitivity of Building Loss Estimates to Major Uncertain Variables for the Van Nuys Testbed.* Keith A. Porter, James L. Beck, and Rustem V. Shaikhutdinov. August 2002.
- PEER 2002/02** *The Third U.S.-Japan Workshop on Performance-Based Earthquake Engineering Methodology for Reinforced Concrete Building Structures.* July 2002.
- PEER 2002/01** *Nonstructural Loss Estimation: The UC Berkeley Case Study.* Mary C. Comerio and John C. Stallmeyer. December 2001.
- PEER 2001/16** *Statistics of SDF-System Estimate of Roof Displacement for Pushover Analysis of Buildings.* Anil K. Chopra, Rakesh K. Goel, and Chatpan Chintanapakdee. December 2001.
- PEER 2001/15** *Damage to Bridges during the 2001 Nisqually Earthquake.* R. Tyler Ranf, Marc O. Eberhard, and Michael P. Berry. November 2001.
- PEER 2001/14** *Rocking Response of Equipment Anchored to a Base Foundation.* Nicos Makris and Cameron J. Black. September 2001.
- PEER 2001/13** *Modeling Soil Liquefaction Hazards for Performance-Based Earthquake Engineering.* Steven L. Kramer and Ahmed-W. Elgamal. February 2001.
- PEER 2001/12** *Development of Geotechnical Capabilities in OpenSees.* Boris Jeremic. September 2001.
- PEER 2001/11** *Analytical and Experimental Study of Fiber-Reinforced Elastomeric Isolators.* James M. Kelly and Shakhzod M. Takhirov. September 2001.

- PEER 2001/10** *Amplification Factors for Spectral Acceleration in Active Regions.* Jonathan P. Stewart, Andrew H. Liu, Yoojoong Choi, and Mehmet B. Baturay. December 2001.
- PEER 2001/09** *Ground Motion Evaluation Procedures for Performance-Based Design.* Jonathan P. Stewart, Shyh-Jeng Chiou, Jonathan D. Bray, Robert W. Graves, Paul G. Somerville, and Norman A. Abrahamson. September 2001.
- PEER 2001/08** *Experimental and Computational Evaluation of Reinforced Concrete Bridge Beam-Column Connections for Seismic Performance.* Clay J. Naito, Jack P. Moehle, and Khalid M. Mosalam. November 2001.
- PEER 2001/07** *The Rocking Spectrum and the Shortcomings of Design Guidelines.* Nicos Makris and Dimitrios Konstantinidis. August 2001.
- PEER 2001/06** *Development of an Electrical Substation Equipment Performance Database for Evaluation of Equipment Fragilities.* Thalia Agnanos. April 1999.
- PEER 2001/05** *Stiffness Analysis of Fiber-Reinforced Elastomeric Isolators.* Hsiang-Chuan Tsai and James M. Kelly. May 2001.
- PEER 2001/04** *Organizational and Societal Considerations for Performance-Based Earthquake Engineering.* Peter J. May. April 2001.
- PEER 2001/03** *A Modal Pushover Analysis Procedure to Estimate Seismic Demands for Buildings: Theory and Preliminary Evaluation.* Anil K. Chopra and Rakesh K. Goel. January 2001.
- PEER 2001/02** *Seismic Response Analysis of Highway Overcrossings Including Soil-Structure Interaction.* Jian Zhang and Nicos Makris. March 2001.
- PEER 2001/01** *Experimental Study of Large Seismic Steel Beam-to-Column Connections.* Egor P. Popov and Shakhzod M. Takhirov. November 2000.
- PEER 2000/10** *The Second U.S.-Japan Workshop on Performance-Based Earthquake Engineering Methodology for Reinforced Concrete Building Structures.* March 2000.
- PEER 2000/09** *Structural Engineering Reconnaissance of the August 17, 1999 Earthquake: Kocaeli (Izmit), Turkey.* Halil Sezen, Kenneth J. Elwood, Andrew S. Whittaker, Khalid Mosalam, John J. Wallace, and John F. Stanton. December 2000.
- PEER 2000/08** *Behavior of Reinforced Concrete Bridge Columns Having Varying Aspect Ratios and Varying Lengths of Confinement.* Anthony J. Calderone, Dawn E. Lehman, and Jack P. Moehle. January 2001.
- PEER 2000/07** *Cover-Plate and Flange-Plate Reinforced Steel Moment-Resisting Connections.* Taejin Kim, Andrew S. Whittaker, Amir S. Gilani, Vitelmo V. Bertero, and Shakhzod M. Takhirov. September 2000.
- PEER 2000/06** *Seismic Evaluation and Analysis of 230-kV Disconnect Switches.* Amir S. J. Gilani, Andrew S. Whittaker, Gregory L. Fenves, Chun-Hao Chen, Henry Ho, and Eric Fujisaki. July 2000.
- PEER 2000/05** *Performance-Based Evaluation of Exterior Reinforced Concrete Building Joints for Seismic Excitation.* Chandra Clyde, Chris P. Pantelides, and Lawrence D. Reaveley. July 2000.

- PEER 2000/04** *An Evaluation of Seismic Energy Demand: An Attenuation Approach.* Chung-Che Chou and Chia-Ming Uang. July 1999.
- PEER 2000/03** *Framing Earthquake Retrofitting Decisions: The Case of Hillside Homes in Los Angeles.* Detlof von Winterfeldt, Nels Roselund, and Alicia Kitsuse. March 2000.
- PEER 2000/02** *U.S.-Japan Workshop on the Effects of Near-Field Earthquake Shaking.* Andrew Whittaker, ed. July 2000.
- PEER 2000/01** *Further Studies on Seismic Interaction in Interconnected Electrical Substation Equipment.* Armen Der Kiureghian, Kee-Jeung Hong, and Jerome L. Sackman. November 1999.
- PEER 1999/14** *Seismic Evaluation and Retrofit of 230-kV Porcelain Transformer Bushings.* Amir S. Gilani, Andrew S. Whittaker, Gregory L. Fenves, and Eric Fujisaki. December 1999.
- PEER 1999/13** *Building Vulnerability Studies: Modeling and Evaluation of Tilt-up and Steel Reinforced Concrete Buildings.* John W. Wallace, Jonathan P. Stewart, and Andrew S. Whittaker, editors. December 1999.
- PEER 1999/12** *Rehabilitation of Nonductile RC Frame Building Using Encasement Plates and Energy-Dissipating Devices.* Mehrdad Sasani, Vitelmo V. Bertero, James C. Anderson. December 1999.
- PEER 1999/11** *Performance Evaluation Database for Concrete Bridge Components and Systems under Simulated Seismic Loads.* Yael D. Hose and Frieder Seible. November 1999.
- PEER 1999/10** *U.S.-Japan Workshop on Performance-Based Earthquake Engineering Methodology for Reinforced Concrete Building Structures.* December 1999.
- PEER 1999/09** *Performance Improvement of Long Period Building Structures Subjected to Severe Pulse-Type Ground Motions.* James C. Anderson, Vitelmo V. Bertero, and Raul Bertero. October 1999.
- PEER 1999/08** *Envelopes for Seismic Response Vectors.* Charles Menun and Armen Der Kiureghian. July 1999.
- PEER 1999/07** *Documentation of Strengths and Weaknesses of Current Computer Analysis Methods for Seismic Performance of Reinforced Concrete Members.* William F. Cofer. November 1999.
- PEER 1999/06** *Rocking Response and Overturning of Anchored Equipment under Seismic Excitations.* Nicos Makris and Jian Zhang. November 1999.
- PEER 1999/05** *Seismic Evaluation of 550 kV Porcelain Transformer Bushings.* Amir S. Gilani, Andrew S. Whittaker, Gregory L. Fenves, and Eric Fujisaki. October 1999.
- PEER 1999/04** *Adoption and Enforcement of Earthquake Risk-Reduction Measures.* Peter J. May, Raymond J. Burby, T. Jens Feeley, and Robert Wood.
- PEER 1999/03** *Task 3 Characterization of Site Response General Site Categories.* Adrian Rodriguez-Marek, Jonathan D. Bray, and Norman Abrahamson. February 1999.

- PEER 1999/02** *Capacity-Demand-Diagram Methods for Estimating Seismic Deformation of Inelastic Structures: SDF Systems.* Anil K. Chopra and Rakesh Goel. April 1999.
- PEER 1999/01** *Interaction in Interconnected Electrical Substation Equipment Subjected to Earthquake Ground Motions.* Armen Der Kiureghian, Jerome L. Sackman, and Kee-Jeung Hong. February 1999.
- PEER 1998/08** *Behavior and Failure Analysis of a Multiple-Frame Highway Bridge in the 1994 Northridge Earthquake.* Gregory L. Fenves and Michael Ellery. December 1998.
- PEER 1998/07** *Empirical Evaluation of Inertial Soil-Structure Interaction Effects.* Jonathan P. Stewart, Raymond B. Seed, and Gregory L. Fenves. November 1998.
- PEER 1998/06** *Effect of Damping Mechanisms on the Response of Seismic Isolated Structures.* Nicos Makris and Shih-Po Chang. November 1998.
- PEER 1998/05** *Rocking Response and Overturning of Equipment under Horizontal Pulse-Type Motions.* Nicos Makris and Yiannis Roussos. October 1998.
- PEER 1998/04** *Pacific Earthquake Engineering Research Invitational Workshop Proceedings, May 14–15, 1998: Defining the Links between Planning, Policy Analysis, Economics and Earthquake Engineering.* Mary Comerio and Peter Gordon. September 1998.
- PEER 1998/03** *Repair/Upgrade Procedures for Welded Beam to Column Connections.* James C. Anderson and Xiaojing Duan. May 1998.
- PEER 1998/02** *Seismic Evaluation of 196 kV Porcelain Transformer Bushings.* Amir S. Gilani, Juan W. Chavez, Gregory L. Fenves, and Andrew S. Whittaker. May 1998.
- PEER 1998/01** *Seismic Performance of Well-Confined Concrete Bridge Columns.* Dawn E. Lehman and Jack P. Moehle. December 2000.